ALMA MATER STUDIORUM
UNIVERSITÀ DI BOLOGNA

DOTTORATO DI RICERCA IN

INGEGNERIA E TECNOLOGIA DELL'INFORMAZIONE PER IL MONITORAGGIO STRUTTURALE E AMBIENTALE E LA GESTIONE DEI RISCHI - EIT4SEMM

Ciclo 37

Settore Concorsuale: 09/G1 - AUTOMATICA

Settore Scientifico Disciplinare: ING-INF/04 - AUTOMATICA

NEURO ADAPTIVE GUIDANCE AND CONTROL SYSTEM OF A MULTIPURPOSE AUTONOMOUS UNDERWATER VEHICLE FOR UNDERWATER ENVIRONMENT MONITORING

Presentata da: Massimiliano Menghini

Coordinatore Dottorato

Luca De Marchi

Supervisore

Paolo Castaldi

Co-supervisore

Luca De Marchi

Esame finale anno 2025

ALMA MATER STUDIORUM - UNIVERSITÀ DI BOLOGNA

DOTTORATO DI RICERCA IN
INGEGNERIA E TECNOLOGIA DELL'INFORMAZIONE PER IL MONITORAGGIO STRUTTURALE E AMBIENTALE E LA GESTIONE DEI RISCHI - EIT4SEMM
CICLO XXXVII

Settore Concorsuale: ING-INF/04 - Automatica
Settore Scientifico Disciplinare: 09/G1 - Automatica

Neuro Adaptive Guidance and Control system of a Multipurpose Autonomous Underwater Vehicle for Underwater Environment Monitoring

Presentata da:
Massimiliano Menghini

Supervisore
Prof. Paolo Castaldi
Co-supervisore
Prof. Luca De Marchi

Esame Finale Anno 2025

"La scienza non è nient'altro che una perversione se non ha come suo fine ultimo il miglioramento delle condizioni dell'umanità."

Nikola Tesla

Abstract

This thesis introduces a novel neuro-adaptive control framework for Blucy, an hybrid unmanned underwater vehicle (UUV), designed for environmental monitoring in complex underwater environments. Central to this work is the development of a comprehensive benchmark model, rigorously validated against real mission data, which serves as a foundational simulator for designing the neuro-adaptive controller. An original parameter identification workflow is proposed, integrating CAD modeling, CFD simulations, and AMCOMP software to accurately capture hydrodynamic forces and thruster dynamics critical for precise modeling. Based on the benchmark, a novel fixed-time sliding mode control system is designed, augmented with neural networks and disturbance observers that estimate uncertainties and disturbances. To enhance adaptability, the neural network and disturbance observer are trained using a composite error learning strategy, optimizing real-time response to environmental changes and system faults. The effectiveness of the neuro adaptive control framework ensuring precise trajectory tracking and robustness against uncertainties, disturbance and faults, is demonstrated through extensive simulations.

Contents

List of Figures

List of Tables

Chapter 1

Introduction

The field of control systems has witnessed a surge in data-driven methodologies, largely due to advances in machine learning and computational power. These developments have paved the way for direct and indirect data-driven control, especially in complex environments like underwater. Direct data-driven approaches bypass the need for explicit model identification, learning control policies directly from system interactions. This allows for rapid adaptability to nonlinearities and real-time decision-making in uncharted terrains, which has proven useful in many applications like fault detection and isolation of actuator fault [P1] and adaptive tracking control in underwater exploration [1]. However, direct methods depend heavily on extensive datasets and face challenges with generalization outside of training data, as in [2], which noted that while direct methods excel with large datasets, they exhibit higher variance and may underperform with limited data.

Conversely, indirect data-driven approaches utilize system identification to create a model from collected data, which is then used within a structured control framework. This method retains interpretability and benefits from leveraging empirical data to refine the baseline model, allowing for increased stability. Applications of indirect control in underwater contexts include an online model identification framework for underwater vehicles through incremental support vector regression [3] and application of a differential evolution algorithm for precise hydrodynamic modeling in gliders [4]. Yet, indirect methods can exhibit bias and are limited by the accuracy of the model, especially in hostile underwater conditions with unexpected dynamics, as they may converge slower in response to noise and parameter discrepancies [5].

The limitations of purely data-driven models in hostile environments have led to increased interest in model-based approaches augmented by neuro-adaptive controllers, thus resulting in hybrid approaches. This strategy combines the advantages of the model based approach with the adaptability of neural networks, yielding an overall control system that is structurally sound, dynamically responsive and robust to model uncertainties, faults

and exogenous disturbances. In [5], this type of architecture, which integrates intelligent control elements, is beneficial when system resilience is paramount and when the environment's unpredictable dynamics demand quick, adaptive responses. Hence, by establishing a reliable baseline grounded in known dynamics, the neuro-adaptive component can detect and adjust to unforeseen disturbances in real time, addressing shortcomings in both direct and indirect methods without extensive reliance on pre-collected data.

1.1 State of the Art

Modeling of UUV

Blucy is a hybrid Unmanned Underwater Vehicle (UUV), capable of operating remotely or autonomously, depending on the specific mission requirements. It was developed in the Interreg IT-HR SUSHI DROP (sustainable fisheries with drone data processing) [6, P2] project for non-invasive underwater monitoring and to preserve and restore underwater ecosystems. The hybrid modelling involves establishing a mathematical model and identifying the parameters of the model. This enables the creation of accurate simulations of the vehicle's interactions with complex underwater environments, facilitating the design and testing of robust neuro-adaptive controllers, path following, target-tracking algorithms, etc.

Blucy's modular design means the vehicle's configuration can change frequently based on specific mission needs, presenting a significant challenge for system identification. While online system identification methods exist in the literature [7, 8, 9], they are often computationally intensive and not always feasible for rapid deployment. Thus, there is a need for an offline identification workflow that balances experimental and numerical simulation methods, ensuring that it is simple, fast, and produces reliable results for different configurations. The mathematical model of underwater vehicles is summarised in [10, 11, 12]. In the model, the hydrodynamic forces and moments are expressed as truncated Taylor series expansion as a function of linear and angular velocities. The coefficients of the Taylor series are termed hydrodynamic and added mass coefficients that act as parameters of the system. Traditionally, these parameters are estimated experimentally using towing tank tests [13, 14] with a Planar Motion Mechanism (PMM) [15]. This method involves external equipment to measure hydrodynamic forces and moments in six degrees of freedom (6 DOF) without using the vehicle's propulsion system. However, PMMs are costly, and the testing procedures are time-consuming. Each hydrodynamic coefficient requires analysis at multiple motions or speeds, leading to long experiment cycles and difficulty in assessing the overall reliability of the dynamic model. Additionally, these

experiments are expensive.

To be cost-effective and ensure high repeatability, open-water tests are used for parameter identification. This technique utilises the vehicle's propulsion system in open water and onboard sensor data for identification. An offline hydrodynamic parameter identification method based on the least squares method is proposed in [16, 17], using data from onboard sensors. An online-adaptive identification method is proposed in [18]. Other techniques include Kalman filtering [19, 20], neural networks [21], and self-oscillation experiments [22]. In [23], velocity tests are used to identify drag parameters, while oscillatory tests are used to identify inertial and coupled terms of an open-frame underwater vehicle using pre-computed forces and moments. A reduced experimental data set method for parameter identification is proposed in [24], to be cost-effective. However, these approaches are affected by external noise and biases in sensor measurements [25, 26]. Although acceleration measurement is feasible in underwater robotics, it is often unreliable due to sensor noise, hydrodynamic disturbances, and the absence of dedicated instrumentation, making parameter estimation dependent on sensor fusion and indirect methods.

Recent increased computational power has enabled the use of Computational Fluid Dynamics (CFD) for parameter identification within the scientific community. In [27], CFD was applied to determine the sway hydrodynamic derivatives of an autonomous underwater vehicle (AUV), demonstrating the feasibility of using CFD for parameter identification. CFD was also used to simulate PMM tests and obtain hydrodynamic parameters in [28]. In [29], hydrodynamic parameters for an underwater tow vehicle were obtained using CFD and optimised using the least squares method. CFD combined with a maximum likelihood algorithm was used to estimate hydrodynamic parameters in [30]. For a comprehensive overview of hydrodynamic parameter estimation techniques, readers are encouraged to refer to the recent survey presented in [31].

Like hydrodynamic parameters, added mass parameters can also be obtained using CFD [32, 33]. However, calculating added mass with CFD is a computationally intensive process. For this reason, studies such as [29] use CFD for hydrodynamic parameters but obtain added mass parameters analytically using strip theory [34]. Added mass for standard shapes can be computed analytically and adjusted using empirical data [35]. For complex shapes and modular vehicles like Blucy, estimating these parameters each time a module changes is challenging. To address this, a Computer-Aided Design (CAD) based environment called AMCOMP, which estimates the added mass of complex shapes simply and intuitively, is proposed in [36].

Thruster modelling is a crucial aspect of modelling underwater vehicles, as the thruster generates forces and moments that control the vehicle's movement. Initially, first-quadrant modelling is considered which characterises the thruster when both thrust and propeller

rotation inputs are positive. This type of modelling is often approximated as bilinear [12, 24] and is suitable for vehicles designed to maintain a minimum speed concerning the water and manoeuvre using control surfaces [37]. However, for vehicles like Blucy, which require forces and torques for manoeuvring via differential thrust from paired propellers, thrusters must operate beyond the first quadrant. In such cases, propellers frequently change rotational direction to execute curved trajectories, necessitating a different model. The four-quadrant model, which considers arbitrary thrust direction and propeller rotation direction, is more appropriate for these scenarios [38, 39]. Studies on four-quadrant modelling of ducted propellers can be found in [40, 41, 42].

Control of UUV

In regards to control systems, various control strategies have been extensively studied to tackle the challenges of trajectory tracking in underactuated underwater vehicles (UUVs). Classical approaches, such as PID controllers, provide foundational control capabilities [43]. To address more complex scenarios involving uncertain dynamics, adaptive integral sliding mode control has been introduced, improving robustness for underactuated autonomous underwater vehicles (AUVs) [44]. Additionally, fuzzy logic observers have been employed to approximate external disturbances and uncertainties, enhancing stability in dynamic underwater environments [45].

Advanced nonlinear methods, including robust backstepping control, have been developed to improve tracking performance in the presence of modeling uncertainties [46]. For scenarios requiring visual data input, a self-triggered vision-based model predictive control framework has been proposed to facilitate effective trajectory tracking under external disturbances [47]. Disturbance observers, known for their adaptability, have been integrated with control frameworks to enhance robustness in trajectory tracking, allowing for greater accuracy in uncertain conditions [48, 45, 49]. A comprehensive review of nonlinear control strategies offers an in-depth exploration of these techniques and their applications to underactuated AUVs [50].

Among these strategies, Sliding Mode Control (SMC) has garnered significant attention for its robustness against model uncertainties and external disturbances, making it well-suited for UUV applications [51, 52, 53]. However, SMC controllers are prone to chattering, which can be mitigated through techniques such as boundary layer methods, higher-order SMC, or super-twisting methods [48, 54]. To improve SMC's response time and address the need for rapid convergence, Finite-Time Sliding Mode Control (FITSMC) has been introduced [53, 55, 56]. Unlike traditional SMC, which converges asymptotically, FITSMC is designed to bring system states to the desired manifold within a finite time, making it particularly useful in dynamic environments. However, the convergence time

in FITSMC can depend on the initial conditions of the state variables; unknown initial conditions may result in longer convergence times.

Fixed-Time Sliding Mode Control (FTSMC) advances beyond finite-time control by guaranteeing convergence within a predetermined time, irrespective of initial conditions [57]. This characteristic is particularly beneficial for UUV applications, where a known settling time is crucial for mission-critical tasks with strict timing constraints. Consequently, FTSMC has been employed to tackle trajectory tracking issues for underactuated underwater vehicles [58, 59]. FTSMC frameworks often integrate disturbance observers and adaptive mechanisms to manage dynamic external disturbances [60], ensuring robust performance in uncertain underwater environments [61]. This combination of high robustness and predictable convergence times positions FTSMC as a key advancement in nonlinear control for underwater applications.

Recent advances in computational resources have facilitated the rise of Artificial Intelligence (AI) controllers, particularly Neural Networks (NNs). NNs are recognized for their effectiveness in managing various uncertainties and their universal approximation capabilities, making them appealing for researchers. Unlike conventional controllers that rely solely on robustness, intelligent controllers leverage NNs to estimate and address external disturbances, thereby enhancing robustness. A recent review discusses intelligent control strategies for trajectory tracking in underactuated UUVs [62]. FTSMC controllers based on NNs often employ the Feedback Error Learning (FEL) strategy, as seen in [61]. However, this approach may lead to aggressive learning, and the convergence of optimal NN weights requires persistent excitation; without it, NN parameters can drift from their optimal values, resulting in high-gain controllers.

To improve learning efficiency, the design of a state estimator based on estimated uncertainties allows for the incorporation of the estimation error into the learning rule, a process termed composite learning. A composite learning-based controller for underactuated UUVs has been proposed, capable of tracking desired paths amid uncertainties and external disturbances [63]. A backstepping method incorporating composite learning for underactuated systems has also been introduced [64], while another study analyzes composite model reference adaptive control for underactuated AUVs [65].

1.2 Thesis contribution

In the light of the above discussion, in this thesis, a hybrid model-based approach augmented by neuro adaptive controller is proposed for Blucy UUV. The main contribution of the thesis are:

- **End-to-End Benchmark Model Development:** A benchmark model of a novel

underactuated Unmanned Underwater Vehicle, validated using real mission data. The primary contribution is an end-to-end modeling procedure that can be generalized to various UUVs, offering the scientific community a robust tool for testing advanced control and guidance algorithms [P3]. This model is fully validated against real data, encompassing all critical aspects of UUV performance, including physical, hydrodynamic, added mass parameters, and thruster dynamics.

- **Balanced Workflow for Parameter Estimation:** The proposed workflow is peculiar in its balanced integration of experimental methods with numerical simulations for parameter estimation, making it applicable to other underwater vehicles. Physical parameters are derived from a detailed CAD model, which is then simplified for hydrodynamic analysis through CFD simulations, thereby reducing the need for costly experimental methods.

- **Application of AMCOMP to UUVs with complex structure:** A notable aspect of this work is the application of AMCOMP, a research tool developed by the University of Bologna and the Royal Melbourne Institute of Technology, to calculate the added mass of complex shapes. Traditionally used for simpler geometries, this tool offers an efficient alternative to the computationally demanding CFD simulations typically required. This study successfully extends the applicability of AMCOMP to more complex UUV designs, thereby broadening its utility in underwater vehicle modeling.

- **Thruster Modeling:** It introduces a refined thrust model based on four-quadrant propeller modeling, tuned experimentally, and presents an actuator model for thrusters. Finally, the benchmark model is validated against real-mission data to ensure that the simulated results match the actual vehicle dynamics.

- **Neuro-Adaptive Control Framework:** A fixed-time sliding mode controller augmented by neural networks and a disturbance observer. Unlike the approach in [61], which develops a neuro-adaptive fixed-time sliding mode controller trained using a finite error learning (FEL) strategy without incorporating a disturbance observer, this thesis explicitly integrates a disturbance observer to estimate time-varying disturbances. This integration enhances the controller's adaptability and robustness beyond relying solely on the inherent strengths of SMC.

- **Fixed time Convergence:** In contrast, the controllers presented in [63] and [64] focus on composite error learning but lack fixed-time convergence properties. By combining fixed-time sliding mode control with neural networks and disturbance observation, the proposed controller addresses the limitations found in previous

work, offering both rapid convergence and improved disturbance estimation. This comprehensive approach marks a significant advancement in control strategies for UUVs, facilitating more reliable path-following and trajectory tracking in dynamic underwater environments

- **Stability Proof and Validation:** The stability of the methodology is established using Lyapunov methods. The effectiveness of the control approach is demonstrated through Blucy's benchmark model [P3], which indicates that the integrated NN and DO estimations significantly enhance robustness against disturbances, thereby validating the control framework's resilience under realistic operational conditions.

Chapter 2

Mathematical Model

This chapter introduces the general mathematical modeling of unmanned underwater vehicles (UUVs) based on Fossen's model [10, 11, 12]. It covers the coordinate systems used in modeling, along with the kinematics and dynamics of the vehicle using rigid-body six-degree-of-freedom (6 DOF) equations. The 6 DOF equations are further generalized to incorporate the effects of ocean currents.

2.1 Coordinate system

In the context of underwater vehicle dynamics, describing the motion of the vehicle requires the adoption of a well-defined coordinate frames. These frames of reference are essential for representing the vehicle's position, orientation, and velocities relative to the Earth and the vehicle itself. The selection of a coordinate system plays a fundamental role in the kinematic and dynamic equations used to model the vehicle's behaviour in 6 degrees of freedom (DOF). Typically, for underwater vehicles, two primary coordinate systems are used:

- North-East-Down (NED) reference frame $\{n\} = (x_n, y_n, z_n)$: it can be considered to be inertial for most UUVs, as long as they operates at low speeds and within a localized area. This is know as the flat Earth navigation assumption, which simplifies modelling by allowing Newton's law of motion to apply without accounting for the Earth curvature or rotational effects. The NED frame is Earth-fixed coordinate system with:
  - x_n axis pointing toward true North;
  - y_n axis pointing toward true East;
  - z_n axis pointing downward, perpendicular to the Earth's surface;

Figure 2.1: The body reference frame of the Blucy.

This alignment with geographic coordinates makes the NED highly compatible with global navigation systems such as Global Navigation Satellite System (GNSS) or acoustic positioning systems like USBL or LBL. Furthermore, environmental disturbances, such as marine currents are often expressed in the NED frame, making it easier to integrate these forces into the vehicle's dynamic models. The NED frame is also well-suited for path-following and waypoint navigation, where the mission trajectories are defined relative to the fixed geographical coordinates, thus simplifying both mission planning and control strategies.

- Body-fixed coordinate system $\{b\} = (x_b, y_b, z_b)$: This frame is attached to the vehicle and moves with it. It is typically fixed to the vehicle's center of gravity (**CG**), and its axes are defined relative to the vehicle's structure:

  - x_b axis points forward along the vehicle's longitudinal axes (toward the bow);
  - y_b axis points to starboard side (to the right);
  - z_b axis points downward, perpendicular to the vehicle's plane;

  The body-fixed frame is essential to represent vehicle's velocities, forces and control inputs relative to its own geometry. Velocities such as surge, sway, and heave, as well as forces and moments generated by thrusters or hydrodynamic effects, are often computed in this frame. This frame also plays a central role in control system design, where forces and control commands are applied in the body-fixed axes and later transformed into the global NED frame for navigation.

2.2 Kinematics

The six-degree-of-freedom kinematic equations are crucial for describing the motion of underwater vehicle by relating its position, linear velocities, angular velocities, and attitude of the rigid body neglecting the forces that drive the motion. These equation focus on the geometric aspects of motion, describing how the position and attitude evolve as a result of the vehicle's velocity in the body frame. To express these relations, let the following vectors be defined:

$$\eta = \begin{bmatrix} \eta_1 & \eta_2 \end{bmatrix}^\top \quad \text{where} \quad \eta_1 = \begin{bmatrix} x & y & z \end{bmatrix}^\top \quad \text{and} \quad \eta_2 = \begin{bmatrix} \phi & \theta & \psi \end{bmatrix}^\top \tag{2.1}$$

$$\nu = \begin{bmatrix} \nu_1 & \nu_2 \end{bmatrix}^\top \quad \text{where} \quad \nu_1 = \begin{bmatrix} u & v & w \end{bmatrix}^\top \quad \text{and} \quad \nu_2 = \begin{bmatrix} p & q & r \end{bmatrix}^\top \tag{2.2}$$

where the term η represents the position of the body frame with respect to the NED frame in terms of linear displacements (η_1) and the Euler angles (η_2). On the other hand, the term ν represents the linear velocity (ν_1) and the angular velocity (ν_2) expressed in the body-axis system.

The core of UUVs kinematics lies in the transformation between body-frame and NED inertial frame. The relation between time derivative of the inertial position and the linear velocity is given as follows:

$$\dot{\eta}_1 = R_b^n(\eta_2)\nu_1 \tag{2.3}$$

where R_b^n is the rotation matrix from the body reference frame to the NED inertial reference frame, defined as:

$$R_b^n = \begin{bmatrix} c\psi c\theta & -s\psi c\phi + c\psi s\theta s\phi & s\psi s\phi + c\psi c\phi s\theta \\ s\psi c\theta & c\psi c\phi + s\phi s\theta s\psi & -c\psi s\phi + s\theta s\psi c\phi \\ -s\theta & c\theta s\phi & c\theta c\phi \end{bmatrix} \tag{2.4}$$

In the above matrix, the terms $s(\cdot)$ and $c(\cdot)$ represent $\sin(\cdot)$ and $\cos(\cdot)$, respectively. Similarly, the relation between the attitude angles and the angular velocity is expressed as:

$$\dot{\eta}_2 = T_\Theta(\eta_2)\nu_2 \tag{2.5}$$

where, T_Θ represents the transformation matrix defined as follows:

$$T_\Theta = \frac{1}{c\theta} \begin{bmatrix} 1 & s\phi s\theta & c\phi s\theta \\ 0 & c\phi c\theta & -s\phi cos\theta \\ 0 & s\phi & c\phi \end{bmatrix} \tag{2.6}$$

A critical limitation of this matrix is its singularity when the pitch angle $\theta = \pm 90^\circ$. However, for practical underwater vehicle applications, such as those involving the vehicle

Blucy, the likelihood of encountering this issue is null due to the inherent stability of the vehicle's pitch and the high moment of inertia around the y axis, which mitigates extreme pitch angles. Hence, no further analysis on this matter is deemed necessary.

By combining the linear (2.3) and angular (2.5) transformation, the full set of kinematic equations in six degrees of freedom can be expressed as:

$$\begin{bmatrix} \dot{\eta}_1 \\ \dot{\eta}_2 \end{bmatrix} = \begin{bmatrix} R_b^n(\eta_2) & 0_{3\times3} \\ 0_{3\times3} & T_\Theta(\eta_2) \end{bmatrix} \begin{bmatrix} \nu_1 \\ \nu_2 \end{bmatrix} \tag{2.7}$$

In a vectorial form, the equation reads as:

$$\dot{\eta} = J_\Theta(\eta)\nu \tag{2.8}$$

where J_Θ is the Jacobian matrix that combines both the rotation matrix $R_b^n(\eta_2)$ and the trasformation matrix $T_\Theta(\eta_2)$:

$$J_\Theta(\eta) = \begin{bmatrix} R_b^n(\eta_2) & 0_{3\times3} \\ 0_{3\times3} & T_\Theta(\eta_2) \end{bmatrix} \tag{2.9}$$

2.3 Dynamics

Before deriving the equations of motion for a marine craft, it is essential to define two key body-fixed reference points that are used to describe the motion:

- **CO** - origin o_b of body-fixed reference frame $\{b\}$
- **CG** - center of gravity

These two points coincide if the position vector $\vec{r_g} = \vec{0}$, meaning that the center of gravity **CG** is located at the origin of the body-fixed frame. The location of **CO** is typically selected by the engineer and serves as the reference for defining the vehicle's navigation, guidance, and control systems.

In this work, the point **CO** is initially set to coincide with the center of gravity (**CG**) of the vehicle in its full configuration. This means the CG is calculated with all payloads and subsystems installed. However, if in future missions the drone's configuration is modified—such as through changes in weight, payload, or subsystem positioning—this would cause the center of gravity to shift, resulting in $\vec{r_g} \neq \vec{0}$. In such cases, the model will still reference the original configuration where **CO** = **CG**, calculated when the drone was in its fully configured state. Therefore the position vector r_g, will no longer be zero and the effect of this displacement will need to be accounted for in the dynamic model.

The rigid body dynamic equations, as formulated by Fossen [10], are expressed:

$$M_{RB}\dot{\nu} + C_{RB}(\nu)\nu = \tau_{RB} \tag{2.10}$$

where, M_{RB} is the rigid-body inertial matrix, defined as follows:

$$M_{RB} = \begin{bmatrix} mI_{3\times3} & -mS(r_g) \\ mS(r_g) & I_g \end{bmatrix} = \begin{bmatrix} m & 0 & 0 & 0 & mz_g & -my_g \\ 0 & m & 0 & -mz_g & 0 & mx_g \\ 0 & 0 & m & my_g & -mx_g & 0 \\ 0 & -mz_g & my_g & I_x & -I_{xy} & -I_{xz} \\ mz_g & 0 & -mx_g & -I_{yx} & I_y & -I_{yz} \\ -my_g & mx_g & 0 & -I_{zx} & -I_{zy} & I_z \end{bmatrix} \tag{2.11}$$

where:

- m is the mass of the vehicle;
- $I_{3\times3}$ is the identity matrix of size 3×3;
- $r_g = [x_g \quad y_g \quad z_g]^\top$ is the location of the CG with respect to the body frame;
- $S(\cdot)$ represents the skew-symmetric matrix of the vector;
- I_g is the inertial matrix defined as follows:

$$I_g = \begin{bmatrix} I_x & -I_{xy} & -I_{xz} \\ -I_{yx} & I_y & -I_{yz} \\ -I_{zx} & -I_{zy} & I_z \end{bmatrix}. \tag{2.12}$$

While C_{RB} is the rigid-body Coriolis and centripetal matrix which is expressed as:

$$C_{RB}(\nu) = \begin{bmatrix} 0_{3\times3} & -mS(\nu_1) - mS(\nu_2)S(r_g) \\ -mS(\nu_1) + mS(r_g)S(\nu_2) & -S(I_g\nu_2) \end{bmatrix} =$$

$$= \begin{bmatrix} 0 & 0 & 0 & m(y_gq + z_gr) & -m(y_gp + w) & -m(z_gp - v) \\ 0 & 0 & 0 & -m(x_gq - w) & m(z_gr + x_gp) & -m(z_gq + u) \\ 0 & 0 & 0 & -m(x_gr + v) & -m(y_gr - u) & m(x_gp + y_gq) \\ -m(y_gq + z_gr) & m(y_gp + w) & m(z_gp - v) & 0 & -I_{xz}p + I_zr & I_{yz}r + I_{xy}p - I_yq \\ m(x_gq - w) & -m(z_gr + x_gp) & m(z_gq + u) & I_{yz}q + I_{xz}p - I_zr & 0 & I_{xz}r + I_{xy}q + I_xp \\ m(x_gr + v) & m(y_gr - u) & -m(x_gp + y_gq) & -I_{yz}r - I_{xy}p + I_yq & -I_{xz}r - I_{xy}q - I_xp & 0 \end{bmatrix} \tag{2.13}$$

The term τ_{RB} is the generalized vector of external forces and moments expressed in $\{b\}$ and it is given as follows:

$$\tau_{RB} = \tau_{hs} + \tau_{hd} + \tau_{wind} + \tau_{waves} + \tau_p \tag{2.14}$$

where τ_{hs} is the contribution due to hydrostatic forces acting on the body, τ_{hd} is of hydrodynamic forces, τ_{wind} and τ_{waves} are forces and moments due to the wind effect and

the wave phenomena, respectively. τ_p represents forces and moments due to the propulsion system.

It is important to note that in the case of unmanned underwater vehicles, τ_{wind} and τ_{wave} can be neglected because usually, the operational depth is far from the surface, i.e., the contribution of these forces and moments is negligible.

2.3.1 Hydrostatic Forces

The hydrostatic forces (or restoring forces) are due to the combined effects of gravity and buoyancy acting on the body, whose equations are given below:

$$W = mg, \quad B = \rho g \nabla \tag{2.15}$$

here, W is the weight, B is the buoyancy force, g is the acceleration due to gravity, ρ is the water density, and ∇ is the displaced water volume. In vehicles such as Blucy and other UUVs, the buoyancy B is designed to slightly exceed the weight W, ensuring a state of positive buoyancy. This has a several key advantages:

- It enhances the *heave* control, allowing the vehicle to maintain or change its depth with minimal energy expenditure;
- It ensures *static stability* in roll and pitch, such that the vehicle naturally returns to an equilibrium orientation if perturbed;
- It allows for *automatic surfacing* in the event of system failure, as positive buoyancy will cause the vehicle to ascend to the surface.

Hydrostatic forces are inherently defined in the inertial (NED) frame which can be transformed into the body frame using a rotation matrix. The transformed force and moments are given by:

$$\tau_{hs} = -g(\eta) = -\begin{bmatrix} (W-B)\sin\theta \\ -(W-B)\cos\theta\sin\phi \\ -(W-B)\cos\theta\cos\phi \\ -(y_gW - y_bB)\cos\theta\cos\phi + (z_gW - z_bB)\cos\theta\sin\phi \\ (z_gW - z_bB)\cos\theta\cos\phi + (x_gW - x_bB)\cos\theta\cos\phi \\ -(x_gW - x_bB)\cos\theta\sin\phi - (y_gW - y_bB)\sin\theta \end{bmatrix} \tag{2.16}$$

where, $r_b = [x_b \quad y_b \quad z_b]^\top$ is the location of the Center of the Buoyancy (**CB**) from the origin of the body axis system **CO**. It is important to noticed that the relative position of **CG** and **CB** play a critical role in determining the vehicle's hydrostatic stability. By ensuring the **CB** is vertically above the **CG**, the vehicle benefits from a natural righting

moment. This is particularly important for maintaining stable operations in the presence of external disturbances, such as currents or unplanned maneuvers, where deviations from the desired orientation can occur.

2.3.2 Hydrodynamic Forces

Hydrodynamic forces and moments result from the interaction between a moving body and the surrounding fluid. These include inertial forces from added mass effects and damping forces due to skin friction, vortex shedding, and other factors. The hydrodynamic forces and moments vector is defined as follows:

$$\tau_{hd} = \begin{bmatrix} X_{hd} & Y_{hd} & Z_{hd} & K_{hd} & M_{hd} & N_{hd} \end{bmatrix}^\top \tag{2.17}$$

where, X_{hd}, Y_{hd} and Z_{hd} are the hydrodynamic forces along the x_b, y_b and z_b body axes respectively, whilst K_{hd}, M_{hd} and N_{hd} are the moments about x_b, y_b and z_b body axes respectively. These terms are obtained by integrating pressure distribution on the entire surface of the body. Given the complexity of this interaction, experimental data is often used to curve-fit these terms. The curve fitting of experimental data showed that this terms can be approximated using two key modelling approaches: truncated third-order odd function Taylor series [66] or second-order modulus expansion [67]. Each method is derived taking as example X_{hd}:

$$X_{hd} = X_{\dot{u}}\dot{u} + X_u u + X_{uuu}u^3 + X_{\dot{v}}\dot{v} + X_v v + X_{vvv}v^3 \cdots \tag{2.18}$$

$$X_{hd} = X_{\dot{u}}\dot{u} + X_u u + X_{u|u|}u\,|u| + X_{\dot{v}}\dot{v} + X_v v + X_{v|v|}v\,|v| \cdots \tag{2.19}$$

The truncated Taylor series expansion (2.18), introduces additional terms to represent the smooth variation of forces and moments in a differentiable function form. This approach increases mathematical precision, but it relies on number of terms of Taylor series expansion considered in the mathematical model. This lead to an excessive number of terms in which the higher order terms do not contribute much to the precision of mathematical modelling. On the other hand, the second-order modulus function (2.19) yields fewer terms, especially for dissipative terms like cross-flow drag and surge resistance, modeled as a sum of linear and quadratic damping. For this reason, hydrodynamic forces and moments are modeled by second-order modulus expansions, such that:

$$\tau_{hd} = -M_A\dot{\nu} - C_A(\nu)\nu - D_l\nu - D_n(\nu)\nu \tag{2.20}$$

In (2.20), according to Fossen [10], the coefficients of second order modulus expansion are organized into key matrices: the *added mass matrix* M_A, its associated *Coriolis matrix* $C_A(\nu)$, and the *damping matrix* $D(\nu)$, which includes both linear D_l and nonlinear $D_n(\nu)$ components.

The added mass is the additional mass experienced by an accelerating or a decelerating body in the fluid, that moves the volume of the fluid surrounding it. This is due to fact that body and the fluid cannot occupy the same physical space simultaneously. According to [68], the general expression for added mass comprise 36 constant parameters that are used to define the added mass matrix M_A:

$$M_A = -\begin{bmatrix} X_{\dot{u}} & X_{\dot{v}} & X_{\dot{w}} & X_{\dot{p}} & X_{\dot{q}} & X_{\dot{r}} \\ Y_{\dot{u}} & Y_{\dot{v}} & Y_{\dot{w}} & Y_{\dot{p}} & Y_{\dot{q}} & Y_{\dot{r}} \\ Z_{\dot{u}} & Z_{\dot{v}} & Z_{\dot{w}} & Z_{\dot{p}} & Z_{\dot{q}} & Z_{\dot{r}} \\ K_{\dot{u}} & K_{\dot{v}} & K_{\dot{w}} & K_{\dot{p}} & K_{\dot{q}} & K_{\dot{r}} \\ M_{\dot{u}} & M_{\dot{v}} & M_{\dot{w}} & M_{\dot{p}} & M_{\dot{q}} & M_{\dot{r}} \\ N_{\dot{u}} & N_{\dot{v}} & N_{\dot{w}} & N_{\dot{p}} & N_{\dot{q}} & N_{\dot{r}} \end{bmatrix} \tag{2.21}$$

As an example, each element in this matrix, such as $X_{\dot{u}}$, can be defined as [69]:

$$X_{\dot{u}} = \left.\frac{\partial X}{\partial \dot{u}}\right|_{\dot{u}=0} \tag{2.22}$$

Furthermore, the hydrodynamic Coriolis and centripetal matrix $C_A(\nu)$ can be defined:

$$C_A(\nu) = \begin{bmatrix} 0 & 0 & 0 & 0 & -a_3 & a_2 \\ 0 & 0 & 0 & a_3 & 0 & -a_1 \\ 0 & 0 & 0 & -a_2 & a_1 & 0 \\ 0 & -a_3 & a_2 & 0 & -b_3 & b_2 \\ a_3 & 0 & -a_1 & b_3 & 0 & -b_1 \\ -a_2 & a_1 & 0 & -b_2 & b_1 & 0 \end{bmatrix} \tag{2.23}$$

where

$$\begin{aligned} a_1 &= X_{\dot{u}}u + X_{\dot{v}}v + X_{\dot{w}}w + X_{\dot{p}}p + X_{\dot{q}}q + X_{\dot{r}}r \\ a_2 &= Y_{\dot{u}}u + Y_{\dot{v}}v + Y_{\dot{w}}w + Y_{\dot{p}}p + Y_{\dot{q}}q + Y_{\dot{r}}r \\ a_3 &= Z_{\dot{u}}u + Z_{\dot{v}}v + Z_{\dot{w}}w + Z_{\dot{p}}p + Z_{\dot{q}}q + Z_{\dot{r}}r \\ b_1 &= K_{\dot{u}}u + K_{\dot{v}}v + K_{\dot{w}}w + K_{\dot{p}}p + K_{\dot{q}}q + K_{\dot{r}}r \\ b_2 &= M_{\dot{u}}u + M_{\dot{v}}v + M_{\dot{w}}w + M_{\dot{p}}p + M_{\dot{q}}q + M_{\dot{r}}r \\ b_3 &= N_{\dot{u}}u + N_{\dot{v}}v + N_{\dot{w}}w + N_{\dot{p}}p + N_{\dot{q}}q + N_{\dot{r}}r \end{aligned} \tag{2.24}$$

As previously mentioned, viscous damping can be categorized into linear and quadratic forms. The significance of each type varies depending on the operational regime. For instance, in low-speed motion, linear damping typically prevails, whereas quadratic damping takes precedence in high-speed scenarios. Nevertheless, it's often crucial to incorporate

both linear and quadratic damping in models. This is because quadratic damping induces oscillatory behavior at low speeds, while linear damping facilitates exponential convergence to zero. Given that both oscillatory and exponential damping phenomena are observed in real-world scenarios, integrating both forms is essential for accurate representation dynamics. Thus, the matrices are defined as follows:

$$D_l = -\begin{bmatrix} X_u & X_v & X_w & X_p & X_q & X_r \\ Y_u & Y_v & Y_w & Y_p & Y_q & Y_r \\ Z_u & Z_v & Z_w & Z_p & Z_q & Z_r \\ K_u & K_v & K_w & K_p & K_q & K_r \\ M_u & M_v & M_w & M_p & M_q & M_r \\ N_u & N_v & N_w & N_p & N_q & N_r \end{bmatrix} \tag{2.25}$$

$$D_n(\nu) = -\begin{bmatrix} X_{u|u|}|u| & X_{v|v|}|v| & X_{w|w|}|w| & X_{p|p|}|p| & X_{q|q|}|q| & X_{r|r|}|r| \\ Y_{u|u|}|u| & Y_{v|v|}|v| & Y_{w|w|}|w| & Y_{p|p|}|p| & Y_{q|q|}|q| & Y_{r|r|}|r| \\ Z_{u|u|}|u| & Z_{v|v|}|v| & Z_{w|w|}|w| & Z_{p|p|}|p| & Z_{q|q|}|q| & Z_{r|r|}|r| \\ K_{u|u|}|u| & K_{v|v|}|v| & K_{w|w|}|w| & K_{p|p|}|p| & K_{q|q|}|q| & K_{r|r|}|r| \\ M_{u|u|}|u| & M_{v|v|}|v| & M_{w|w|}|w| & M_{p|p|}|p| & M_{q|q|}|q| & M_{r|r|}|r| \\ N_{u|u|}|u| & N_{v|v|}|v| & N_{w|w|}|w| & N_{p|p|}|p| & N_{q|q|}|q| & N_{r|r|}|r| \end{bmatrix} \tag{2.26}$$

However, Blucy is allowed only to move at low speed and also has starboard-port symmetry this suggests that the contribution from the off-diagonal elements will be much smaller when compared with diagonal elements. Furthermore, computation of these off-diagonal elements is very tedious task both theoretically as well as the experimentally. Hence, these terms can be neglected in M_A, which can be reduced as follows:

$$M_A = -diag\left\{X_{\dot{u}}, Y_{\dot{v}}, Z_{\dot{w}}, K_{\dot{p}}, M_{\dot{q}}, N_{\dot{r}}\right\} \tag{2.27}$$

accordingly, $C_A(\nu)$ becomes as follows:

$$C_A\left(v\right) = \begin{bmatrix} 0 & 0 & 0 & 0 & -Z_{\dot{w}}w & Y_{\dot{v}}v \\ 0 & 0 & 0 & Z_{\dot{w}}w & 0 & -X_{\dot{u}}u \\ 0 & 0 & 0 & -Y_{\dot{v}}v & X_{\dot{u}}u & 0 \\ 0 & -Z_{\dot{w}}w & Y_{\dot{v}}v & 0 & -N_{\dot{r}}r & M_{\dot{q}}q \\ Z_{\dot{w}}w & 0 & -X_{\dot{u}}u & N_{\dot{r}}r & 0 & -K_{\dot{p}}p \\ -Y_{\dot{v}}v & X_{\dot{u}}u & 0 & -M_{\dot{q}}q & K_{\dot{p}}p & 0 \end{bmatrix} \tag{2.28}$$

By applying similar assumptions, the components within D_l and $D_n(\nu)$ can also be simplified to include only diagonal terms. However, overlooking the off-diagonal elements leads to a misrepresentation of the nonlinear coupling dynamics. These assumptions are supported by the CFD simulations in Section 3.2, which are crucial in the design of autopilots

and control systems. Hence, the D_l and $D_n(\nu)$ are written as follows:

$$D_l = -\begin{bmatrix} X_u & 0 & 0 & 0 & 0 & 0 \\ 0 & Y_v & 0 & Y_p & 0 & Y_r \\ 0 & 0 & Z_w & 0 & Z_q & 0 \\ 0 & K_v & 0 & K_p & 0 & K_r \\ 0 & 0 & M_w & 0 & M_q & 0 \\ 0 & N_v & 0 & N_p & 0 & N_r \end{bmatrix} \tag{2.29}$$

$$D_n(\nu) = -\begin{bmatrix} X_{|u|u}|u| & 0 & 0 & 0 & 0 & 0 \\ 0 & Y_{|v|v}|v| & 0 & Y_{|p|p}|p| & 0 & Y_{|r|r}|r| \\ 0 & 0 & Z_{|w|w}|w| & 0 & Z_{|q|q}|q| & 0 \\ 0 & K_{|v|v}|v| & 0 & K_{|p|p}|p| & 0 & K_{|r|r}|r| \\ 0 & 0 & M_{|w|w}|w| & 0 & M_{|q|q}|q| & 0 \\ 0 & N_{|r|r}|r| & 0 & N_{|p|p}|p| & 0 & N_{|r|r}|r| \end{bmatrix} \tag{2.30}$$

2.4 6 DOF Models for UUV

Combining together (2.8), (2.10), (2.16) and (2.20), the complete six-degree-of-freedom model for underwater vehicle can be written as follows:

$$\dot{\eta} = J_\Theta(\eta)\nu \tag{2.31}$$

$$M\dot{\nu} + C(\nu)\nu + D(\nu)\nu + g(\eta) = \tau_p \tag{2.32}$$

where:

$$M = M_{RB} + M_A \qquad C(\nu) = C_{RB}(\nu) + C_A(\nu) \qquad D(\nu)\nu = D_l v + D_n(\nu)\nu \tag{2.33}$$

Furthermore, the six-degree-of-freedom model can be generalised considering the effect of the sea current, under the assumption of a 2D constant irrotational flow, introducing ν_r that is the relative velocity between the body and the fluid defined as:

$$\nu_r = \begin{bmatrix} u - u_c^b & v - v_c^b & w & p & q & r \end{bmatrix} \tag{2.34}$$

where u_c^b, and v_c^b are the body-fixed current velocities. The effect of sea currents can be incorporated into the dynamic (2.32) by using the relative motion under the assumption of a 2D irrotational flow:

$$M_{RB}\dot{\nu} + C_{RB}(\nu)\nu + M_A\dot{\nu_r} + C_A(\nu_r)\nu_r + D(\nu_r)\nu_r + g(\eta) = \tau_p \tag{2.35}$$

It is evident from equation (2.35) that the terms affected by the current are specifically those related to the hydrodynamics, namely $M_A\dot{\nu_r}+C_A(\nu_r)\nu_r+D(\nu_r)\nu_r$ and τ_p as discussed in 3.3.

Chapter 3

Parameters Identification

Introduction

This chapter outlines the methodologies employed for parameter identification in developing a benchmark model of Blucy UUV. The approach, built upon the work presented in [P3], introduces a novel end-to-end workflow, balancing experimental data and numerical simulations to accurately estimate the vehicles's parameters. This workflow can be generalized to other UUVs, making it a versatile tool for underwater vehicle modelling and simulation. By validating the benchmark with real mission data, the workflow ensures that the resulting model is robust to serve as benchmark for testing new control and guidance algorithm. In particular, the validated benchmark is used to test the novel control scheme proposed in Chapter 4.

As shown in Figure 3.1, the process includes a detailed sequence of steps to capture Blucy's physical, geometric, hydrodynamic and propulsive characteristics. The key stages of this workflow are:

- 3D Cad Modelling: develop a high fidelity 3D CAD model of Blucy, based on technical specifications, sensor data and physical measurements from the actual drone.

- Model Simplification and Meshing: preparing the CAD model for CFD simulations and added mass calculation by semplyfying and meshing it.

- CDF Simulations: Estimating the linear and non linear hydrodynamic damping coefficients through CFD simulations.

- Added Mass Calculation: determining the added mass matrix using AMCOMP software [36].

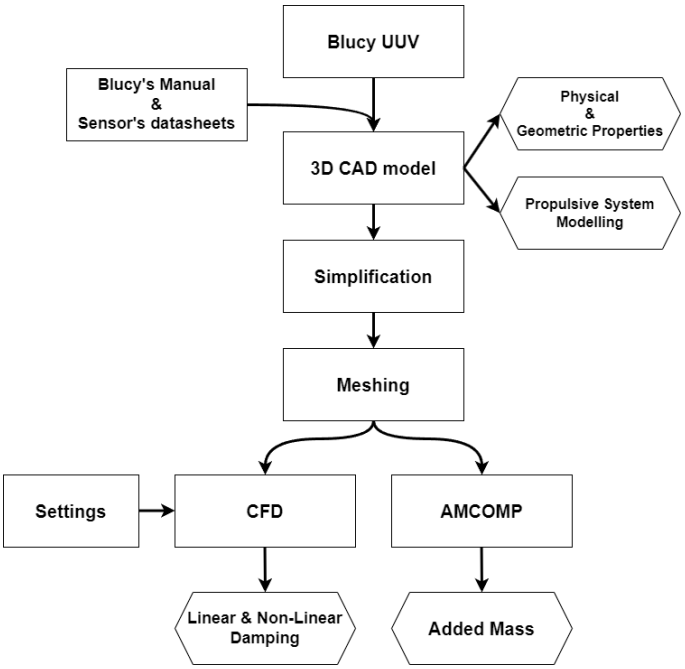

Figure 3.1: The workflow implemented for parameter identification.

- Propulsive system modelling: development of 4 quadrant model of thrusters based on experimental data and literature models [38, 66, 39]. Modelling of actuator dynamics based on the actual system.

Finally, the benchmark model is validated against real-mission data to ensure that the simulated results match the actual vehicle dynamics.

This chapter delves into each aspect of the workflow in detail, discussing the methods used for parameter identification, presenting the results, and exploring the challenges encountered during the process. The ultimate goal is to provide a validated benchmark of Blucy that can be used for the development of advanced control and guidance algorithms.

In this thesis, Blucy is considered in its complete configuration, which includes all the scientific payloads on board. It is worth observing that the developed workflow can easily be adapted to any configuration of the Blucy, though it is not demonstrated in this work. Demonstrating this is straightforward because the hydrodynamic and added mass parameters remain constant regardless of the drone's payload as do not change the outer structure of the drone. Only the mass, inertia, CG, CB, and thruster level arm change with the payload, and these adjustments can be easily and accurately incorporated into the CAD model and buoyancy calculator.

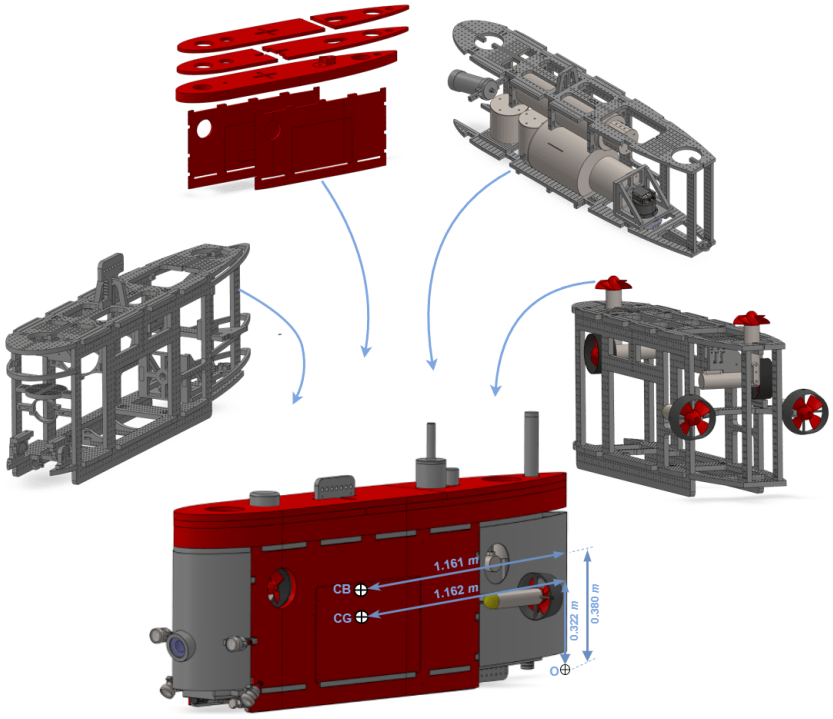

Figure 3.2: The complete assembly of Blucy's CAD model.

3.1 Physical and Geometric Properties

The physical and geometric properties of the drone are determined by analysing its 3D model, which is developed using CAD software such as SolidWorks (SW). This 3D model is built referencing the actual drone, the Blucy "Use and Maintenance" manual [70] and sensor datasheets. Special attention is given to accurately representing the masses of the custom components, especially those with complex geometries. Wherever possible, these components are physically weighed to ensure the highest accuracy. The complete assembly of all components, including internal subsystems and external structures, is depicted in Figure. 3.2.

The parameters obtained from the 3D CAD analysis are outlined in Table. 3.1. These parameters are calculated with reference to the **CG**, which is set as the origin of the body reference frame $\{b\}$. The position of the **CG** relative to the CAD reference frame origin (O), is illustrated in Figure. 3.2. In this study, the **CG** is treated as the center of the UUV, which simplifies the dynamic modeling by defining the CG as the origin of the body reference frame $\{b\}$. The **CG** location is thus set as:

$$r_g = \begin{bmatrix} x_g & y_g & z_g \end{bmatrix}^\top = \begin{bmatrix} 0 & 0 & 0 \end{bmatrix}^\top \tag{3.1}$$

Concerning the inertial parameters, they were automatically derived from SolidWorks with respect to the body axis centred in the **CG**. The inertia matrix in (2.12) of the

Parameter	Value
m	216.15 kg
volume	0.179 m^3
I_x	11.3114 $kg\ m^2$
I_y	49.2791 $kg\ m^2$
I_z	41.7449 $kg\ m^2$
I_{xy}	0 $kg\ m^2$
I_{xz}	2.8636 $kg\ m^2$
I_{yz}	0 $kg\ m^2$
r_g^O	$\begin{bmatrix}1.1622 & 0 & -0.3221\end{bmatrix}^\top$ m
r_b^O	$\begin{bmatrix}1.1622 & 0 & -0.3701\end{bmatrix}^\top$ m

Table 3.1: Physical and geometric parameters.

vehicle becomes:

$$I_g = \begin{bmatrix} 11.3114 & 0 & -2.8636 \\ 0 & 49.2791 & 0 \\ -2.8636 & 0 & 41.7449 \end{bmatrix} \tag{3.2}$$

It should be pointed out that $I_{xy} = I_{yx} = I_{yz} = I_{zy} = 0$ in (3.2), since the vehicle has starboard-port symmetry.

The position of the buoyancy centre (r_b) is determined by calculating the wet weight of each component using its volume from the CAD model and the fluid density (in this case, $\rho = 1025, \mathrm{kg/m}^3$). The position of the buoyancy center relative to the CAD reference frame origin, denoted as r_b^O, is computed using the following equation:

$$r_b^O = \begin{bmatrix} x_b^O & y_b^O & z_b^O \end{bmatrix}' = \begin{bmatrix} \frac{\sum_{i=1}^n B_i \cdot x_{gi}^O}{B} & \frac{\sum_{i=1}^n B_i \cdot y_{gi}^O}{B} & \frac{\sum_{i=1}^n B_i \cdot z_{gi}^O}{B} \end{bmatrix}' \tag{3.3}$$

where n is the total number of components in the assembly, B_i is the wet weight of the i^{th} component, and B is the sum of the wet weights of all components. r_b is calculated with respect to the CG, which serves as the origin of the body reference system, using the following equation:

$$r_b = r_g^O - r_b^O = \begin{bmatrix} 0 & 0 & -0.048 \end{bmatrix} m \tag{3.4}$$

where r_g^O is the CG in CAD reference frame.

Remark 3.1.1. *For different payload configurations, physical and geometric parameters must be recalculated based on the position of the new **CG**. This adjustment is necessary because the body reference frame $\{b\}$ is centered on **CG** position. Moreover in the complete configuration the wet mass of Blucy is $m_{Buoyancy} = 216.45\ kg$.*

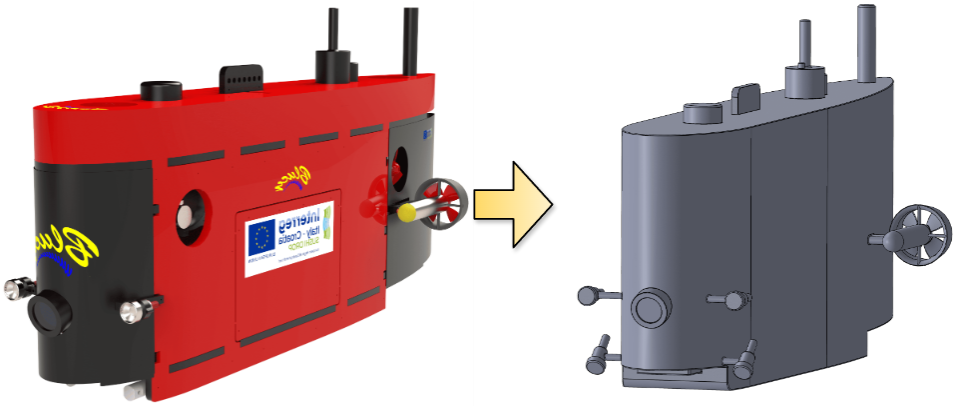

Figure 3.3: 3D CAD simplification for hydrodynamic parameters estimation

3.2 Hydrodynamic parameters

To derive hydrodynamic parameters and added mass coefficient, simplification are applied to the original 3D CAD model. These modification are necessary to streamline the model and make it more suitable for CFD simulations while preserving the key geometric features that affect hydrodynamic behaviour.

The simplified model (Figure. 3.3) exclude internal components and gaps, focusing instead on creating a solid volume with a smooth, continuous external surface. This reduction in complexity allows the model to capture the essential external flow interactions while minimizing unnecessary computational overhead. Additionally, the rotation of external thruster propellers is constrained, as their dynamic effects on the overall flow is not the primary focus at this stage. External cables and other small appendages are neglected, given their minimal impact on large-scale hydrodynamic forces. Furthermore, fillets were applied at the sharp edges of the model to smooth out transitions between surfaces. This refinement is crucial for avoiding unrealistic flow separations and turbulence that can arise at sharp corners, which would otherwise distort the accuracy of the CFD results. These simplifications ensure that the model remains representative of the actual vehicle's hydrodynamic behavior while maintaining computational efficiency for the parameter estimation process. The simplification are summarized in Table 3.2.

Two software tools are utilized for setting up and running the CFD simulations: OpenFOAM (OF) and SolidWorks (SW) Flow Simulation. OF was used to simulate Blucy's linear velocities in surge, sway, and heave, while SW Flow Simulation is employed to simulate the rotational motion, specifically the angular velocities around the roll, pitch, and yaw axes. The velocity ranges for the simulations are selected based on telemetry data collected from real-world missions, ensuring that the simulations accurately reflect Blucy's operational conditions. For surge, the velocity range is set to $(-0.8, 1.75)$ m/s, for sway $(-0.8, 0.8)$ m/s, and for heave $(-1.4, 1.4)$ m/s, with simulations conducted at increments

	Simplifications
Geometry	– all external holes and internal cavities were filled in order to have a continuous external surface – fillets were applied at every external edge – the original shapes of external elements, such as the mounts of the main thrusters and LEDs, were replaced by extruded cylinders – external cables were not taken into account – bottom of Blucy extremely simplified through plane surfaces
Setup	– external propellers were left rigidly in place (no rotation allowed during simulations) – the porosity of external surfaces was neglected

Table 3.2: CAD simplifications

of 0.2 m/s. These ranges capture the typical motion of Blucy during underwater operations. Similarly, angular motion simulations are guided by real-world scenarios observed during the missions. As a result, angular velocity simulations for roll, pitch, and yaw are constrained to a maximum of 10 degrees per second. While Blucy is primarily controlled in yaw, it is not specifically designed for complex rolling and pitching maneuvers. However, roll and pitch angular velocities may still occur due to hydrodynamic forces and environmental factors like sea currents, which are accounted for in the simulations.

3.2.1 Linear Motion Simulations

The external control volume is defined as a simple cuboid, with its eight vertices positioned relative to the vehicle's **CG** at the point $(0, 0, 0)$, as shown in Figure 3.4a. The volume is strategically enlarged in regions where wake formation is anticipated, enhancing the accuracy of the CFD analysis. For instance, during positive surge motion, the control volume is extended behind the vehicle, where the wake would predominantly develop. This approach is similarly applied to the wake size boxes, drone shells, and propellers, as illustrated in in the Figures. 3.4b and 3.4c. It's important to note, however, some distinctions between these elements. While the refinement boxes around the drone and propellers are kept consistent across all simulations, the wake box is the key variable that change depending on the expected wake region. Specifically, the volume of the wake box is substantially enlarged in regions where significant wake generation is anticipated.

Object	Length (m)		
	x	y	z
Control volume	32	20	21
Wake size box	6	4	5
Drone size box	2.25	0.84	1.2

Table 3.3: Volume and size boxes dimensions for surge simulations.

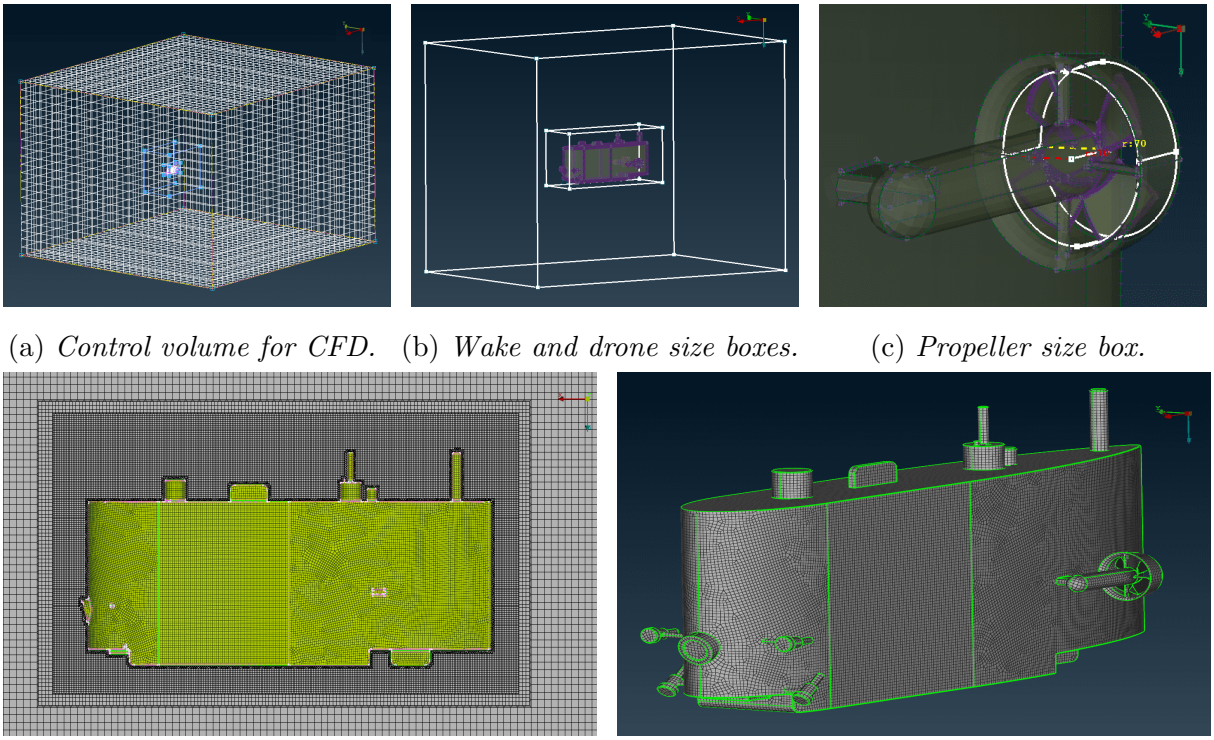

(a) *Control volume for CFD.* (b) *Wake and drone size boxes.* (c) *Propeller size box.*

(d) *Volume mesh detail: hexa interior.* (e) *Blucy surface mesh: tetra.*

Figure 3.4: Control volume and meshing details of OpenFoam.

The final dimensions of the control volume and refinement boxes for surge motion are detailed in Table 3.3. This setup ensured that the simulations captured the flow dynamics around the vehicle with higher precision, particularly in regions where turbulent wake effects are most pronounced.

In addition to defining the external dimensions of the cuboids, it is essential to specify the mesh spacing, as it plays a critical role in determining the numerical resolution of the simulation. Mesh spacing directly influences the accuracy of the results and the computational cost. To achieve an optimal balance between these factors, a grid convergence study is carried out for the surge motion case, examining three types of meshes: coarse, fine, and finest. The drag coefficient (C_D) is used as a measure of convergence. The drag coefficient is defined as $C_D = \frac{2D}{\rho U A}$, where D represents the drag force, U is the velocity

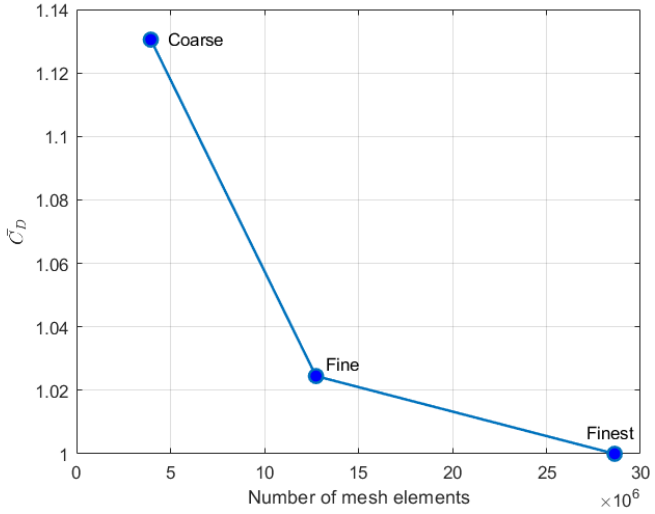

Figure 3.5: Grid convergence study of normalised drag coefficient $\bar{C}_D$ using three different mesh element sizing.

in the surge direction, and A is the reference area subjected to the drag force.

Figure 3.5 illustrates the results of the grid convergence study, where the number of mesh elements is plotted against the normalized drag coefficient ($\bar{C}_D$). The normalized drag coefficient is the ratio of the drag coefficient of each mesh to that of the finest mesh. The study revealed that the coarse mesh deviates from the finest mesh by approximately 12%. However, the difference between the fine and finest mesh is only about 2%, demonstrating a satisfactory level of convergence. Consequently, the fine mesh is selected as the optimal choice, balancing accuracy with the available computational resources. The final configuration of the fine mesh has an outer volume resolution that increases gradually from $1m$ at the boundaries to $0.25m$ near the drone surface, resulting in a total of $12,739,440$ mesh elements.

To solve the velocity and pressure fields, the steady-state Reynolds-Averaged Navier-Stokes (RANS) equations were employed using the SimpleFoam solver. This solver relies on the Semi-Implicit Method for Pressure-Linked Equations (SIMPLE) algorithm, which is well-suited for incompressible flow simulations. The k-ϵ turbulence model was adopted to account for turbulent flow behavior, requiring the resolution of two additional transport equations: one for the turbulence kinetic energy (k) and another for the turbulence dissipation rate (ϵ). This model strikes a balance between computational efficiency and accuracy, making it ideal for external flows around complex geometries such as Blucy. An inlet turbulence intensity of 0.1% is set to reflect the calm flow conditions typically encountered during the vehicle's operation.

Control volume	
x-size	$16\,m$
y-size	$16\,m$
z-size	$9\,m$
Hexa mesh	
Fluid cells	1 807 502
Fluid cells contacting solids	679 793
Maximum refinement level	5

Table 3.4: SolidWorks mesh parameters.

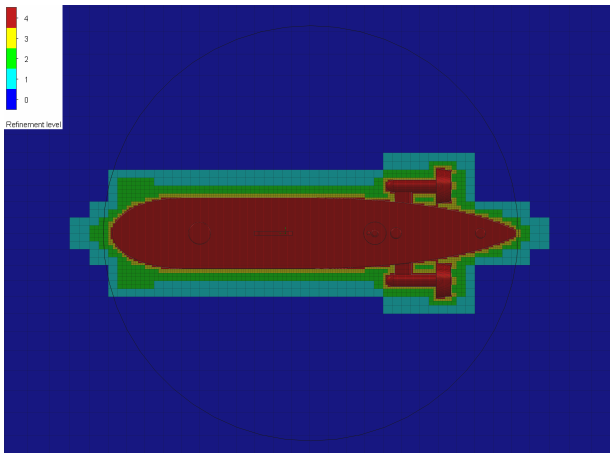

Figure 3.6: The mesh generated in the SolidWorks.

3.2.2 Angular Motion Simulations

The CFD simulations for angular motion are performed using SolidWorks (SW) Flow Simulation. The fluid density is set to 1025 kg/m^3 to represent saltwater, and the k-ϵ turbulence model is applied with an inlet turbulence intensity of 0.1%. SW Flow Simulation uses the Favre-Averaged Navier-Stokes (FANS) equations in steady-state mode, along with transport equations for turbulent kinetic energy (k) and dissipation rate (ϵ). The simulations focus on achieving convergence based on the forces and moments along and about the three principal body axes: x_b, y_b, and z_b, ensuring accuracy in the calculated hydrodynamic loads.

The mesh is generated directly within the SW Flow Simulation tool, followed by a convergence analysis similar to that performed for the linear velocity simulations. The final mesh characteristics are summarized in Table 3.4 and visually represented in Figure 3.6. This ensured that the mesh is sufficiently refined for accurate resolution of the flow field around the vehicle during angular motion simulations.

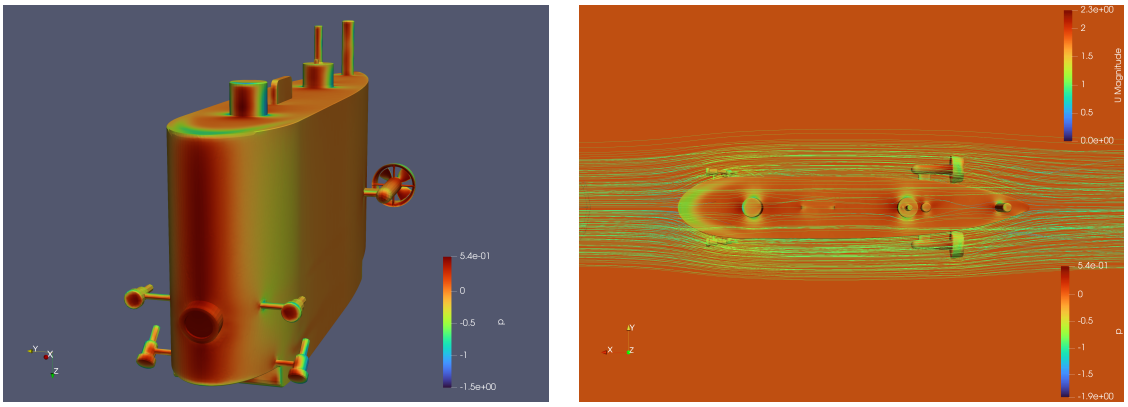

(a) *Pressure distribution.* (b) *Flow streamlines in top view.*

Figure 3.7: Pressure and flow streamlines of Surge motion simulated at 1 m/s.

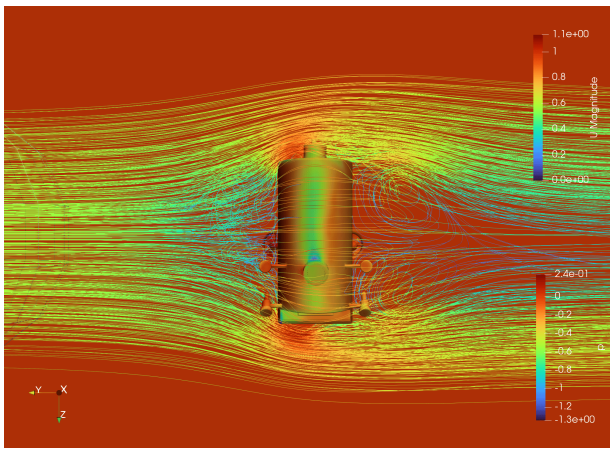

Figure 3.8: Pressure and flow streamlines of Sway motion simulated at 0.6 m/s.

3.2.3 CFD Simulations Results

The simulation results, which display the forces and moments generated at various velocity ranges, are illustrated in Figures 3.9-3.14. Figures 3.9-3.11 present the hydrodynamic responses for linear motions, including surge, sway, and heave. In contrast, Figures 3.12-3.14 show the corresponding results for angular motions, such as roll, pitch, and yaw. These simulations provide valuable insights into the behavior of the vehicle under different operating conditions, capturing the relationship between velocity and the resulting forces and moments. By examining these results, the impact of linear and quadratic damping effects can be better understood.

To ensure an accurate representation of the data, it is essential to identify the dominant forces and moments associated with each motion, while neglecting the contributions from non-dominant components. This approach simplifies the analysis by focusing on the most influential hydrodynamic factors. The dominant forces and moments are then fitted using

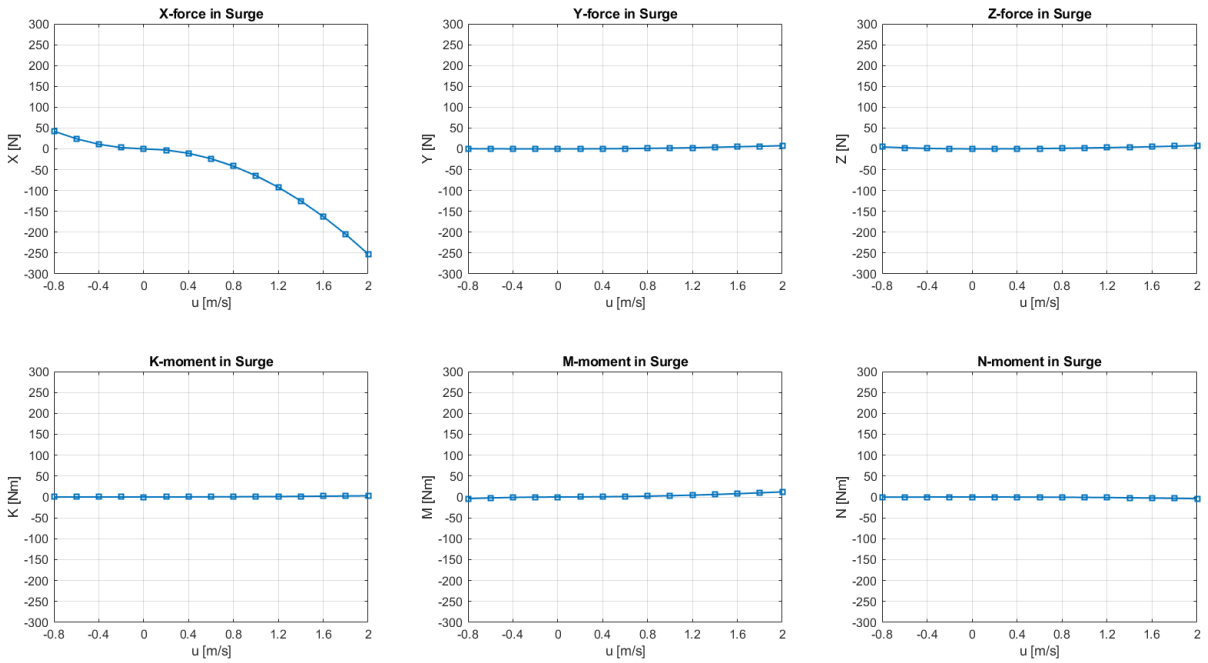

Figure 3.9: CFD simulation results of forces and moments in the surge.

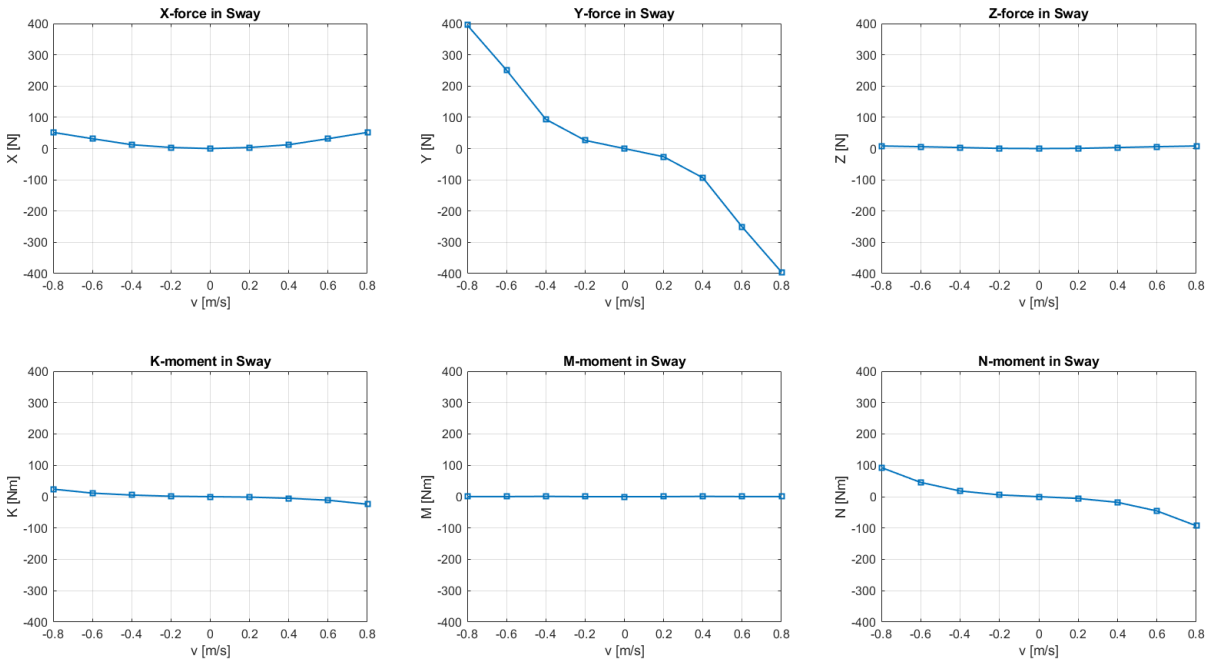

Figure 3.10: CFD simulation results of forces and moments in the sway.

a second-order modulus function, (2.19), which allows for the calculation of the linear and quadratic damping coefficients. This method effectively captures the non-linear behavior of the vehicle, particularly at higher velocities, where quadratic damping becomes more pronounced and significantly impacts the vehicle's overall dynamic response [10].

For instance, in the surge motion simulation conducted at 1 m/s, the pressure distri-

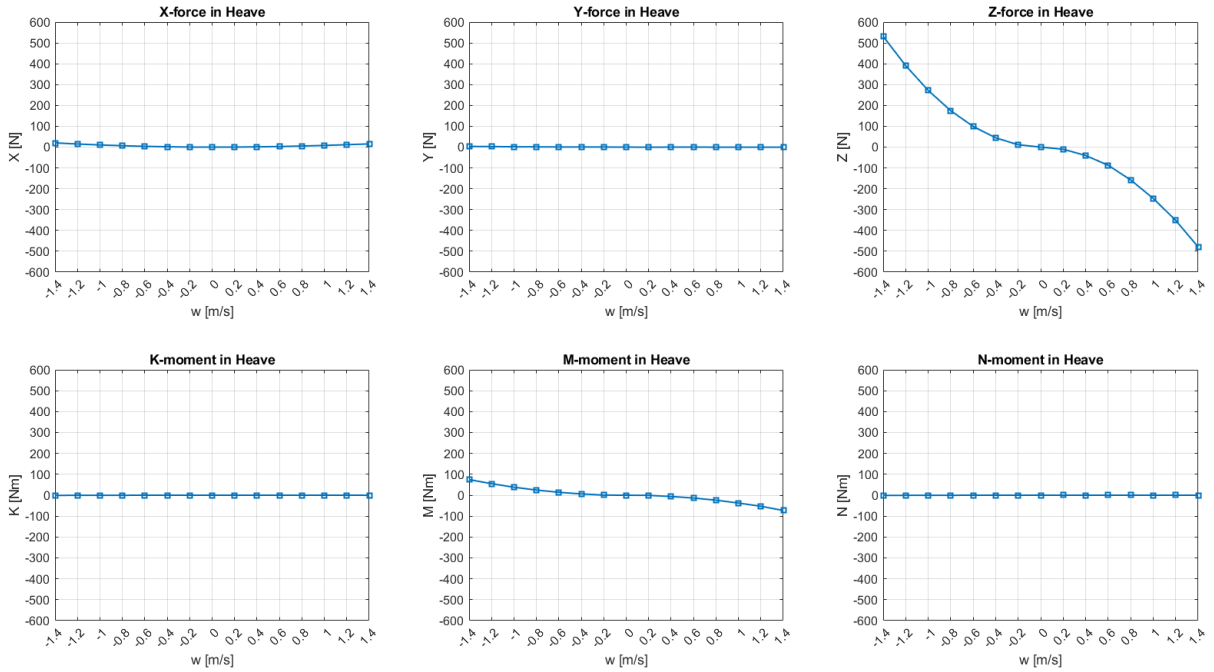

Figure 3.11: CFD simulation results of forces and moments in the heave.

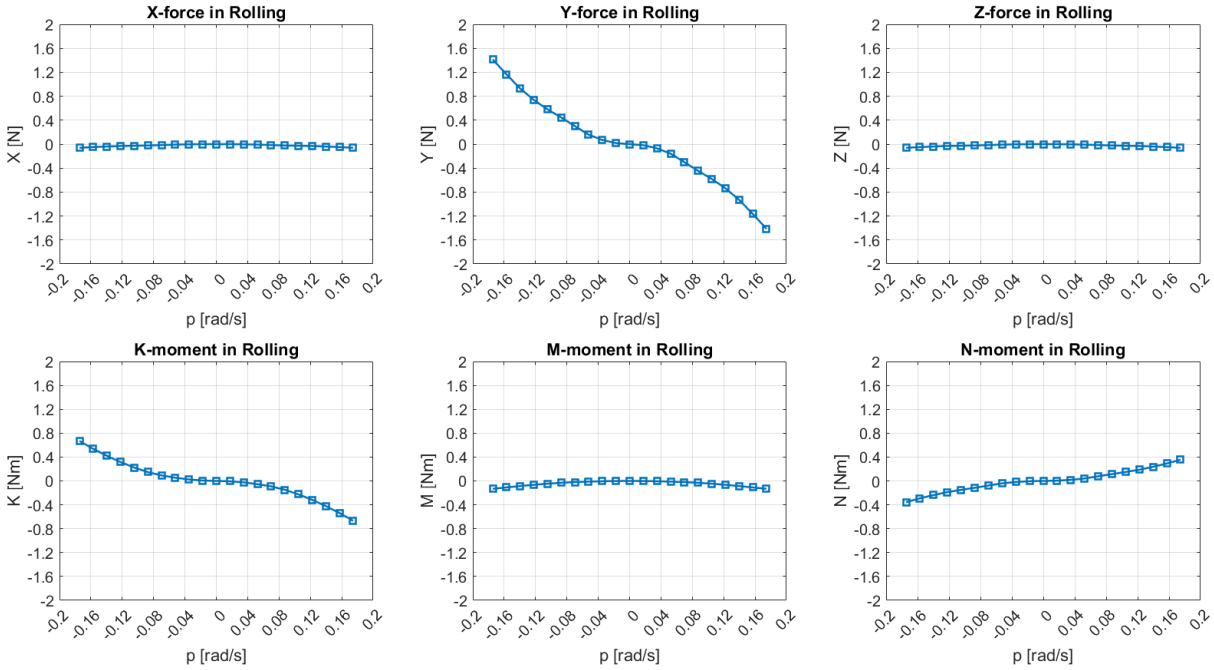

Figure 3.12: CFD simulation results of forces and moments in the rolling.

bution and flow field, shown in Figures 3.7a and 3.7b, reveal the formation of a distinct wake behind Blucy, indicating significant flow separation. The primary contributors to this flow disturbance are the propulsive thrusters and the cylindrical components located on the top of the drone. These features amplify turbulence and consequently increase drag, particularly in the rear section of the vehicle, which predominantly generates drag forces X in the x_b axis. Due to the symmetry of Blucy, the net force in the y_b direction

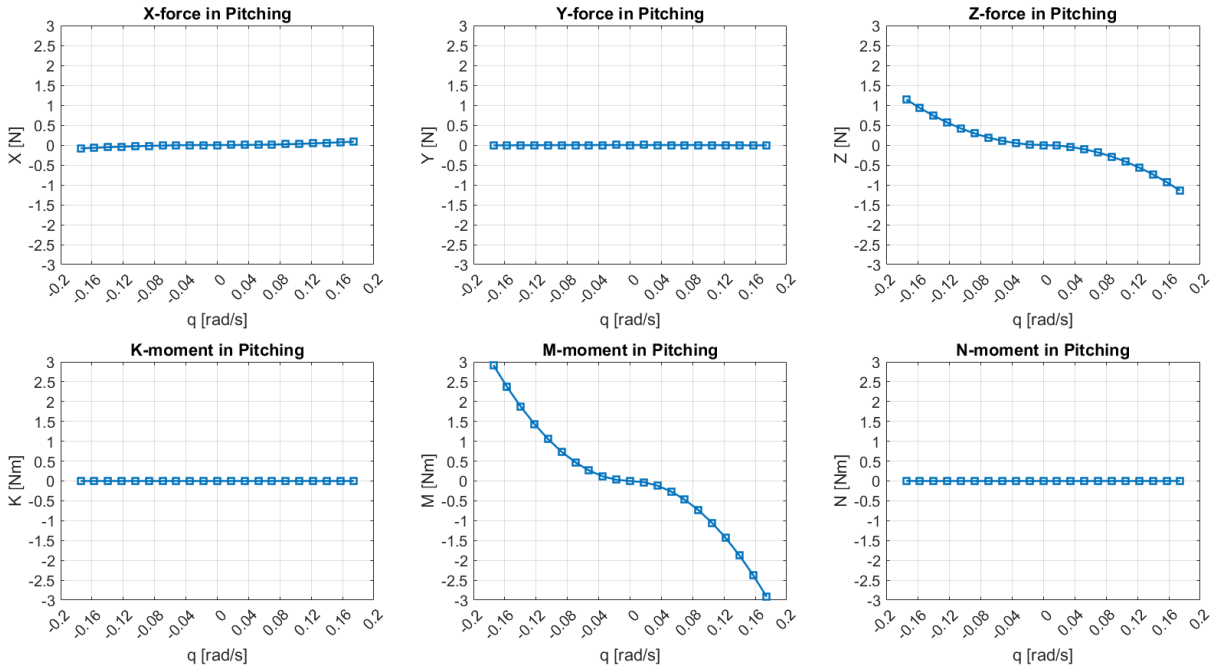

Figure 3.13: CFD simulation results of forces and moments in the pitching.

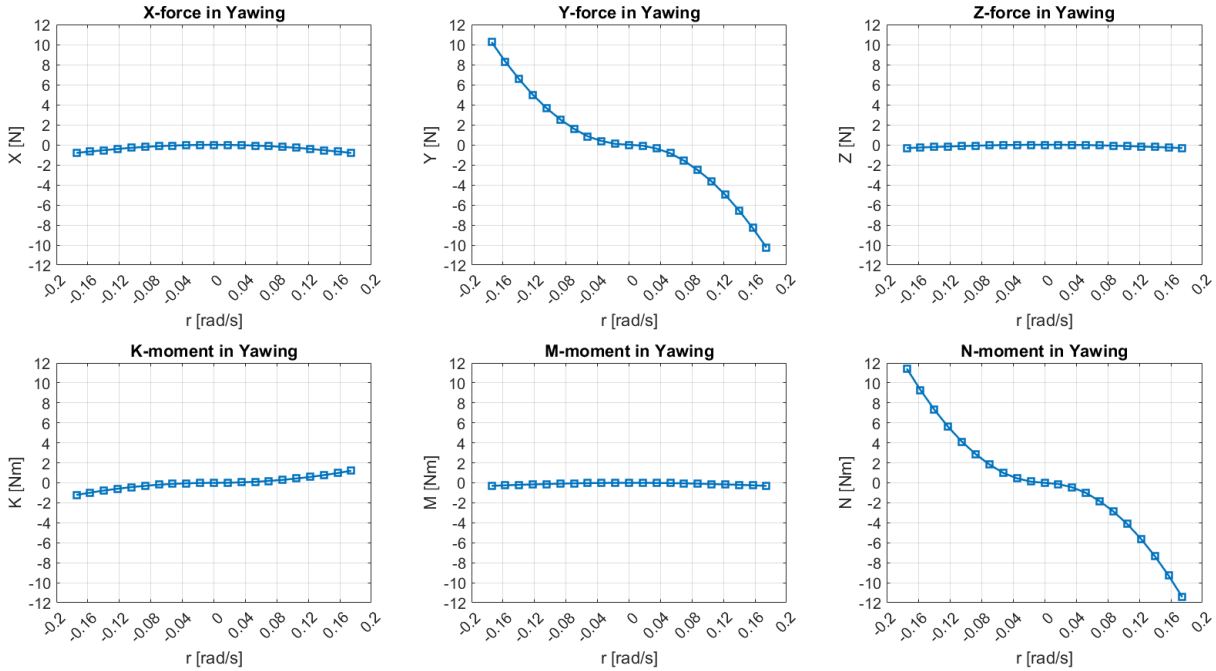

Figure 3.14: CFD simulation results of forces and moments in yawing.

remains zero, as the pressure distribution about the y_b axis cancels out when integrated.

As observed from the simulation results in Figure. 3.9, the force X along the x_b axis is clearly dominant, aligning with the predictions made in Section 2. This dominance allows the force in the surge direction to be accurately modeled using a second-order modulus

function, as described in (2.19), which can be expressed as:

$$X(u) = X_u u + X_{u|u|} u|u|. \tag{3.5}$$

This methodology is applied to all motion types, with the major components of the linear and quadratic hydrodynamic damping coefficients summarized in Table 3.5. From the table, it is clear that each motion has dominant forces or moments that exert more influence than the others. However, secondary forces and moments are also generated due to the nonlinear coupling of motions. For example, in the sway simulation (Figure 3.10), the primary force is Y along y_b direction, driven by the wake generated along the sides of the vehicle, as shown in Figure 3.8. Secondary effects, such as the K and N moments, arise due to the lack of symmetry about the x_b and z_b axes, respectively. These moments result from the overall integration of the pressure distribution, which is uneven due to the vehicle's geometry.

By referring to the calculated coefficients in Table 3.5, the matrices in (2.29) and (2.30) are updated to incorporate these effects:

$$D_l = -\begin{bmatrix} -2.61 & 0 & 0 & 0 & 0 & 0 \\ 0 & -24.72 & 0 & -1.43 & 0 & -1.87 \\ 0 & 0 & -2.82 & 0 & -0.07 & 0 \\ 0 & 0.83 & 0 & -0.04 & 0 & 0.14 \\ 0 & 0 & -1.71 & 0 & -0.06 & 0 \\ 0 & -11.21 & 0 & 0.41 & 0 & -0.044 \end{bmatrix} \tag{3.6}$$

$$D_n(\nu) = -\begin{bmatrix} -61.82|u| & 0 & 0 & 0 & 0 & 0 \\ 0 & -597.62|v| & 0 & -38.14|p| & 0 & -342.89|r| \\ 0 & 0 & -255.86|w| & 0 & -37.19|q| & 0 \\ 0 & -30.05|v| & 0 & -23.68|p| & 0 & 41.28|r| \\ 0 & 0 & -38.7|w| & 0 & -95.69|q| & 0 \\ 0 & -85.4|r| & 0 & 9.28|p| & 0 & -375.53|r| \end{bmatrix} \tag{3.7}$$

Motion	Linear	Quadratic
Surge	$X_u = -2.61$	$X_{u\|u\|} = -61.82$
Sway	$Y_v = -24.72$	$Y_{v\|v\|} = -597.62$
	$K_v = 0.83$	$K_{v\|v\|} = -30.05$
	$N_v = -11.21$	$N_{v\|v\|} = -85.4$
Heave	$Z_w = -2.82$	$Z_{w\|w\|} = -255.86$
	$M_w = -1.71$	$M_{w\|w\|} = -38.7$
Roll	$Y_p = -1.43$	$Y_{p\|p\|} = -38.14$
	$K_p = -0.04$	$K_{p\|p\|} = -23.68$
	$N_p = 0.41$	$N_{p\|p\|} = 9.28$
Pitch	$Z_q = -0.07$	$Z_{q\|q\|} = -37.19$
	$M_q = -0.06$	$M_{q\|q\|} = -95.69$
Yaw	$Y_r = -1.87$	$Y_{r\|r\|} = -342.98$
	$K_r = 0.14$	$K_{r\|r\|} = 41.28$
	$N_r = -0.044$	$N_{r\|r\|} = -375.53$

Table 3.5: Hydrodynamic damping coefficients obtained after fitting the CFD data.

3.2.4 Added Mass Parameters

The computation of added mass is facilitated by AMCOMP, a research CAD tool developed by the University of Bologna in collaboration with the Royal Melbourne Institute of Technology [36]. This software is developed using C++ without reliance on external third-party libraries. It utilizes the Stereo Lithography (STL) format that discretizes the external CAD body into triangles for added mass calculations. Common software like Solidworks supports saving CAD files in the STL format. AMCOMP boasts a user-friendly interface, allowing for easy loading of STL files and parameter adjustments such as density within its environment.

The mathematical framework behind the computation of the added mass involves solving the potential flow around the body. The potential flow is governed by Laplacian equation given below:

$$\nabla^2 \Phi = 0 \tag{3.8}$$

where ∇ is the Laplacian operator and Φ is velocity potential field that depends only on the surface shape in a closed control volume. The flow is subjected to the following boundary conditions:

1. The watertight condition:
$$\left.\frac{\mathrm{d}\Phi}{\mathrm{d}\hat{n}}\right|_S = u_n \tag{3.9}$$
where $\hat{n}$ is the unit vector normal to surface, while the u_n is projection of velocity vector on to normal $\hat{n}$ of a point on the body.

2. The stationary condition:
$$\lim_{r\to\infty}\frac{\mathrm{d}\Phi}{\mathrm{d}r} = 0 \tag{3.10}$$
where the r is the distance between the origin and the fluid point that is far enough from the influence of perturbation of the fluid.

3. Kutta condition: This condition is important to ensure continuous pressure distribution and smooth flow that is leaving the trailing edge.

The above problem is applied to the discretized finite elements body and the unknown potential Φ is computed by solving the linear algebraic system of equation give by the following equation:

$$2\pi\Phi_i(P) = \sum_{\substack{j=1\\(i\neq j)}}^{N_B}\Phi_j\left(Q_j\right)C_{ij} - \sum_{j=1}^{N_B}\frac{\partial\Phi}{\partial\hat{n}}\left(Q_j\right)B_{ij}, \quad i = 1,2,3\ldots N_B \tag{3.11}$$

where, P represents the point field, while Q denotes the point source. N_B denotes the number of elements on the body. The terms C_{ij} and B_{ij} describe the influence exerted by the j-th element on the control point of the i-th element. These coefficients can be determined using the following expressions:

$$C_{ij} = \int_{S_B}\frac{\partial}{\partial\hat{n}_j}\left(\frac{1}{\vec{r}_{ij}}\right)\mathrm{d}S + \int_{S_W}\frac{\partial}{\partial\hat{n}_j}\left(\frac{1}{\vec{r}_{ij}}\right)\mathrm{d}S = \int_{S_B}\frac{\overrightarrow{r}_{ij}\bullet\hat{n}_j}{\vec{r}_{ij}^{\,3}}\mathrm{d}S_j + \int_{S_W}\frac{\vec{r}_{ij}\bullet\hat{n}_j}{\overrightarrow{r}_{ij}^{\,3}}\mathrm{d}S_j \tag{3.12}$$

$$B_{ij} = \int_{S_B}\frac{1}{\overrightarrow{r_{ij}}}\mathrm{d}S_j \tag{3.13}$$

The symbol $\vec{r}_{ij}$ denotes the vector connecting the i_{th} and j_{th} elements. While, S_B representing the external surface of the body and S_W symbolizing the surface of the wake. By substituting (3.8) into (3.11), following matrix equation is obtained:

$$[2\pi\delta - C]_{N_B\times N_B}\{\phi\}^k_{N_B\times 1} = [B]_{N_B\times N_B}\left\{\frac{\partial\phi}{\partial\widetilde{n}}\right\}^k_{N_B\times 1} \tag{3.14}$$

where δ_{ij} is the Kronecker delta function. To obtain the unit flow potential, the solution

procedure involves iterating through following six boundary conditions:

$$\left\{\frac{\partial\Phi}{\partial\hat{n}}\right\}^k = \begin{cases} \alpha & k=1 \\ \beta & k=2 \\ \gamma & k=3 \\ (\gamma y - \beta z) & k=4 \\ (\alpha z - \gamma x) & k=5 \\ (\beta x - \alpha y) & k=6 \end{cases} \tag{3.15}$$

where, α, β, and γ represent the normal direction cosines of each boundary element on the surface, while x, y, and z denote the position of the element's center of gravity relative to the pole, which serves as the reference point for computing the rotational terms of the inertia.

Following the computation of flow potential Φ, the 6×6 added mass matrix can be obtained using the following expression:

$$M_A = \rho \begin{bmatrix} \sum_{i=1}^{N_B} \Phi_i \left\{\frac{\partial\Phi}{\partial\hat{n}}\right\}_i \mathrm{d}s_i & \cdots & \sum_{i=1}^{N_B} \Phi_i \left\{\frac{\partial\Phi}{\partial\hat{n}}\right\}_i \mathrm{d}s_i \\ \cdots & \cdots & \\ \sum_{i=1}^{N_B} \Phi_i \left\{\frac{\partial\Phi}{\partial\hat{n}}\right\}_i \mathrm{d}s_i & \cdots & \sum_{i=1}^{N_B} \Phi_i \left\{\frac{\partial\Phi}{\partial\hat{n}}\right\}_i \mathrm{d}s_i \end{bmatrix} \tag{3.16}$$

herein, ρ is the density of the fluid surrounding the body, s_i is the surface of the i^{th} discretised element, N_B is the total number of elements into which the surface of the body is divided, and Φ_i is the unknown potential obtained by solving the Laplacian problem.

The solution of the problem depends on the number of elements considered for computation. In this case, the number of elements is the same as in the CFD analysis (fine mesh), as this configuration provides reliable results, as demonstrated in Section 3.2.

The AMCOMP uses the properties of the linear system of equations and the Gaussian elimination method to solve the above described numerical problem. Since Blucy moves at low speed and has starboard-port symmetry, the M_A has the same form of (2.27). The computed added mass values are summarised in the Table. 3.6, so the obtained M_A matrix is:

$$M_A = -diag\left\{-28.94, -166.03, -94.13, -0.0758, -17.10, -33.58\right\} \tag{3.17}$$

Remark 3.2.1. *Hydrodynamic parameters remain valid as long as different payload configurations do not alter the outer shape of the vehicle.*

Coefficient	Values
$X_{\dot{u}}$	-28.9440 kg
$Y_{\dot{v}}$	-166.0392 kg
$Z_{\dot{w}}$	-94.1328 kg
$K_{\dot{p}}$	-0.0758 $kg\,m^2$
$M_{\dot{q}}$	-17.1097 $kg\,m^2$
$N_{\dot{r}}$	-33.5838 $kg\,m^2$

Table 3.6: Added mass coefficients computed using AMCOMP.

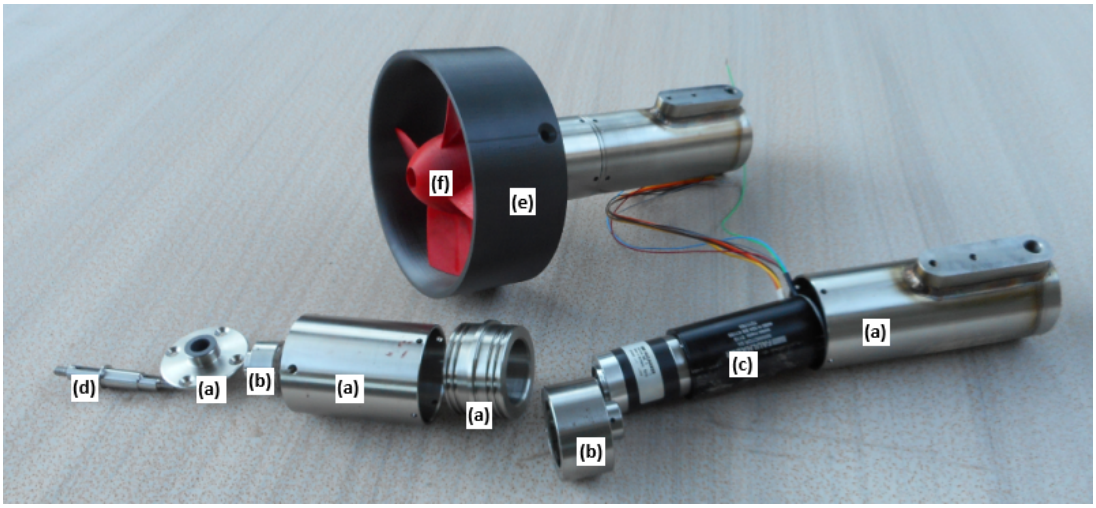

Figure 3.15: Thruster components:(**a**) Canister components; (**b**) Magnetic couplings; (**c**) Brushless servomotors: Faulhaber DC 4490H036BS 38A; (**d**) Propeller shaft; (**e**) Kaplan series kort 19A nozzle; (**f**) Wageningen Kaplan series Ka 4-70 propeller.

3.3 Propulsive System Modelling

Blucy is an underactuated vehicle with inherent high pitch and roll stability that enhances control over x, y, z, u, v, w, r, and ψ variables during the different survey operations. This stability ensures the vehicle remains balanced and maintains its orientation, which is crucial for precise data collection. The vehicle is equipped with a total of six thrusters: two horizontal, two vertical, and two lateral. The horizontal thrusters are positioned behind the **CG**, one on the port side and the other on the stern side, with each featuring counter rotating propellers. This counter rotation cancels out roll torque, ensuring that the vehicle maintains its stability during horizontal maneuvers. The vertical thrusters, designed to control depth, are installed atop the vehicle. One is located at the rear, while the other is positioned at the front, both relative to the **CG**, with propellers rotating in the same direction. The lateral thrusters, positioned at the bow and stern,

Number	Location	Propeller	Position $l(m)$	Thrust versor e
TH 1	Rear, starboard	Propulsive	[-0.821, 0.230, -0.008]	[1, 0, 0]
TH 2	Rear, port	Propulsive	[-0.821, -0.230, -0.008]	[1, 0, 0]
TH 3	Front, top	Manoeuvre	[0.615, 0, -0.386]	[0, 0, 1]
TH 4	Rear, top	Manoeuvre	[-0.835, 0, -0.386]	[0, 0, 1]
TH 5	Front, port	Manoeuvre	[0.490, -0.113, -0.131]	[0, 1, 0]
TH 6	Rear, starboard	Manoeuvre	[-0.660, 0.124, -0.131]	[0, 1, 0]

Table 3.7: Position of the motors from the centre of gravity and versor pointing the direction of the thrust produced.

are primarily allocated for yaw control, enabling precise rotational maneuvers around the z-axis. However, if there is any remaining thrust capacity after yaw control, the lateral thrusters can also contribute to sway control, assisting in lateral movements along the y-axis. The positions of these actuators relative to the centre of gravity (**CG**) are outlined in Table. 3.7.

Remark 3.3.1. *Position of actuator, relative to the **CG**, varies depending on the payloads configuration. In work, these distances are measured with respect to Blucy **CG** in its complete configuration.*

3.3.1 Thrust and Torque Modelling

The thrusters consist of Kaplan Ka 4-70 series ducted propellers with pitch ratio (P/D) of 1.28, diameter ($D = 0.145m$), and area ratio (A_e/A_o) of 0.7, paired with 19A ducts [38, 71, 40] as shown in Figure.3.15. The propellers are categorised into two distinct types: propulsive and manoeuvring. Propulsive propellers are dedicated to surge motion while manoeuvring ones are used for heave, sway, or yaw motions. The distinction arises from the symmetry of the propeller blades according to their intended functionalities. Propulsive blades are asymmetrical and are optimised for efficiency at high rotational speed in surge motion. In contrast, manoeuvring blades are symmetrical, optimised for lower rotational speed, and have balanced performance characteristics in pushing or pulling.

The thrust and torque generated by the thrusters are described using non-dimensional coefficients, denoted as C_T and C_Q, respectively, as functions of the advance ratio J. These

coefficients C_T, C_Q, and J are computed using the following equations:

$$\begin{aligned} C_T &= \frac{T}{\rho n^2 D^4} \\ C_Q &= \frac{Q}{\rho n^2 D^5} \\ J &= \frac{V_a}{nD} \end{aligned} \tag{3.18}$$

where T and Q are the thrust and torque respectively, V_a is the inflow velocity, n is the rotational speed of the propeller expressed in rotation per second (rps) and D is the diameter of the propeller.

Several tests have been conducted by the Maritime Research Institute Netherlands (MARIN) to evaluate these coefficients, with their findings documented in various reports. A valuable reference for this series of propeller test can be found in [71, 40], from which regression polynomials have been developed to express C_T and C_Q as functions of P/D and advance ratio J:

$$\begin{aligned} C_T = {} & A_{0,0} + A_{0,1}J + \_\ \_\ \_\ + A_{0,6}J^6 + \\ & + A_{1,0}\left(\frac{P}{D}\right) + A_{1,1}\left(\frac{P}{D}\right)J + \_\ \_\ \_ + A_{1,6}\left(\frac{P}{D}\right)J^6 + \\ & + A_{2,0}\left(\frac{P}{D}\right)^2 + A_{2,1}\left(\frac{P}{D}\right)^2 J + \_\ \_\ \_ + A_{2,6}\left(\frac{P}{D}\right)^2 J^6 + \\ & + \_\ \_\ \_\ \_\ \_\ \_\ \_\ \_\ \_\ \_\ \_\ \_\ \_\ \_\ \_ + \\ & + A_{6,0}\left(\frac{P}{D}\right)^6 + A_{6,1}\left(\frac{P}{D}\right)^6 J + \_\ \_\ \_ + A_{6,6}\left(\frac{P}{D}\right)^6 J^6 \end{aligned} \tag{3.19}$$

$$\begin{aligned} C_Q = {} & C_{0,0} + C_{0,1}J + \_\ \_\ \_\ \_\ \_\ \_\ \_\ \_\ \_\ \_\ \_\ \_\ \_\ \_ \\ & \_\ \_\ \_\ \_\ \_\ \_\ \_\ \_\ \_\ \_\ \_\ \_\ \_\ \_ + C_{6,6}\left(\frac{P}{D}\right)^6 J^6 \end{aligned} \tag{3.20}$$

where $A_{i,j}$ and $C_{i,j}$ are documented in [39, 71]. It is important to emphasize that the polynomials in (3.19) and (3.20) provide accurate approximations for high-area ratio Ka propellers series. However, for propellers with lower area ratios, such those considered in this work, these models tend to overestimate the behaviour. To address this issue, open-water tests were conducted at zero inflow velocity of $V_a = 0$ for both propulsive and manoeuvring propellers. These experiments were performed in a tank, with the thruster controlled by an in-built velocity controller (Faulhaber MCLM3006S RS) that logs the rotational speed of the propeller using an internal speed sensor. The thruster were mounted in the tank using a beam equipped with a strain gauge, to measure both thrust and torque. The experimental tests cover both positive and negative rps values. Even though these tests do not cover the entire operating regime of the thrusters, the

results are used to scale the polynomial approximation (3.20),(3.19) , thus developing a more accurate and comprehensive model. This scaling ensures that the theoretical C_T and C_Q values more accurately reflect the real behavior of the propellers considered in this work.

Figure.3.16 illustrates the refined C_T and C_Q curves as functions of J. It can be observed that the reduction factors for the propulsive and manoeuvring propellers due in rps are 0.811 and 0.9, respectively, consistent with their optimised operating conditions. Additionally, the propulsive propeller (Figure. 3.16a) generates greater thrust compared to the manoeuvring propeller (Figure. 3.16b), although the latter produces nearly identical thrust in both directions of rotation. The overall C_Q of the manoeuvring thruster is higher compared to the propulsive ones.

The description above has focused primarily on the first quadrant performance of propellers, where the propellers operate with positive rotational speed and forward or zero advance velocity. This is the typical mode of operation for propulsive thrusters in the ahead operating condition. However, to study maneuvering situations, a more generalized dataset is required, particularly for the maneuvering propellers.

Using C_T and C_Q as functions of the advance ratio J can be impractical when dealing with reverse or low-speed operations due to the occurrence of singularities and numerical inconsistencies, especially when the inflow velocity V_a and rotational speed n are reversed. This limitation arises because the advance ratio J does not account for the flow direction relative to the propeller, making it challenging to accurately model the behavior during reverse or complex maneuvering scenarios.

To address this, propeller coefficients are expressed in relation to the advance angle β, which is calculated at 70% of the propeller tip radius defining the four quadrant operation:

$$\beta = \tan^{-1}\left(\frac{V_a}{0.7\pi nD}\right) = \tan^{-1}\left(\frac{J}{0.7\pi}\right) \tag{3.21}$$

- *1st quadrant*: $n > 0$ and $V_a > 0$ with $0° \leq \beta < 90°$
- *2nd quadrant*: $n > 0$ and $V_a < 0$ with $90° < \beta \leq 180°$
- *3rd quadrant*: $n < 0$ and $V_a < 0$ with $180° < \beta \leq 270°$
- *4th quadrant*: $n < 0$ and $V_a > 0$ with $270° < \beta \leq 360°$

The angle β effectively represents the local inflow angle at 70% of the propeller radius, which corresponds closely to the typical location of maximum blade loading. This approach accounts for the number of blades and their geometric distribution along the propeller disc, factors that significantly influence thrust and torque characteristics.

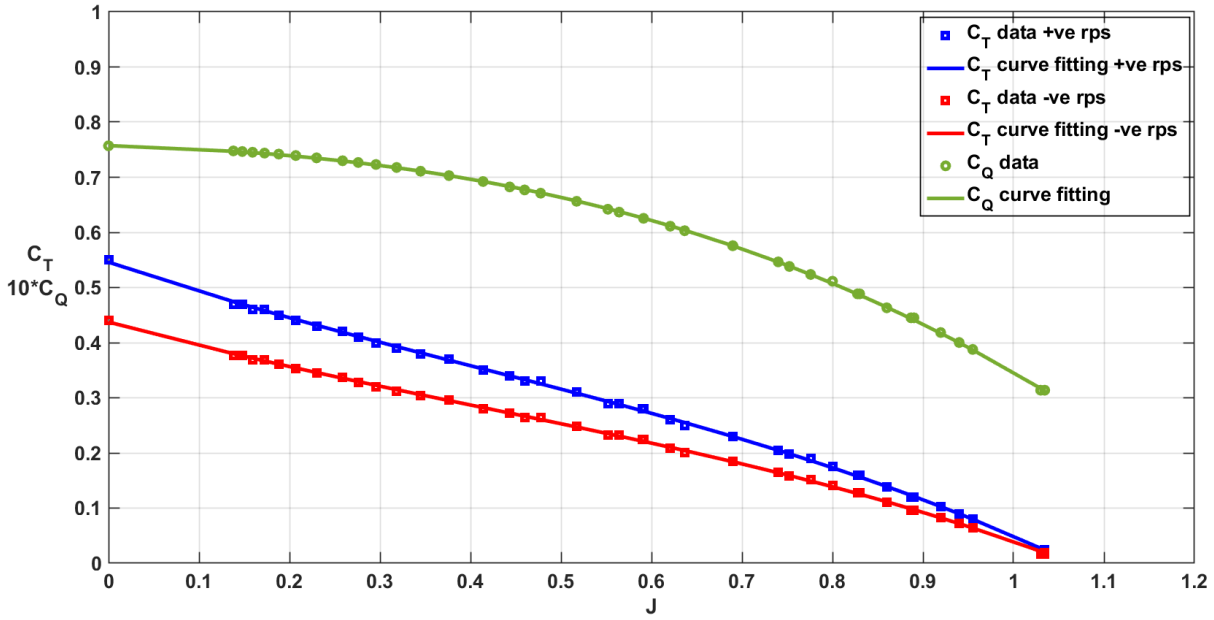

(a) *Propulsive thrusters.*

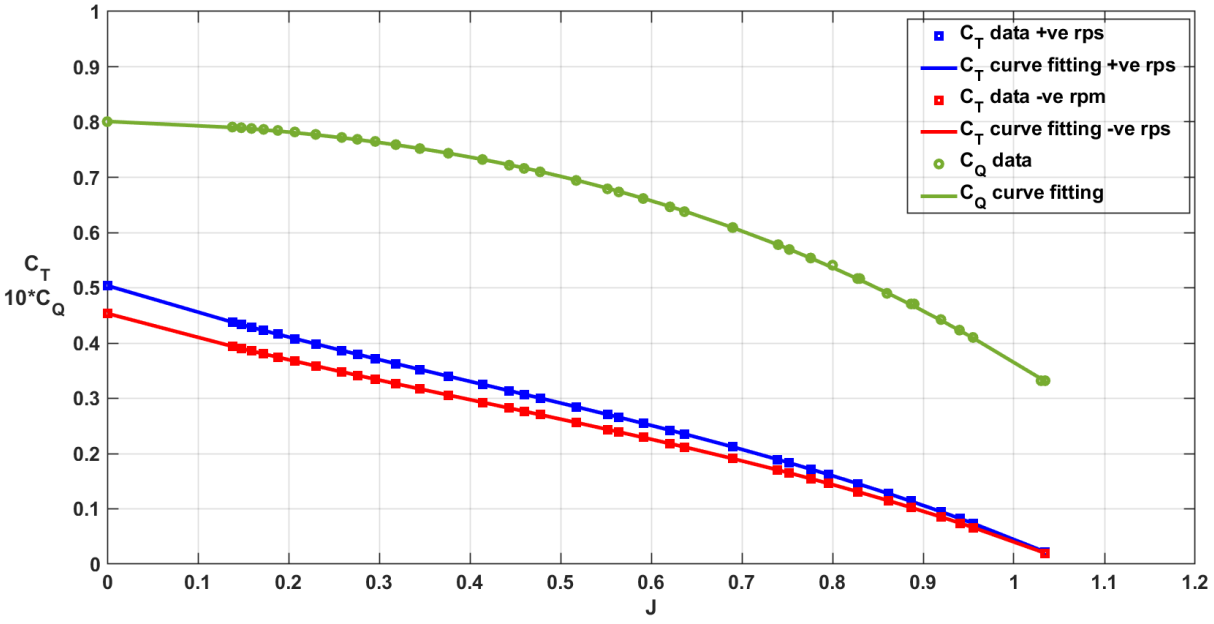

(b) *Manoeuvre thrusters.*

Figure 3.16: The C_T and $10 * C_Q$ curves as function of J fitted using experimentally refined data.

Consequently, the coefficients C_T and C_Q are transformed into K_T and K_Q, respectively, to better account for the limitations of using J alone and to reflect additional influencing factors. This transformation enables the development of a four-quadrant representation of the thruster model. The corrected coefficients K_T and K_Q are computed as follows:

$$K_T = \frac{C_T}{\frac{\pi}{8}J^2 + 0.49\pi^2} \tag{3.22}$$

$$K_Q = \frac{C_Q}{\frac{\pi}{8}J^2 + 0.49\pi^2} \tag{3.23}$$

It is important to note that the coefficients C_T and C_Q, when expressed as functions of the advance ratio J, are typically valid only in the first and third quadrants, corresponding to forward and reverse thrust conditions, respectively. To develop a comprehensive four-quadrant model, the coefficients for the second and fourth quadrants, which represent off-design conditions such as negative inflow or reverse rotation, are derived from theoretical models available in the literature [71, 40]. These theoretical values are then integrated with the previously calculated experimental K_T and K_Q data from the first and third quadrants to construct a complete four-quadrant model.

Finally, the overall refined K_T and K_Q as a function β in four quadrants are obtained by fitting the data with 20 terms of the Fourier series as shown in Figure.3.17 and mathematically given as follows:

$$K_T = \sum_{k=0}^{20} A_k \cos(\beta k) + B_k \sin(\beta k) \tag{3.24}$$

$$K_Q = \sum_{k=0}^{20} C_k \cos(\beta k) + D_k \sin(\beta k) \tag{3.25}$$

where A_k, B_k, C_k and D_k of propulsive and maneuvering thruster are described in Table 3.8 and Table 3.9 respectively. From (3.24) and (3.25), it is possible to estimate the thrust and torque produced by each thruster, which are summed to obtain total forces and moments (τ_p) generated by the thrusters using the following vectorial equations:

$$\tau_p = \begin{bmatrix} F \\ \\ M \end{bmatrix} = \begin{bmatrix} \sum_{i=1}^{6}(e_i \cdot T_i) \\ \\ \sum_{i=1}^{6}(l_i \times T_i) \cdot e_i + Q_i \end{bmatrix} \tag{3.26}$$

where F and M are the forces and moments vectors of size 3×1 expressed in body frame. The vector e_i represents the unit normal pointing to the direction of the thrust produced by the i_{th} motor (Table. 3.7). T_i and Q_i are the thrust and torque generated by the i_{th} motor and l_i is the position vector from the CG to i_{th} motor.

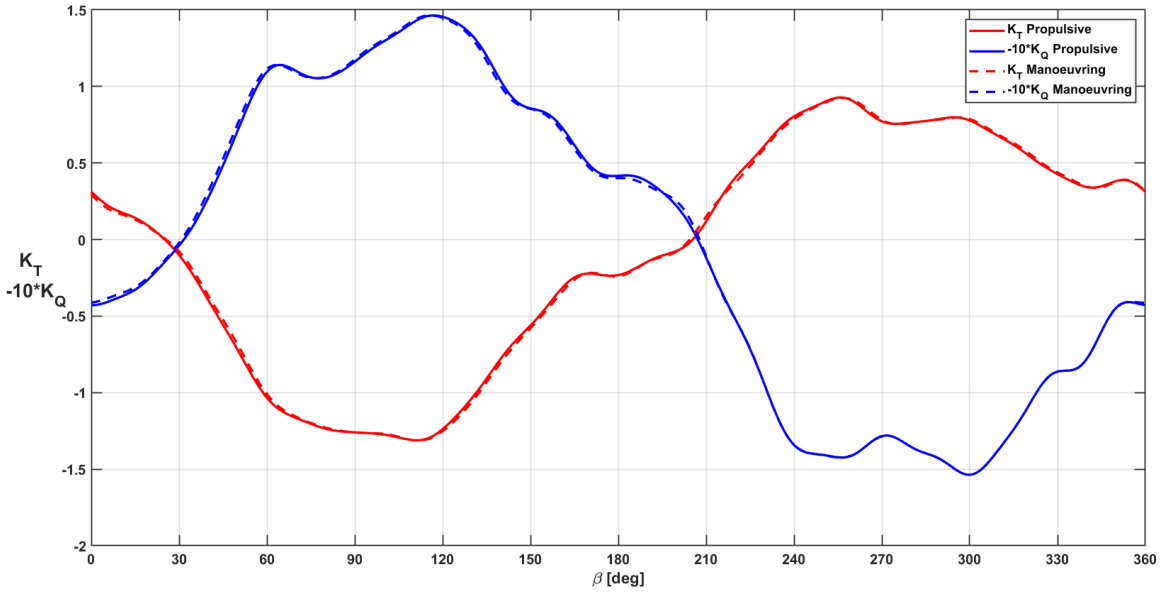

Figure 3.17: K_T and $-10 * K_Q$ four quadrant Operation for Propulsive and Manoeuvring propellers.

k	A_k (for K_T)	B_k (for K_T)	C_k (for K_Q)	D_k (for K_Q)
0	-0.09206028	-	0.00551495	-
1	0.20180687	-0.00388799	0.04281919	-0.00014652
2	0.13838084	-0.99595941	-0.00453555	-0.13203086
3	0.05676669	0.05504578	0.00464806	0.00603567
4	0.00055262	0.14252157	-0.00192653	0.01148237
5	-0.01324648	-0.02898227	-0.00308513	-0.00223488
6	-0.00118735	0.08885943	-0.00029858	0.01641088
7	0.01006116	-0.00866055	-0.00245483	0.00089074
8	0.00491892	-0.02414735	0.00009848	-0.00512016
9	-0.00241437	-0.01673651	-0.00096852	-0.00166618
10	0.00599285	0.00058718	0.00098547	0.00117258
11	0.01058598	-0.00271682	-0.00138868	0.00118160
12	-0.00893709	-0.00781591	-0.00011500	0.00342105
13	0.00445882	-0.00369873	0.00032087	0.00001993
14	-0.00204943	-0.00756685	0.00057607	0.00096086
15	0.00714124	-0.00256742	0.00153777	0.00022406
16	-0.00617022	-0.00508364	-0.00050650	0.00010467
17	0.00197036	-0.00044922	0.00095716	0.00021173
18	0.00056815	0.00013427	0.00069045	0.00038306
19	-0.00283608	-0.00337977	0.00001148	-0.00047074
20	-0.00004512	-0.00365705	0.00011479	-0.00066125

Table 3.8: Fourier Series Coefficients A_k, B_k, C_k, and D_k for K_T and K_Q of the Propulsive Thruster (M1, M2)

k	A_k (for K_T)	B_k (for K_T)	C_k (for K_Q)	D_k (for K_Q)
0	-0.09098766	-	0.00524171	-
1	0.20527927	-0.99457550	0.04161741	-0.13236558
2	0.13647601	0.06365627	-0.00435855	0.00481390
3	0.04889571	0.14018405	0.00469623	0.01161810
4	-0.00277528	-0.02706614	-0.00173967	-0.00285067
5	-0.01665875	0.08366338	-0.00282881	0.01656645
6	-0.00482159	-0.01161137	-0.00002515	0.00127992
7	0.01391855	-0.02529375	-0.00328790	-0.00495197
8	0.00317517	-0.01989391	0.00008865	-0.00192358
9	-0.00182741	0.00216645	-0.00136061	0.00083231
10	0.00672991	-0.00612963	0.00115739	0.00099105
11	0.00870930	-0.00543145	-0.00121626	0.00316571
12	-0.00655156	-0.00598118	-0.00026942	0.00034412
13	0.00214095	-0.00773791	0.00040556	0.00056637
14	-0.00044575	-0.00112208	0.00033937	0.00042057
15	0.00584554	-0.00664747	0.00175716	-0.00025495
16	-0.00776044	0.00108907	-0.00059986	0.00034795
17	0.00289544	-0.00183957	0.00105730	0.00036738
18	-0.00244427	-0.00316067	0.00060535	-0.00053796
19	-0.00060732	-0.00366892	-0.00002677	-0.00048631
20	-0.00250670	-0.00338672	0.00005741	-0.00060698

Table 3.9: Fourier Series Coefficients A_k, B_k, C_k, and D_k for K_T and K_Q of Maneuvering Thrusters (M3, M4, M5, M6)

3.3.2 Actuator modelling

To optimise the thruster's response, its dynamics are modelled. It has a Faulhaber 4490H036-24BS single-phase brushless DC motor paired with a Faulhaber 38A gearbox with a 4:1 ratio. The motor is controlled with a PI velocity controller. The mathematical model comprises two loops: the electric and the shaft dynamic loops. The electric loop outputs the torque of the motor and is given as follows:

$$\begin{aligned} L\dot{I} &= V - K_e n - RI \\ Q_m &= K_m I \end{aligned} \tag{3.27}$$

where L is the inductance, V is the voltage, K_e and R are the back EMF constant and thermal resistance, respectively. K_m is the torque constant, n is the shaft RPM, and I is current. Q_m represents motor torque.

The shaft dynamics are given as follows:

$$I_s \dot{n} = Q_{mp} - Q_p - Q_f(n) \tag{3.28}$$

here, $Q_{mp} = K_g Q_m$ denotes motor torque transferred to the propeller shaft, with K_g as the gear ratio. I_s is total inertial that accounts for the motor inertia (I_m) and propeller inertia (I_p), multiplied by the gear ratio (K_g) to account for gearbox inertia. Q_p is propeller torque, and Q_f represents torque due to motor friction:

$$Q_f(n) = C_0 \text{sign}(n) + C_v n \tag{3.29}$$

where C_0 and C_v are static and dynamic friction coefficients. The term $sign(\cdot)$ represents the sign function. The parameters of the motor are summarised in the Table. 3.10

Parameter	**Value**
R	0.66 $ohms$
L	$219 \cdot 10^{-6}$ H
K_m	$42{\cdot}10^{-3}$ Nm/A
K_e	$4.4{\cdot}10^{-3}$ V/min^{-1}
C_0	$3.86{\cdot}10^{-3}$ Nm
C_v	$5.2{\cdot}10^{-7}$ Nm/min^{-1}
K_g	4
I_m	$2.7375{\cdot}10^{-5}$ kgm^2
I_p	$2.3{\cdot}10^{-4}$ kgm^2

Table 3.10: Thruster actuator parameters.

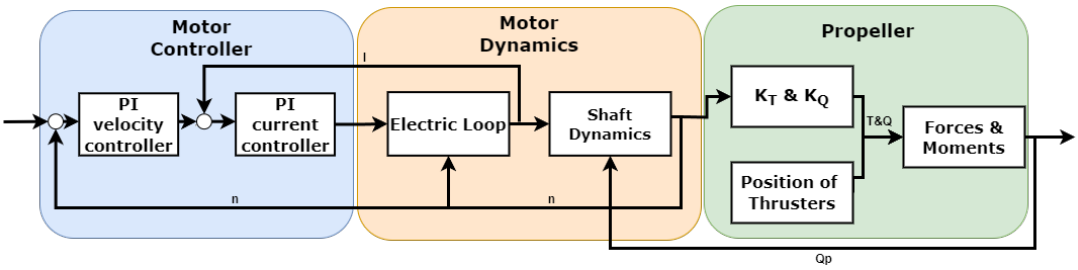

Figure 3.18: Simulation scheme of the thruster model.

The motor controller uses cascaded PI controllers, with the outer loop functioning as the velocity controller to determine the required current and the inner loop functioning as the current controller to output the required voltage.

All the estimated parameters are summarized in Table 3.11, providing a comprehensive reference for the identified model. This parameter set serves as the foundation for validating the mathematical model against real-world mission data, as discussed in the Section 3.4. The benchmark validation assesses the accuracy of the developed 6-degree-of-freedom simulator, ensuring its reliability as a testing framework for guidance and control algorithm development.

Blucy		**Actuator**	
Dry mass m	216.15 kg	Propeller type	Ka 4-70 with 19A Duct
Wet mass m	216.45 kg	Number of thrusters	6
I_x	11.3114 kgm^2	Number of blades	4
I_y	49.2791 kgm^2	Diameter D	0.145 m
I_z	41.7449 kgm^2	Pitch ratio P/D	1.28
I_{xy}	0 kgm^2	Area ratio A_e/A_o	0.7
I_{xz}	2.8636 kgm^2	Motor rpm range	$(-3000, 3000)rpm$
I_{yz}	0 kgm^2	Gear ratio	4 : 1
Center of Gravity CG	$(0, 0, 0)$ m	Prop rpm range	$(-750, 750)rpm$
Center of Buoyancy CB	$(0, 0, 0.048)$ m	**Propulsive**	M1, M2
Hydrodynamic Coefficients		K_t	A_k, B_k in Table 3.8
Linear $[Kg/s]$	**Quadratic** $[Kg/m]$	K_q	C_k, D_k in Table 3.8
$X_u = -2.61$	$X_{u\|u\|} = -61.82$	**Maneuver**	M3, M4, M5, M6
$Y_v = -24.72$	$Y_{v\|v\|} = -597.62$	K_t	A_k, B_k in Table 3.9
$K_v = 0.83$	$K_{v\|v\|} = -30.05$	K_q	C_k, D_k in Table 3.9
$N_v = -11.21$	$N_{v\|v\|} = -85.4$	**Position** w.r.t. CG	l_i $[m]$
$Z_w = -2.82$	$Z_{w\|w\|} = -255.86$	M1	[-0.821 0.230 -0.008]
$M_w = -1.71$	$M_{w\|w\|} = -38.7$	M2	[-0.821 -0.230 -0.008]
$Y_p = -1.43$	$Y_{p\|p\|} = -38.14$	M3	[0.615 0 -0.386]
$K_p = -0.04$	$K_{p\|p\|} = -23.68$	M4	[-0.835 0 -0.386]
$N_p = 0.41$	$N_{p\|p\|} = 9.28$	M5	[0.490 -0.113 -0.131]
$Z_q = -0.07$	$Z_{q\|q\|} = -37.19$	M6	[-0.660 0.124 -0.131]
$M_q = -0.06$	$M_{q\|q\|} = -95.69$	**Thrust versor**	e_i
$Y_r = -1.87$	$Y_{r\|r\|} = -342.98$	M1	[1 0 0]
$K_r = 0.14$	$K_{r\|r\|} = 41.28$	M2	[1 0 0]
$N_r = -0.044$	$N_{r\|r\|} = -375.53$	M3	[0 0 1]
Added Mass		M4	[0 0 1]
$X_{\dot{u}}$	-28.94 kg	M5	[0 1 0]
$Y_{\dot{v}}$	-166.03 kg	M6	[0 1 0]
$Z_{\dot{w}}$	-94.13 kg		
$K_{\dot{p}}$	-0.07 kgm^2		
$M_{\dot{q}}$	-17.10 kgm^2		
$N_{\dot{r}}$	-33.58 kgm^2		

Table 3.11: Summary table of Blucy UUV and actuator parameters.

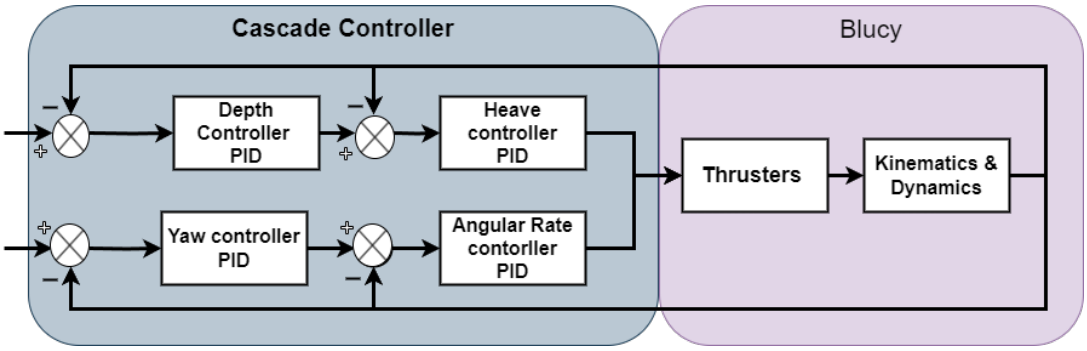

Figure 3.19: The cascade architecture of the depth and yaw controller.

3.4 Benchmark Validation

To validate the identified model and create a robust benchmark, real-world mission data are used to assess the performance of a comprehensive 6-degree-of-freedom (DOF) simulator developed in Matlab/Simulink. The benchmark incorporates the same PID cascade control architecture that is deployed on the Blucy during the actual missions. As depicted in Figure 3.19, the outer control loop governs depth (z) and yaw angle (ψ), generating reference velocities for the inner control loops. The inner loops then regulate the linear velocity (w) along the z-axis and the angular velocity (r) about the z-axis.

While the PID cascade structure in the benchmark mirrors the control system used in the real mission, its implementation here is solely for validation purposes. The broader objective of this benchmark is to serve as a foundation for the design and development of novel Guidance, Navigation, and Control (GNC) algorithms, as shown in Chapter 4. This enables a controlled environment for evaluating new strategies before deployment in actual missions.

3.4.1 Dataset

The simulator is validated against the data acquired during the previous mission of the Interreg IT-HR Techera project [72]. In particular, two datasets will be presented that are recorded during a multibeam survey in the Marine Protected Area of Miramare in Trieste, Italy. These datasets reflect typical maneuvers performed during a survey mission, such as diving, forward flight, and turning maneuvers, making them ideal for validation purposes.

3.4.1.1 Dataset 1: Depth and Yaw autopilot validation

The dataset 1, which is 620 s long, consist in different operation maneuvers as shown in Table 3.12. This dataset is used to validate the depth and yaw autopilots, which is

Time Interval (s)	Operation
0 - 120	Dive Maneuver @ 5 m
120 - 200	Forward Flight
200 - 260	Turn
260 - 440	Forward Flight
440 - 520	Turn
520 - 570	Forward Flight
570 - 620	Turn

Table 3.12: Operational Phases in Dataset 1

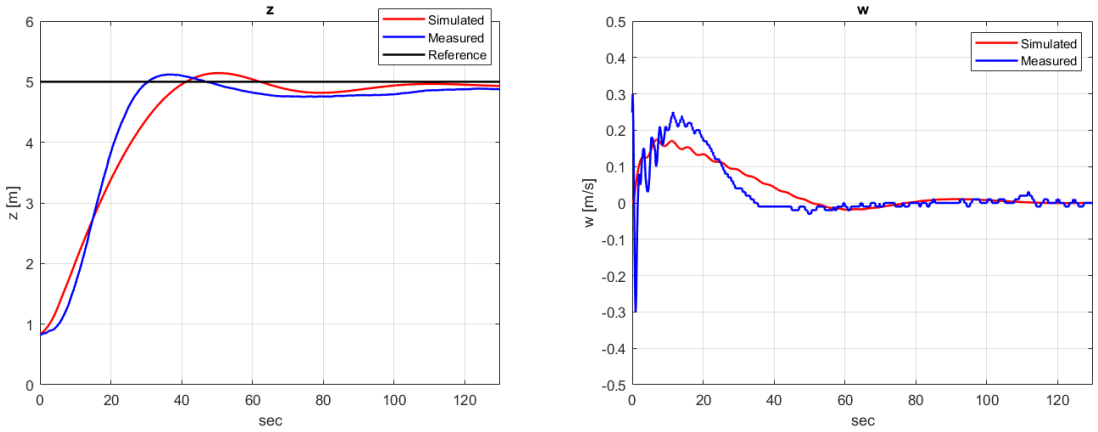

(a) *Depth z response.* (b) *velocity w response.*

Figure 3.20: Optimised depth autopilot response: Dataset 1.

crucial because the survey data includes these systems. The validation method involves passing the same reference signals used by the vehicle to the model and then comparing the model's response to the actual data from Blucy. These reference signals include force along the x-axis for surge velocity control, as well as depth and yaw references for the autopilots. The autopilot control parameters are optimised using a least squares algorithm. Specifically, the first 120 s od data are selected to validate the depth controller parameters, while 120 second from the first turn are used to validate the yaw autopilot. The optimised values are then utilised to simulate the complete data sets.

The responses of the optimised depth controller (z) and the linear velocity controller (w) during a dive manoeuvre are illustrated in Figures. 3.20a and 3.20b respectively. In the Figure. 3.20a, the simulated and measured depth z exibit a close match, demonstrating a strong correlation between the model and the real-life data. The initial transient response and the steady-state behaviour indicate that the model accurately captures the system's dynamics.

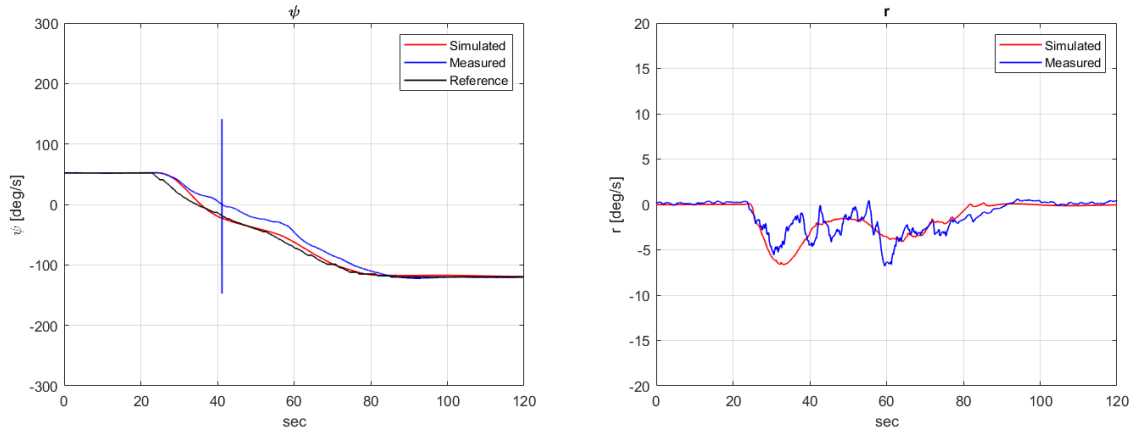

(a) *yaw ψ response.* (b) *angular velocity r response.*

Figure 3.21: Optimised yaw autopilot response: Dataset 1.

Gains	**Depth (z)**	**Velocity (w)**	**Yaw (ψ)**	**Angular velocity (r)**
Proportional	1.5	350	0.5	5000
Derivative	0	30	5	800
Integral	0	2	0	1000

Table 3.13: Optimised PID gains using the dataset 1.

In the Figure. 3.20b, the response of the simulated and measured linear velocity w also aligns well, though there are slight discrepancies in the transient phase. The measured data exhibits more variability compared to the simulated response, possibly due to noise in the system. Nonetheless, the steady-state velocity shows a good agreement, indicating that the model parameters are well-tuned.

Similarly, the responses of the yaw controller (ψ) and the angular velocity (r) are presented in Figures. 3.21a and 3.21b respectively. The simulated and measured responses demonstrate a reasonable correlation. However, there are notable differences in the transient phases that could be attributed to noise affecting the data. Despite these differences, the overall trend and steady-state behaviour of the simulated align well with the measured data. The identified parameters of the depth and yaw autopilots are shown in Table.3.13.

The complete simulation of dataset 1 is shown in Figure 3.22. The simulated trajectory closely matches the real data, except for the velocities u and v. One possible reason for this discrepancy is the tether, which introduces additional drag forces. Initially, with less tether in the water, the measured velocity aligns well with the simulation. However, as the vehicle turns and more tether is deployed, the measured surge velocity decreases despite the constant thrust, and sway velocity deviates due to increased tether tension,

Time Interval (s)	Operation
0 - 120	Forward Flight
120 - 220	Turn
220 - 350	Forward Flight
350 - 460	Turn
460 - 550	Forward Flight

Table 3.14: Operational Phases in Dataset 2

affecting the x and y positions. Another contributing factor is that the simulation does not account for hull-thruster interactions, which influence thrust production. While sea currents could be a potential source of discrepancy, to the best of the author's knowledge, the current was negligible during that survey, as the data were recorded on a calm day.

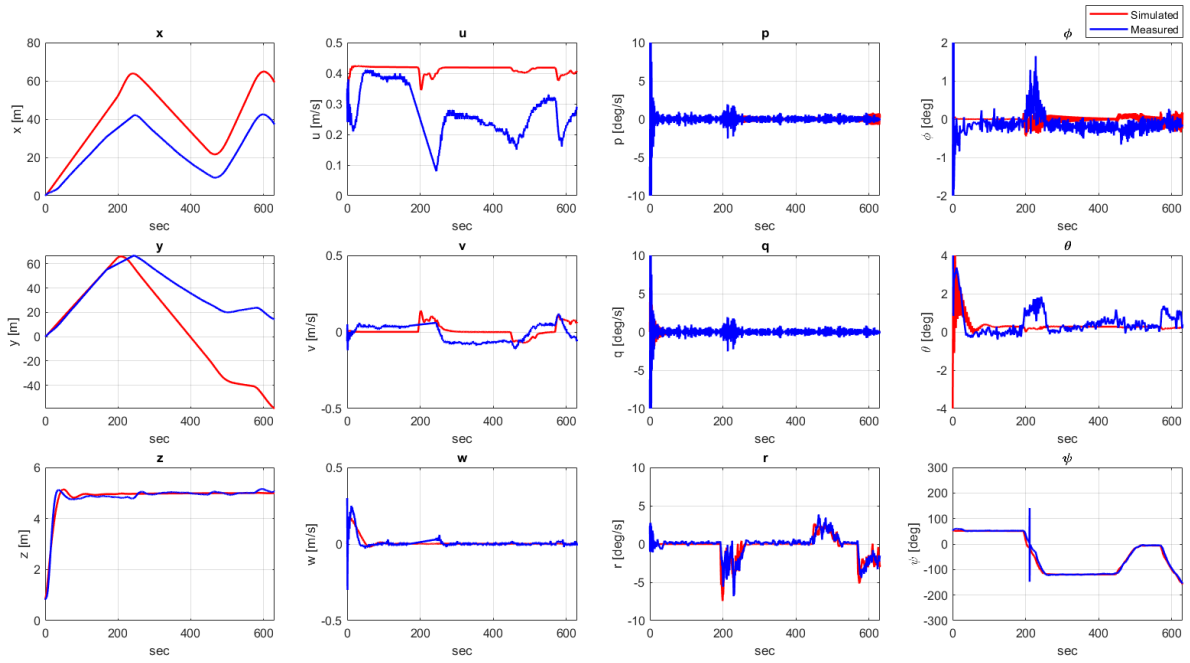

Figure 3.22: Validation of the states against the real data for dataset 1.

3.4.1.2 Dataset 2: Benchmark Validation

Spanning 550 seconds, Dataset 2 captures a survey conducted at a constant depth of 5 meters, with its various operational phases detailed in Table 3.14. Figure 3.23, demonstrates the validation of both the PID parameters and the benchmark model, using the same optimized PID values from Dataset 1.The alignment between the simulated results and the real data from Dataset 2 highlights the robustness of the proposed simulator.

It is important to note that data for linear velocities (u, v, w) and position (x, y) were not recorded during turns, as multibeam survey data collected during such maneuvers is often unreliable for 3D reconstruction and post-processing analysis. Despite this limitation, the comparison of position and ψ data validates the simulator, showing its effectiveness for designing and testing new guidance and control schemes.

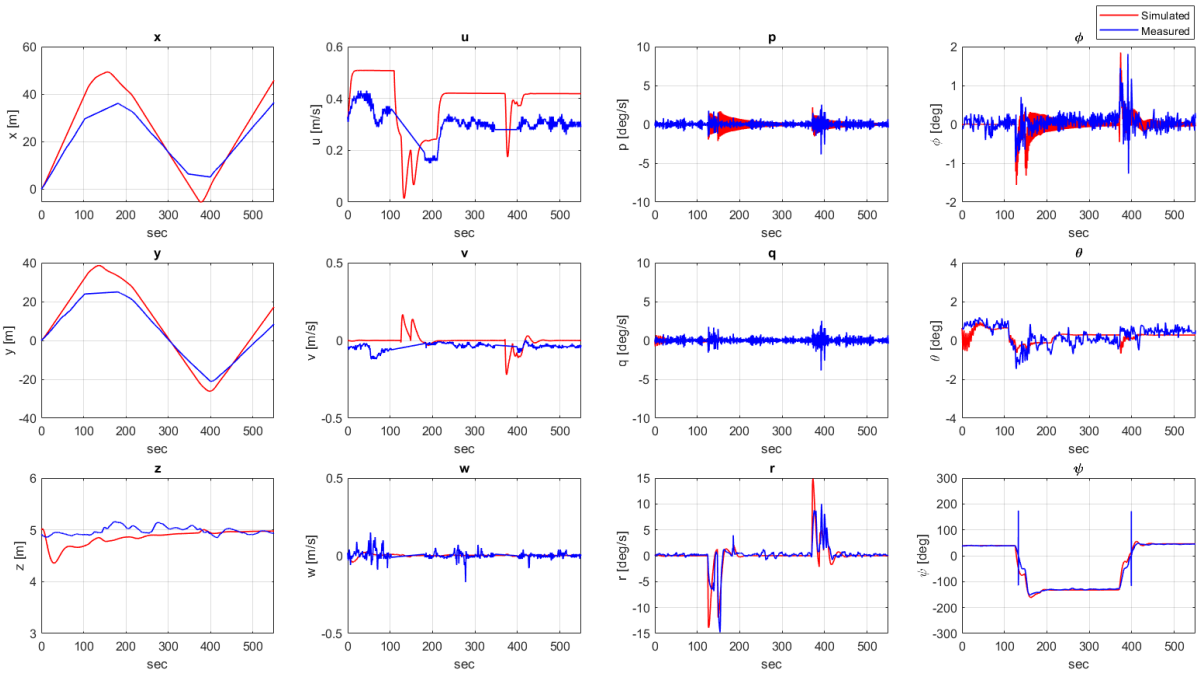

Figure 3.23: Validation of the states against the real data for dataset 2.

To summarize, this chapter presents a benchmark model for Blucy, developed using a balanced workflow between experimental and numerical simulation for parameter estimation (summarized in Table 3.11). Despite some limitations in the accuracy of the parameter estimations, such as stationary propeller assumption, simplifications in the vehicle's CAD model for CFD simulations, and the neglect of hull and thrusters interaction, the simulation results, validated against real mission data, demonstrated the model effectiveness. Consequently, the proposed benchmark model provides a reliable foundation for designing and testing new control algorithms, offering a robust baseline for control prototyping. This will enable the development of new algorithms for path-following, path generation, and trajectory tracking, enhancing Blucy's navigation capabilities in complex underwater environments as is illustrated in Chapter 4.

Chapter 4

Neuro Adaptive Fixed time Sliding mode control using Composite Learning

4.1 Control Objective

In this chapter, a robust guidance and control system for the Blucy UUV is developed to ensure precise trajectory tracking, where the vehicle's heading remains aligned with the direction of the trajectory, despite the presence of uncertainties and external disturbances. The proposed approach builds upon the work presented in [P4, P5], where adaptive fixed-time sliding mode and neuro-adaptive integral sliding mode control strategies, augmented with composite error learning, have been formulated for underactuated underwater vehicles.

The guidance and control system is designed in two parts. First, a look-ahead guidance law based on the Line-of-Sight (LOS) method is designed to enable accurate trajectory tracking. This approach calculates the desired heading by anticipating the path direction ahead of the vehicle, ensuring smooth and precise navigation. Secondly, a neuro-adaptive fixed-time sliding mode controller, enhanced by composite error learning, is designed to track the virtual inputs generated by the guidance system. The schematic representation of the overall system is depicted in Figure 4.1.

4.1.1 Preliminaries

To facilitate the forthcoming analysis, it is essential to be cognizant of certain foundational definitions and lemmas. In particular, they include essential results related to practical fixed-time stability and inequalities that facilitate the derivation of bounded

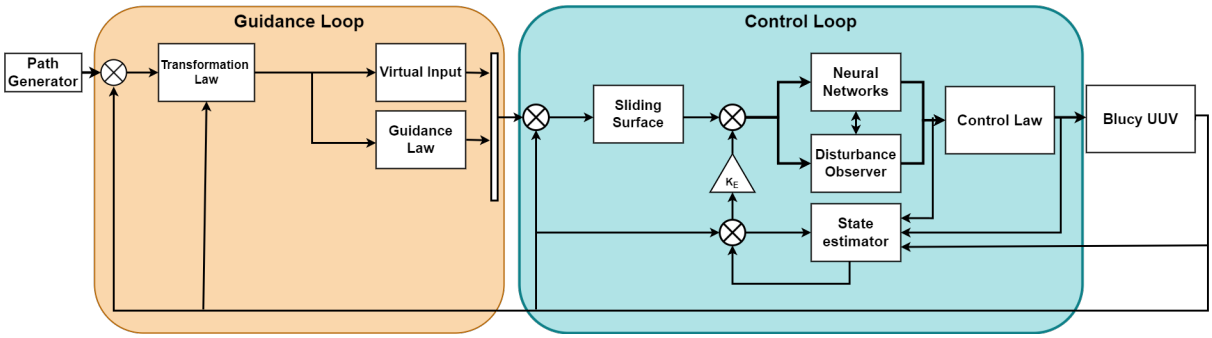

Figure 4.1: Guidance and control scheme.

convergence times. These concepts will be instrumental in proving the stability of the proposed neuro-adaptive fixed-time sliding mode control approach. Therefore, they are systematically introduced in the following:

Definition 4.1.1. *[73] Consider the following nonlinear system:*

$$\dot{x}(t) = f(x,t), \qquad x(0) = x_0 \tag{4.1}$$

where $x \in R^n$ is the system state variable and $f : R^+ \times R^n \to R^n$ is a nonlinear function. The system (4.1) is practical fixed time stable if for any initial condition $x(0) = x_0$, there exist constant $\eta > 0$ and settling time $T(\eta, x_0) < \infty$ satisfying $|x(t)| < \eta$, $\forall t > T$. Moreover, the settling time $T(\eta, x_0)$ is bounded, i.e., there exists $T(\eta, x_0) \leq T_{max}$, $\forall x(0) \in R^n$.

Lemma 4.1.1. *[74] For some constants $\alpha, \beta > 0$, $p > 1$, $0 < q < 1$ and $0 < \eta < \infty$, if there is a positive definite function such that*

$$\dot{V}(x) \leq -\alpha V^p(x) - \beta V^q(x) + \eta, \tag{4.2}$$

then the system (4.1) is practical fixed-time stable and the settling time T can be estimated by

$$T \leq T_{max} = \frac{1}{\alpha\phi(p-1)} + \frac{1}{\beta\phi(1-q)}, \tag{4.3}$$

with $0 < \phi < 1$ and the residual of the system (4.1) is give by

$$x \in \left\{ V(x) \leq min \left\{ (\frac{\eta}{(1-\phi)\alpha})^{\frac{1}{p}}, (\frac{\eta}{(1-\phi)\beta})^{\frac{1}{q}} \right\} \right\}. \tag{4.4}$$

Lemma 4.1.2. *[75] Considering the following scalar system:*

$$\dot{y} = -l_1 sign^{m_1} y - l_2 sign^{m_2} y, \quad y(0) = 0, \tag{4.5}$$

where $sign^{(\cdot)} y = |y|^{(\cdot)} \cdot sign(y)$, $l_1 > 0$, $l_2 > 0$, $m_1 > 1$ and $0 < m_2 < 1$. Then, the equilibrium is fixed-time stable with settling time T bounded by

$$T \leq T_{max} = \frac{1}{l_1(m_1 - 1)} + \frac{1}{l_2(1 - m_2)}, \tag{4.6}$$

Lemma 4.1.3. *[76] For $a, b \geq 0$ and $p, q \geq 1$ such that $\frac{1}{p} + \frac{1}{q} = 1$, the following inequality holds*

$$ab \leq \frac{a^p}{p} + \frac{b^q}{q}. \tag{4.7}$$

Lemma 4.1.4. *[77] For any real values of $x > 0$ and $p \in (1, 2)$, the following inequality holds*

$$\frac{x^p}{p} \geq x + \frac{1-p}{p} \tag{4.8}$$

Lemma 4.1.5. *[78] For $x \geq 0$ and $y, h > 0$, the following inequality holds*

$$x^h(y - x) \leq \frac{1}{1+h}(y^{h+1} - x^{h+1}). \tag{4.9}$$

Lemma 4.1.6. *[78] For $c > 1$, $a > 0$, $b \leq a$ and $b \in R$, it holds that*

$$(a - b)^c \geq b^c - a^c. \tag{4.10}$$

4.1.1.1 Neural Networks

An unknown continuous nonlinear function $f(x)$ can be estimated by employing the radial basis neural networks. Considering $x \in R^n$ and invoking universal approximation ability the nonlinear function can be approximated as follows [79]:

$$f(x) = W^{*T}\mu(x) + \epsilon, \tag{4.11}$$

where ϵ is the approximation error such that $|\epsilon| \leq \bar{\epsilon}$ and W^* are the optimal weights of neural network that satisfies $\|W^*\| = \bar{W}$.

$\mu(x)$ is the basis function vector $\mu = [\mu_1, \mu_2, ..., \mu_n]$ where n is the number of the neurons and μ_i is choosen as Gaussian function given as follows:

$$\mu_i(x) = exp^{\left(-\frac{(x-c_i)^T(x-c_i)}{\sigma_i^2}\right)}, \tag{4.12}$$

where c_i and σ_i are the centre and width of the Gaussian function respectively, and j is the number of neurons of the neural network.

4.2 Synthesis model: 4DOF

The model based on (2.31)-(2.32) is suitable for high fidelity simulations, but for the guidance and control system design, the use of a transformed set of equation is preferred. The model considered is the following 4 DOF synthesis model, describing the kinematics and the dynamics as follows:

$$\begin{aligned} \dot{x} &= u\cos\psi - v\sin\psi \\ \dot{y} &= u\sin\psi + v\cos\psi \\ \dot{z} &= w \\ \dot{\psi} &= r \end{aligned} . \tag{4.13}$$

and

$$\begin{aligned}
\dot{u} &= \tfrac{1}{m_{11}}\left(m_{22}vr - d_{11}u + \tau_u + d_u\right) \\
\dot{v} &= \tfrac{1}{m_{22}}\left(-m_{11}ur - d_{22}v + d_v\right) \\
\dot{w} &= \tfrac{1}{m_{33}}\left(-d_{33}w + \tau_w + d_w\right) \\
\dot{r} &= \tfrac{1}{m_{66}}\left(\left(m_{11} - m_{22}\right)uv - d_{66}r + \tau_r + d_r\right)
\end{aligned} \quad . \tag{4.14}$$

Here in, $m_{11} = m - X_{\dot{u}}$, $m_{22} = m - Y_{\dot{v}}$, $m_{33} = m - Z_{\dot{w}}$, $m_{66} = I_z - N_{\dot{r}}$, $d_{11} = X_u + X_{u|u|}|u|$, $d_{22} = Y_v + Y_{v|v|}|v|$, $d_{33} = Z_w + Z_{w|w|}|w|$, $d_{66} = N_r + N_{r|r|}|r|$. τ_u and τ_w are the forces along x_b and z_b respectively, while τ_r torque about z_b. The terms du, dv, dw, and dr represent the disturbance affecting the systems. It can be seen that the dynamic (4.14) is underactuated system since there is no actuation in the sway motion.

Remark 4.2.1. *This model does not account for roll and pitch dynamics, as the separation between the CG and the Center of Buoyancy (CB) generates a substantial restoring force that inherently stabilizes roll and pitch oscillations. Hence in real-time applications for slow-moving UUVs, the above dynamics are valid.*

Assumption 4.2.1. *The coupling between pitch and heave motions is assumed to be negligible.*

Remark 4.2.2. *According to Fossen [10], this assumption is valid for low-speed Underwater Unmanned Vehicles (UUVs) equipped with vertical thrusters, as these vehicles do not need to adjust their pitch to achieve vertical motion. This simplifies the control design by allowing independent control of heave without significant influence from pitch dynamics.*

Assumption 4.2.2. *The sway velocity is assumed to be passively bounded, such that $|v| < v_m$, where v_m is a positive constant.*

Remark 4.2.3. *This assumption is reasonable because the hydrodynamic damping forces acting in the sway direction are typically strong enough to limit sway velocities, even in the absence of active control. This passive stability is beneficial for maintaining lateral stability and minimizing energy consumption in corrective manoeuvres.*

Assumption 4.2.3. *Unknown time-varying disturbances are assumed to be bounded, such that $|d_n| \leq \bar{d}_n$, where $n = u, v, w, r$ and $\bar{d}_n$ is an unknown but finite constant.*

Remark 4.2.4. *External disturbances affecting UUVs, such as those from sea currents, underwater waves, or forces from tethers in Remotely Operated Vehicles (ROVs), are generally bounded in magnitude. This bounded nature allows for the design of robust control strategies that can effectively mitigate the impact of such disturbances, ensuring the stability and performance of the vehicle.*

Assumption 4.2.4. *The desired path x_d, y_d, and z_d are assumed to be differentiable.*

Remark 4.2.5. *The path considered in this study is smooth and continuous; hence, it is differentiable. This assumption ensures that the path-following control laws can be designed using differential calculus, which requires smooth and continuous trajectories.*

4.3 Look-ahead Distance based Line-of-Sight Guidance System

The desired path is typically described in a path reference frame. The tracking errors with respect to the inertial reference frame can be expressed in the path reference frame as follows:

$$\begin{aligned} x_e &= (x - x_d)\cos(\gamma_p) + (y - y_d)\sin(\gamma_p), \\ y_e &= -(x - x_d)\sin(\gamma_p) + (y - y_d)\cos(\gamma_p), \end{aligned} \tag{4.15}$$

where x_e and y_e are the along-track and cross-track errors, respectively, and γ_p is the path tangent angle defined as:

$$\gamma_p = \text{atan2}(\dot{y}_d, \dot{x}_d) \tag{4.16}$$

The control objective is to drive x_e and y_e to zero. To achieve this, we take the time derivative of (4.15) to obtain the error dynamics:

$$\begin{aligned} \dot{x}_e &= -(x - x_d)\sin(\gamma_p)\dot{\gamma}_p + (y - y_d)\cos(\gamma_p)\dot{\gamma}_p + (\dot{x} - \dot{x}_d)\cos(\gamma_p) + (\dot{y} - \dot{y}_d)\sin(\gamma_p), \\ \dot{y}_e &= -(x - x_d)\cos(\gamma_p)\dot{\gamma}_p - (y - y_d)\sin(\gamma_p)\dot{\gamma}_p - (\dot{x} - \dot{x}_d)\sin(\gamma_p) + (\dot{y} - \dot{y}_d)\cos(\gamma_p). \end{aligned} \tag{4.17}$$

It is important to address the terms involving $\dot{\gamma}_p$ in the error dynamics (4.17). These terms can be simplified based on the following considerations:

1. **Straight Line Path Approximation**: When vehicle is expected to follow a straight-line path, typically defined through waypoints, the rate of change of the path tangent angle, $\dot{\gamma}_p$, is approximately zero. This occurs because, for a straight-line path, the direction of the tangent remains constant, leading to $\dot{\gamma}_p \approx 0$. Thus, for straight-line segments, the effect of $\dot{\gamma}_p$ can be neglected.

2. **Low Curvature Approximation**: In situations where vehicles follows a curved path, but the curvature is gentle (i.e., large-radius arcs or gradual turns), the rate of change of γ_p remains small. In such cases, $\dot{\gamma}_p$ can be approximated using the radius of curvature R as follows:

$$\dot{\gamma}_p \approx \frac{1}{R}$$

where R represents the radius of curvature of the path. For large radii, $\dot{\gamma_p}$ becomes small, allowing to approximate its effect as negligible.

Therefore, for Blucy's operational scenarios, the terms involving $\dot{\gamma_p}$ can often be ignored without affecting the accuracy of the guidance and control system. This is especially true when Blucy is either following straight paths (where $\dot{\gamma_p} \approx 0$) or navigating curved paths with sufficiently large radii.

In the light of the above discussion (4.17) becomes:

$$\begin{aligned} \dot{x}_e &= (\dot{x} - \dot{x}_d)\cos(\gamma_p) + (\dot{y} - \dot{y}_d)\sin(\gamma_p) \\ \dot{y}_e &= -(\dot{x} - \dot{x}_d)\sin(\gamma_p) + (\dot{y} - \dot{y}_d)\cos(\gamma_p) \end{aligned} \tag{4.18}$$

Substituting kinematic relation (4.13) in (4.18) and rearranging, one has:

$$\begin{aligned} \dot{x}_e &= u\cos(\psi - \gamma_p) + v\sin(\psi - \gamma_p) - \dot{x}_d\cos(\gamma_p) - \dot{y}_d\sin(\gamma_p) \\ \dot{y}_e &= u\sin(\psi - \gamma_p) + v\cos(\psi - \gamma_p) + \dot{x}_d\sin(\gamma_p) - \dot{y}_d\cos(\gamma_p) \end{aligned} \tag{4.19}$$

By defining the desired horizontal velocity $U_d = \sqrt{\dot{x}_d^2 + \dot{y}_d^2}$ and from the definition of the path tangent angle γ_p (4.16), the components of the desired velocity in the x and y directions can be expressed as:

$$\begin{aligned} \dot{x_d} &= U_d\cos\gamma_p \\ \dot{y_d} &= U_d\sin\gamma_p \end{aligned} \tag{4.20}$$

Substituting (4.20) in (4.19):

$$\begin{aligned} \dot{x}_e &= u\cos(\psi - \gamma_p) + v\sin(\psi - \gamma_p) - U_d \\ \dot{y}_e &= u\sin(\psi - \gamma_p) + v\cos(\psi - \gamma_p) \end{aligned} \tag{4.21}$$

By defining horizontal velocity $U_h = \sqrt{u^2 + v^2}$, and arranging the remaining terms in amplitude-phase form, one has:

$$\begin{aligned} \dot{x}_e &= U_h\cos(\psi - \gamma_p + \beta) - U_d \\ \dot{y}_e &= U_h\sin(\psi - \gamma_p + \beta) \end{aligned} \tag{4.22}$$

where

$$\beta = atan2(v, u) \tag{4.23}$$

β is called as a sideslip angle. The sideslip angle arises due to external disturbances or non-zero sway velocity during a turn that causes the drift in the orientation of ψ of the surge velocity u relative to horizontal velocity U_h. Hence the relation between the β and U_h is given as $U_h = u/cos\beta$

Next, the following Lyapunov function candidate is defined:

$$V_1 = \frac{1}{2}x_e^2 + \frac{1}{2}y_e^2. \tag{4.24}$$

Taking the time derivative of V_1 along the system trajectory, one obtains:

$$\begin{aligned}\dot{V}_1 &= x_e\dot{x}_e + y_e\dot{y}_e \\ &= x_e\left(U_h\cos(\psi-\gamma_p+\beta)-U_d\right)+y_e\left(U_h\sin(\psi-\gamma_p+\beta)\right).\end{aligned} \tag{4.25}$$

Recalling that $u = U_h\cos(\beta)$, where u is the surge velocity, the aim is to design a virtual input u_d (desired surge velocity) to ensure that the position error x_e goes to zero. The virtual control input, u_d, is designed to guide the surge velocity u toward the desired velocity U_d. The virtual input u_d is designed as follows:

$$u_d = \frac{U_d cos\beta}{\cos(\psi-\gamma_p+\beta)}. \tag{4.26}$$

By substituting (4.26) into (4.25), it becomes:

$$\dot{V}_1 = y_e\left(U_h\sin(\psi-\gamma_p+\beta)\right). \tag{4.27}$$

The remaining task is to ensure the convergence of the cross-track error (y_e) to zero. In a fully actuated system, a virtual input for the lateral velocity v would be designed to make y_e converge to zero. However, since the system considered here is underactuated, a look-ahead-based guidance law as in [80] was employed:

$$\psi_d = \gamma_p - \beta + \arctan\left(\frac{-y_e}{\Lambda}\right), \tag{4.28}$$

where Λ is the look-ahead distance, typically considered to be constant. However, as presented in [81], a time-varying look-ahead distance as a function of the cross-tracking error y_e can be used to dynamically adjust the vehicle's behaviour based on its position relative to the desired path. The time-varying look-ahead distance is given by:

$$\Lambda(y_e) = (\Lambda_{max}-\Lambda_{min})e^{-k_\Lambda y_e^2}+\Lambda_{min}, \tag{4.29}$$

where Λ_{max} and Λ_{max} are the maximum and minimum look-ahead distances respectively, and k_Λ is a positive scaling factor. The underlying idea is intuitive and straightforward: a smaller Λ is assigned when the vehicle is far from the desired path, resulting in more aggressive steering to quickly reduce the cross-track error. Conversely, a larger Λ is assigned when the vehicle is close to the path to reduce the risk of overshooting, promoting smoother and more stable convergence. If the desired heading ψ_d is perfectly tracked, then (4.27) becomes:

$$\dot{V}_1 = -U_h\frac{y_e^2}{\sqrt{y_e^2+\Delta_{max}^2}}. \tag{4.30}$$

For $U_h > 0$, this implies that y_e converges to zero, indicating exponential stability as described in [81]. However, the stability is constrained by the Δ_{max}, that is as the Δ_{max} increases, the stability region becomes smaller. This fact should be taken into consideration when designing Δ_{max} and other related design parameters to ensure optimal performance and stability.

Remark 4.3.1. *Note that in the 4-DOF model, the vertical-track error z_e does not require a specific guidance law for convergence. Any controller capable of generating a non-zero vertical velocity w can stabilize the vertical-track error in this 4-DOF system.*

4.4 Neuro-Adaptive Fixed-Time Control Design and Stability Analysis

The tracking problem should be converted into a regulatory problem to design the fixed-time sliding mode controller. To do so, firstly, the equation (4.14) is written in vectorial form as follows:

$$\dot{X} = f(X) + g(X)\tau + \delta(X) + d(t) \tag{4.31}$$

where $X = [u, w, r]^T$, $\tau = [\tau_u, \tau_w, \tau_r]^T$, $\delta = \delta f(X) + \delta g(X)\tau$,

$$f(X) = \begin{bmatrix} \frac{1}{m_{11}}(m_{22}vr - d_{11}u) \\ \frac{1}{m_{22}}(-d_{33}w) \\ \frac{1}{m_{66}}((m_{11} - m_{22})uv - d_{66}r) \end{bmatrix}, \quad g(X) = \begin{bmatrix} \frac{1}{m_{11}} \\ \frac{1}{m_{33}} \\ \frac{1}{m_{66}} \end{bmatrix}, \quad d(t) = \begin{bmatrix} \frac{1}{m_{11}}d_u \\ \frac{1}{m_{66}}d_w \\ \frac{1}{m_{66}}d_r \end{bmatrix}.$$

Remark 4.4.1. *In the above model, The dynamics of the sway velocity are not considered as it cannot be controlled but only observed, and hence, its dynamics are not considered in the control design. Furthermore, δ represents the unknown uncertainties that the system can have due to ignored nonlinear dynamics in the synthetic model and the parameters.*

Define the velocity errors $u_e = u - u_d$, $w_e = w - w_d$, and $r_e = r - r_d$, where u_d, w_d, and r_d are desired velocities. Their error dynamics can be written as follows:

$$\dot{X}_e = f(X) + g(X)\tau + \delta(X) + d(t) - \dot{X}_d \tag{4.32}$$

where $X_e = [u_e, w_e, r_e]$ and $X_d = [u_d, w_d, r_d]$.

Next, the long tracking error x_e defined in (4.15) along with the vertical error $z_e = z - z_d$ and heading error $\psi_e = \psi - \psi_d$ are used to describe the position error dynamics given as follows:

$$\begin{aligned} \dot{x_e} &= U_h \cos(\psi - \gamma_p + \beta) - U_d = cos(\psi - \gamma_p + \beta)(u - u_d) = cos(\psi - \gamma_p + \beta)u_e \\ \dot{z_e} &= \dot{z} - \dot{z}_d = w - w_d = w_e \\ \dot{\psi_e} &= \dot{\psi} - \dot{\psi}_d = r - r_d = r_e \end{aligned} \tag{4.33}$$

In (4.33), the transformation of x_e is obtained using (4.26) and the relation $U_h = u/cos\beta$. The vectorial representation of (4.33) is given as follows:

$$\dot{e}_1 = R(\psi)X_e \tag{4.34}$$

where $e_1 = [x_e, z_e, \psi_e]^T$ and $R(\psi)$ is defined as $diag(\cos(\psi + \beta - \gamma_p), 1, 1)$. An auxiliary error is then introduced as:

$$e_2 = R(\psi)X_e \tag{4.35}$$

This results in a transformation that leads to the regulatory problem:

$$\begin{aligned} \dot{e}_1 &= e_2 \\ \dot{e}_2 &= F(X) + G(X)\tau + \Delta(X) + \bar{d}(t) - \dot{\bar{X}}_d \end{aligned} \tag{4.36}$$

where $F(X) = R(\psi)f(X)$, $G(X) = R(\psi)g(X)$, $\bar{d}(t) = R(\psi)d(t)$, $\dot{\bar{X}}_d = R(\psi)\dot{X}_d$, and $\Delta(X) = \dot{R}(\psi)X + R(\psi)(\delta f(X) + \delta g(X)\tau)$ represents the unmodeled dynamics and uncertainties. The estimation of Δ is achieved through a radial basis neural network, which leverages the universal approximation capability of neural networks:

$$\Delta = W^{*T}\mu(X) + \epsilon \tag{4.37}$$

where ϵ represents the approximation error that is bounded, $\mu(X)$ is the Gaussian function and W^* are the ideal neurons. Since W^* is known, let the $\hat{W}$ be its estimation. Consequently, the estimation of Δ is given as

$$\hat{\Delta} = \hat{W}^T\mu(X) \tag{4.38}$$

An adaptive disturbance observer is introduced to estimate to compensate for the neural network's estimation error and account for bounded time-dependent disturbances defined as $D = \bar{d}(t) + \epsilon$. Let $\hat{D}$ be the estimation of the D. Since both $\bar{d}(t)$ (Assumption 4.2.3) and ϵ are bounded the following inequality holds:

$$|D| \leq \chi_d \tag{4.39}$$

where χ_d is positive constant.

4.4.1 Fixed-Time Non-Singular Sliding Mode Control

A fixed-time, non-singular sliding surface, as given in [75], is defined as:

$$S = sign^{a_1}e_1 + \frac{k_2 a_2}{2a_2 - 1} sign^{2-1/a_2}(e_2 + k_1 sign^{a_1}e_1) \tag{4.40}$$

where $sign^{a_1}e_1 = |e_1|^{a_1} diag(sign(e_1))$, $sign^{2-1/a_2}(e_2 + k_1 sign^{a_1}e_1) = |e_2 + k_1 sign^{a_1}e_1|^{2-1/a_2}$ $diag(sign(e_2 + k_1 sign^{a_1}e_1))$ with $k_1 > 0$, $k_2 > 0$, $a_2 > 1$ and $1 < a_1 < 2 - 1/a_2$.

Subsequently, the singularity-free fixed-time control law is designed as:

$$\tau = -G(X)^{-1}\left(F(X) + \hat{D} + \hat{W}^T\mu(X) + k_1 a_1 diag(|e_1|^{a_1-1})\left(\frac{\Phi}{k_1} + e_2\right) + \alpha sign^{\gamma_1}S + \beta sign^{\gamma_2}S\right) \tag{4.41}$$

where $\alpha > 0$, $\beta > 0$, $\gamma_1 > 1$, and $0 < \gamma_2 < 1$ are the design parameters of the controller and Φ is the auxiliary function defined as follows:

$$\Phi(e_1, e_2) = \frac{1}{k_2} sign^{1/a_2}(e_2 + k_1 sign^{a_1}(e_1)) + \frac{k_1 a_2}{2a_2 - 1}(e_2 + k_1 sign^{a_1}(e_1)) \tag{4.42}$$

Combining equations (4.42) and (4.40), the following relationship is obtained:

$$k_2 \left|e_2 + k_1 sign^{a_1}(e_1)\right|^{1-1/a_2} \Phi = e_2 + k_1 S \tag{4.43}$$

4.4.2 State and Disturbance observer Design

State observers are typically designed to estimate system states that cannot be measured directly. In composite error learning framework they are also used to enhance the learning process by using the state observer estimation error along with the system's tracking error for updating the neural networks and disturbance observer. To this end, a fixed-time state observer is constructed as:

$$\dot{\hat{X}} = f(X) + g(X)u + \hat{W}^T\mu(X) + \hat{D} + k_0 e_o + \alpha_3 sign^{\gamma_1}(e_o) + \beta_3 sign^{\gamma_2}(e_o) \tag{4.44}$$

where k_o, α_3 and β_3 are the positive definite matrices that represent the state observer's gain. e_o is the prediction error made by the state observer, defined as:

$$e_o = X - \hat{X}. \tag{4.45}$$

Taking the time derivative of e_o, the observer error dynamics are obtained as:

$$\dot{e}_o = \tilde{W}\mu(X) + \tilde{D} - k_o e_o - \alpha_3 sign^{\gamma_1}(e_o) - \beta_3 sign^{\gamma_2}(e_o) \tag{4.46}$$

where $\tilde{W} = W^* - \hat{W}$ and $\tilde{D} = D_u - \hat{D}$ are estimation errors of the neural network's weights and the disturbance, respectively.

Now, the composite error learning-based updating law of the neural network is designed as:

$$\dot{\hat{W}} = \Gamma\Big((S\Theta + k_e e_o)\,\mu(X) - \alpha_1 \hat{W}^{\gamma_1} - \beta_1 \hat{W}^{\gamma_2}\Big) \tag{4.47}$$

where Γ, k_e, α_1 and β_1 are the positive definite matrices and

$$\begin{aligned} \Theta &= k_2 diag(|\sigma|^{1-1/a_2}) \\ \sigma &= e_2 + k_1 sign^{a_1}(e_1) \end{aligned} \tag{4.48}$$

Using the neural network approximation information and composite learning the nonlinear disturbance observer is designed as follows:

$$\hat{D} = X - \xi \tag{4.49a}$$

$$\dot{\xi} = f(X) + g(X)\tau + \hat{W}^T\mu(X) + \hat{D} - (S\Theta + k_e e_o) + \alpha_2\hat{D}^{\gamma_1} + \beta_2\hat{D}^{\gamma_2} \tag{4.49b}$$

where α_2 and β_2 are positive definite matrices.

The disturbance observer estimation error dynamics is given as follows:

$$\dot{\tilde{D}} = \dot{D} - (\tilde{W}\mu(X) + \tilde{D}) - (S\Theta + k_e e_o) + \alpha_2\hat{D}^{\gamma_1} + \beta_2\hat{D}^{\gamma_2} \tag{4.50}$$

4.4.3 Fixed time stability analysis

Theorem 4.4.1. *For the system described by equation (4.36) with the singularity-free sliding surface (4.40), the fixed-time control law (4.41), the state observer (4.44), it can be concluded that all signals of the closed-loop system are uniformly ultimately bounded. The switching function S converges to a small region around the surface $S = 0$ within a fixed time. $T_1 \leq T_r + T(\eta)$.*

Proof. Consider the following Lyapunov function candidate function

$$V = \frac{1}{2}S^TS + \frac{1}{2}\tilde{W}^T\Gamma^{-1}\tilde{W} + \frac{1}{2}\tilde{D}^T\tilde{D} + \frac{1}{2}e_o^Tk_e e_o \tag{4.51}$$

Where $\tilde{W} = W^* - \hat{W}$ and $\tilde{D} = D - \hat{D}$. Differentiating the above equation one gets:

$$\begin{aligned}
\dot{V} =& S^T\dot{S} + \tilde{W}^T\dot{\tilde{W}} + \tilde{D}^T\dot{\tilde{D}} + e_o^T\dot{e_o} \\
=& S^T\Big((a_1 diag(|e_1|^{a_1-1})e_2 + k_2 diag(|e_2 + k_1 sign^{a_1}e_1|^{1-1/a_2}) \\
& (\dot{e}_2 + k_1a_1 diag(|e_1|^{a_1-1})e_2)\Big) + \tilde{W}^T\Gamma^{-1}\dot{\tilde{W}} + \tilde{D}^T\dot{\tilde{D}} + e_o^Tk_e\dot{e_o} \\
=& S^T\Big((a_1 diag(|e_1|^{a_1-1})e_2 + k_2 diag(|e_2 + k_1 sign^{a_1}|^{1-1/a_2}) \\
& (F(x) + G(x)\tau + W^{*T}\mu(x) + D + k_1a_1 diag(|e_1|^{a_1-1})e_2)\Big) + \tilde{W}^T\Gamma^{-1}\dot{\tilde{W}} + \tilde{D}^T\dot{\tilde{D}} + e_o^Tk_e\dot{e}_o
\end{aligned} \tag{4.52}$$

substituting (4.41) in the above equation and simplifying:

$$\begin{aligned}
\dot{V} =& S^T\Big((a_1 diag(|e_1|^{a_1-1})e_2 + k_2 diag(|e_2 + k_1 sign^{a_1}|^{1-1/a_2})(a_1 diag(|e_1|^{a_1-1})\Phi \\
& + \tilde{D} + \tilde{W}^T\mu(x) - \alpha sign^{\gamma_1}S - \beta sign^{\gamma_2}S)\Big) + \tilde{W}^T\Gamma^{-1}\dot{\tilde{W}} + \tilde{D}^T\dot{\tilde{D}} + e_o^Tk_e\dot{e}_o
\end{aligned} \tag{4.53}$$

By using the relation (4.43) one has the following equation:

$$\begin{aligned}
\dot{V} =& S^T\Big(- (k_1 a_1 diag(|e_1|^{a_1-1})S + k_2 diag(|e_2 + k_1 sign^{a_1}|^{1-1/a_2})(\tilde{D} + \tilde{W}^T\mu(x) \\
& - \alpha sign^{\gamma_1} S - \beta sign^{\gamma_2} S)\Big) + \tilde{W}^T\Gamma^{-1}\dot{\tilde{W}} + \tilde{D}^T\dot{\tilde{D}} + e_o^T k_e \dot{e}_o \\
=& - k_1 a_1 diag(|e_1|^{a_1-1})S^T S + S^T\Big(k_2 diag(|e_2 + k_1 sign^{a_1}|^{1-1/a_2})(\tilde{D} + \tilde{W}^T\mu(x) \\
& - \alpha sign^{\gamma_1} S - \beta sign^{\gamma_2} S)\Big) + \tilde{W}^T\Gamma^{-1}\dot{\tilde{W}} + \tilde{D}^T\dot{\tilde{D}} + e_o^T k_e \dot{e}_o \\
\leq& S^T\Big(k_2 diag(|e_2 + k_1 sign^{a_1}|^{1-1/a_2})(\tilde{D} + \tilde{W}^T\mu(x) - \alpha sign^{\gamma_1} S - \beta sign^{\gamma_2} S)\Big) \\
& + \tilde{W}^T\Gamma^{-1}\dot{\tilde{W}} + \tilde{D}^T\dot{\tilde{D}} + e_o^T k_e \dot{e}_o \\
\leq& S^T\Theta\Big(\tilde{D} + \tilde{W}^T\mu(x) - \alpha sign^{\gamma_1} S - \beta sign^{\gamma_2} S\Big) + \tilde{W}^T\Gamma^{-1}(-\dot{\hat{W}}) + \tilde{D}^T\dot{\tilde{D}} + e_o^T k_e \dot{e}_o \\
\leq& S^T\Theta\tilde{D} + S^T\Theta\tilde{W}^T\mu(x) - \Theta\alpha|S|^{\gamma_1+1} - \Theta\beta|S|^{\gamma_2+1} - \tilde{W}^T\Big((S + e_o)\mu(x) \\
& - \alpha_1\hat{W}^{\gamma_1} - \beta_1\hat{W}^{\gamma_2}\Big) + \tilde{D}^T\Big(\dot{D} - (\tilde{W}\mu(X) + \tilde{D}) - (S\Theta + k_e e_o) + \alpha_2\hat{D}^{\gamma_1} + \beta_2\hat{D}^{\gamma_2}\Big) \\
& + e_o^T k_e\Big(\tilde{W}\mu(X) + \tilde{D} - k_o e_o - \alpha_3 sign^{\gamma_1}(e_o) - \beta_3 sign^{\gamma_2}(e_o)\Big) \\
\leq& - \Theta\alpha|S|^{\gamma_1+1} - \Theta\beta|S|^{\gamma_2+1} + \alpha_1\tilde{W}^T\hat{W}^{\gamma_1} + \beta_1\tilde{W}^T\hat{W}^{\gamma_2} + \tilde{D}^T\dot{D} - \tilde{D}^T\tilde{W}\mu(X) \\
& - \tilde{D}^T\tilde{D} + \alpha_2\tilde{D}^T\hat{D}^{\gamma_1} + \beta_2\tilde{D}^T\hat{D}^{\gamma_2} - k_e k_0 {e_o}^T e_o - \alpha_3|e_o|^{\gamma_1+1} - \beta_3|e_o|^{\gamma_2+1}
\end{aligned} \tag{4.54}$$

By using the Lemma 4.1.5 and 4.1.6 below inequalities holds

$$\begin{aligned}
\tilde{W}^T\hat{W}^{\gamma_1} \leq& \frac{1}{\gamma_1+1}\left(2W^{*\gamma_1+1} - \tilde{W}^{\gamma_1+1}\right) \\
\tilde{W}^T\hat{W}^{\gamma_2} \leq& \frac{1}{\gamma_2+1}\left(2W^{*\gamma_2+1} - \tilde{W}^{\gamma_2+1}\right) \\
\tilde{D}^T\hat{D}^{\gamma_1} \leq& \frac{1}{\gamma_1+1}\left(2D^{\gamma_1+1} - \tilde{D}^{\gamma_1+1}\right) \\
\tilde{D}^T\hat{D}^{\gamma_2} \leq& \frac{1}{\gamma_2+1}\left(2D^{\gamma_2+1} - \tilde{D}^{\gamma_2+1}\right)
\end{aligned} \tag{4.55}$$

Eq. (4.54) becomes :

$$\begin{aligned}
\dot{V} \leq& - \Theta\alpha|S|^{\gamma_1+1} - \Theta\beta|S|^{\gamma_2+1} + \frac{\alpha_1}{\gamma_1+1}(2W^{*\gamma_1+1} - \tilde{W}^{\gamma_1+1}) + \frac{\beta_1}{\gamma_2+1}(2W^{*\gamma_2+1} - \tilde{W}^{\gamma_2+1}) \\
& + \tilde{D}^T\dot{D} - \tilde{D}^T\tilde{W}\mu(X) - \tilde{D}^T\tilde{D} + \frac{\alpha_2}{\gamma_1+1}(2D^{\gamma_1+1} - \tilde{D}^{\gamma_1+1}) + \frac{\beta_2}{\gamma_2+1}(2D^{\gamma_2+1} - \tilde{D}^{\gamma_2+1}) \\
& - k_e k_0 {e_o}^T e_o - \alpha_3|e_o|^{\gamma_1+1} - \beta_3|e_o|^{\gamma_2+1}
\end{aligned} \tag{4.56}$$

from Lemma 4.1.3, the following inequalities hold:

$$\begin{aligned}
\tilde{D}^T\dot{D} \leq& \frac{1}{2}\tilde{D}^T\tilde{D} + \frac{1}{2}||\chi_d||^2 \\
\tilde{D}^T\tilde{W}\mu(X) \leq& \frac{\varepsilon}{2}\tilde{D}^T\tilde{D} + \frac{1}{2\varepsilon}||\mu(X)||^2\tilde{W}^T\tilde{W} \quad \text{with } \varepsilon > 0
\end{aligned} \tag{4.57}$$

$$\begin{aligned}\dot{V} \leq & -\Theta\alpha|S|^{\gamma_1+1} - \Theta\beta|S|^{\gamma_2+1} + \frac{\alpha_1}{\gamma_1+1}(2W^{*\gamma_1+1} - \tilde{W}^{\gamma_1+1}) + \frac{\beta_1}{\gamma_2+1}(2W^{*\gamma_2+1} - \tilde{W}^{\gamma_2+1}) \\ & - \frac{2-\varepsilon}{2}\tilde{D}^T\tilde{D} + \frac{1}{2}||\chi_d||^2 - \frac{||\mu(X)||^2}{\varepsilon}\tilde{W}^T\tilde{W} + \frac{\alpha_2}{\gamma_1+1}(2D^{\gamma_1+1} - \tilde{D}^{\gamma_1+1}) \\ & + \frac{\beta_2}{\gamma_2+1}(2D^{\gamma_2+1} - \tilde{D}^{\gamma_2+1}) - k_e k_0 {e_o}^T e_o - \alpha_3|e_o|^{\gamma_1+1} - \beta_3|e_o|^{\gamma_2+1} \\ \leq & -\Theta\alpha|S|^{\gamma_1+1} - \Theta\beta|S|^{\gamma_2+1} + \frac{\alpha_1}{\gamma_1+1}(2W^{*\gamma_1+1} - \tilde{W}^{\gamma_1+1}) + \frac{\beta_1}{\gamma_2+1}(2W^{*\gamma_2+1} - \tilde{W}^{\gamma_2+1}) \\ & + \frac{1}{2}||\chi_d||^2 + \frac{\alpha_2}{\gamma_1+1}(2D^{\gamma_1+1} - \tilde{D}^{\gamma_1+1}) + \frac{\beta_2}{\gamma_2+1}(2D^{\gamma_2+1} - \tilde{D}^{\gamma_2+1}) - \alpha_3|e_o|^{\gamma_1+1} - \beta_3|e_o|^{\gamma_2+1}\end{aligned} \tag{4.58}$$

Manipulating the following terms:

$$\begin{aligned}\frac{1}{\gamma_1+1}\tilde{W}^{\gamma_1+1} =& \frac{2^{\frac{\gamma_1+1}{2}}}{\gamma_1+1}\left(\frac{1}{2}\tilde{W}^T\tilde{W}\right)^{\frac{\gamma_1+1}{2}} \\ \frac{1}{\gamma_2+1}\tilde{W}^{\gamma_2+1} =& \frac{2^{\frac{\gamma_2+1}{2}}}{\gamma_2+1}\left(\frac{1}{2}\tilde{W}^T\tilde{W}\right)^{\frac{\gamma_2+1}{2}} \\ \frac{1}{\gamma_1+1}\tilde{D}^{\gamma_1+1} =& \frac{2^{\frac{\gamma_1+1}{2}}}{\gamma_1+1}\left(\frac{1}{2}\tilde{D}^T\tilde{D}\right)^{\frac{\gamma_1+1}{2}} \\ \frac{1}{\gamma_2+1}\tilde{D}^{\gamma_2+1} =& \frac{2^{\frac{\gamma_2+1}{2}}}{\gamma_2+1}\left(\frac{1}{2}\tilde{D}^T\tilde{D}\right)^{\frac{\gamma_2+1}{2}} \\ |S|^{\gamma_1+1} =& 2^{\frac{\gamma_1+1}{2}}\left(\frac{1}{2}S^TS\right)^{\frac{\gamma_1+1}{2}} \\ |S|^{\gamma_2+1} =& 2^{\frac{\gamma_2+1}{2}}\left(\frac{1}{2}S^TS\right)^{\frac{\gamma_2+1}{2}} \\ |e_o|^{\gamma_1+1} =& 2^{\frac{\gamma_1+1}{2}}\left(\frac{1}{2}e_o^Te_o\right)^{\frac{\gamma_1+1}{2}} \\ |e_o|^{\gamma_2+1} =& 2^{\frac{\gamma_2+1}{2}}\left(\frac{1}{2}e_o^Te_o\right)^{\frac{\gamma_2+1}{2}}\end{aligned} \tag{4.59}$$

$$\begin{aligned}\dot{V} \leq & -\left(\Theta\alpha 2^{\frac{\gamma_1+1}{2}}\left(\frac{1}{2}S^TS\right)^{\frac{\gamma_1+1}{2}} + \frac{\alpha_1 2^{\frac{\gamma_1+1}{2}}}{\gamma_1+1}\left(\frac{1}{2}\tilde{W}^T\tilde{W}\right)^{\frac{\gamma_1+1}{2}} + \frac{\alpha_2 2^{\frac{\gamma_1+1}{2}}}{\gamma_1+1}\left(\frac{1}{2}\tilde{D}^T\tilde{D}\right)^{\frac{\gamma_1+1}{2}}\right. \\ & \left.+\alpha_3 2^{\frac{\gamma_1+1}{2}}\left(\frac{1}{2}e_o^Te_o\right)^{\frac{\gamma_1+1}{2}}\right) - \left(\Theta\beta 2^{\frac{\gamma_2+1}{2}}\left(\frac{1}{2}S^TS\right)^{\frac{\gamma_2+1}{2}} + \frac{\beta_1 2^{\frac{\gamma_2+1}{2}}}{\gamma_2+1}\left(\frac{1}{2}\tilde{W}^T\tilde{W}\right)^{\frac{\gamma_2+1}{2}}\right. \\ & \left.+\frac{\beta_2 2^{\frac{\gamma_2+1}{2}}}{\gamma_2+1}\left(\frac{1}{2}\tilde{D}^T\tilde{D}\right)^{\frac{\gamma_2+1}{2}} + \beta_3 2^{\frac{\gamma_2+1}{2}}\left(\frac{1}{2}e_o^Te_o\right)^{\frac{\gamma_2+1}{2}}\right) + \left(\frac{2\alpha_1}{\gamma_1+1}W^{*\gamma_1+1}\right. \\ & \left.+\frac{2\beta_1}{\gamma_2+1}W^{*\gamma_2+1} + \frac{2\alpha_2}{\gamma_1+1}D^{\gamma_1+1} + \frac{2\beta_2}{\gamma_2+1}D^{\gamma_2+1} + \frac{1}{2}||\chi_d||^2\right)\end{aligned} \tag{4.60}$$

The (4.60) can be written in the form:

$$\dot{V}(x) \leq -\bar{\alpha}V^{\bar{\gamma_1}}(x) - \bar{\beta}V^{\bar{\gamma_2}}(x) + \eta \tag{4.61}$$

where:

$$\bar{\gamma_1} = \frac{\gamma_1 + 1}{2} \qquad \bar{\gamma_2} = \frac{\gamma_2 + 1}{2}$$

$$\bar{\alpha} = \min\Big\{\Theta\alpha 2^{\bar{\gamma_1}}, \frac{\alpha_1 2^{\bar{\gamma_1}}}{\gamma_1 + 1}, \frac{\alpha_2 2^{\bar{\gamma_1}}}{\gamma_1 + 1}, \alpha_3 2^{\bar{\gamma_1}}\Big\}$$

$$\bar{\beta} = \min\Big\{\Theta\beta 2^{\bar{\gamma_2}}, \frac{\beta_1 2^{\bar{\gamma_2}}}{\gamma_2 + 1}, \frac{\beta_2 2^{\bar{\gamma_2}}}{\gamma_2 + 1}, \beta_3 2^{\bar{\gamma_2}}\Big\}$$

$$\eta = \frac{2\alpha_1}{\gamma_1 + 1} W^{*\gamma_1 + 1} + \frac{2\beta_1}{\gamma_2 + 1} W^{*\gamma_2 + 1} + \frac{2\alpha_2}{\gamma_1 + 1} D^{\gamma_1 + 1} + \frac{2\beta_2}{\gamma_2 + 1} D^{\gamma_2 + 1} + \frac{1}{2}||\chi_d||^2$$

In terms $\bar{\alpha}$ and $\bar{\beta}$ all the terms are positive, except for the term that contains the Θ. This term, needs further analysis. Thus, for the convenience of the proof, the state space is divided into different spaces as:

$$\Omega = \begin{cases} \Omega_1 = \{\ (e_1, e_2) | \Theta \geq 1\} \\ \Omega_2 = \{\ (e_1, e_2) | \Theta < 1\} \end{cases} \tag{4.62}$$

When the system is in the area Ω_1, i.e., $\Theta > 1$ and $\sigma \neq 0$, the terms $\Theta\alpha 2^{\bar{\gamma_1}} > 0$ and $\Theta\beta 2^{\bar{\gamma_2}} > 0$. Hence according to the Lemma 4.1.1, the system will converge to $V = 0$ or to a small region Δ_1 around $V = 0$ in fixed time T_1:

$$\Delta_1 = \left\{ \lim_{t \to T_1} V \leq min \left\{ \left(\frac{\eta}{(1-\phi)\bar{\alpha}} \right)^{\frac{2}{\gamma_1 + 1}}, \left(\frac{\eta}{(1-\phi)\bar{\beta}} \right)^{\frac{2}{\gamma_2 + 1}} \right\} \right\} \tag{4.63}$$

$$T_1 \leq T_{max} = \frac{2}{\bar{\alpha}\phi(\gamma_1 - 1)} + \frac{2}{\bar{\beta}\phi(1 - \gamma_2)}, \tag{4.64}$$

This also means that sliding surface S will converge to 0 or it will converge in the neighborhood $S = 0$ or enter in the region Ω_2. If the system states enter the region Ω_2 , $0 < \Theta < 1$ and $\sigma \neq 0$ from (4.61), it can be demonstrated that $S = 0$ is still an attractor. What is remaining to prove is that $\sigma = 0$ is not an attractor expect for the origin. It is clear that on the curve $\sigma = 0$, the function $\Phi = 0$, thus the control input τ (4.41) becomes:

$$\tau = -G(X)^{-1}(F(X) + \hat{D} + \hat{W}^T\mu(X) + k_1 a_1 diag(|e_1|^{a_1 - 1}e_2) + \alpha sign^{\gamma_1}(S) + \beta sign^{\gamma_2}(S)) \tag{4.65}$$

Taking the time derivative of σ of (4.48), one obtains following equation:

$$\begin{aligned} \dot{\sigma} =& \dot{e_2} + k_1 a_1 diag(|e_1|^{a_1 - 1})e_2 \\ =& F(X) + G(X)\tau + W^{*T}\mu(X) + D + k_1 a_1 diag(|e_1|^{a_1 - 1})e_2 \end{aligned} \tag{4.66}$$

Substituting (4.65) in (4.66), one obtains:

$$\dot{\sigma} = \tilde{W}^T\mu(X) + \tilde{D} - \alpha sign^{\gamma_1} S - \beta sign^{\gamma_2} S \tag{4.67}$$

From (4.67), the terms $\tilde{W}^T\mu(X)$ and $\tilde{D}$ converge to region close to zero. Consequently, if $S > 0$ then $\dot{\sigma} < 0$, while if $S < 0$ one has $\dot{\sigma} > 0$. Thus the system states will transgress the regions Ω_2 into Ω_1 monotonically in finite time. Then for a given $t > 0$ there exist a constant $\lambda(t) > 0$ that represents the time required for the system to pass through the area Ω_2. Thus, $\sigma = 0$ is not an attractor except for the origin. Hence, the overall time required for V to converge to Δ_1 is: $T_r < T_1 + \lambda(t)$. □

Theorem 4.4.2. *The tracking error and velocity error converge to the equilibrium $e_1 = 0$ and $e_2 = 0$ or to the neighbourhood of the equilibrium within a fixed-time if $S = 0$ condition is satisfied or the S converge to a small region around $S = 0$ respectively.*

Proof. If the sliding surface $S = 0$ is satisified, Then the eqution 33 cna be written as follows:

$$\left(\frac{2a_2 - 1}{k_2 a_2} sign^{a_1} e_1\right)^{\frac{a_2}{2a_2-1}} + e_2 + k_1 sign^{a_1} e_1 = 0 \tag{4.68}$$

By defining the following equations:

$$\begin{aligned} \bar{k}_1 = \quad k_1 \qquad \bar{k}_2 \quad &= (\frac{2a_2 - 1}{k_2 a_2})^{\frac{a_2}{2a_2-1}} \\ \bar{a_1} = \quad a_1 \qquad \bar{a_1} \quad &= (\frac{a_1 a_2}{2a_2 - 1}) \end{aligned} \tag{4.69}$$

and noting that $\dot{e_1} = e_2$, one has the following equation:

$$\dot{e_1} = -\bar{k}_1 sign^{\bar{a}_1} e_1 - \bar{k}_2 sign^{\bar{a}_2} e_1 \tag{4.70}$$

By invoking the Lemma 4.1.2, the error will converge to the equilibrium with in the fixed time T_s:

$$T_s \leq \frac{1}{\bar{k}_1(\bar{a}_1 - 1)} + \frac{1}{\bar{k}_2(1 - \bar{a}_2)} \tag{4.71}$$

On the other hand if the S converges to the neighbourhood of $S = 0$, From theorem one analysis, one has :

$$\begin{aligned} S =& sign^{a_1} e_1 + \frac{k_2 a_2}{2a_2 - 1} sign^{2-1/a_2}(e_2 + k_1 sign^{a_1} e_1) \\ =& \epsilon, \quad |\epsilon| \leq \Delta_1 \end{aligned} \tag{4.72}$$

The maximum value of the ϵ is achieved when the $sign^{a_1} e_1$ and $\frac{k_2 a_2}{2a_2-1} sign^{2-1/a_2}(e_2 + k_1 sign^{a_1} e_1)$ have the same sign. The case of the positive sign is considered in this analysis From Lemma 4.1.4 the following inequality holds :

$$e_2 + k_1 sign^{a_1}(e_1) - \frac{a_2 + 1}{2a_2 - 1} \leq \frac{|e_2 + k_1 sign^{a_1}(e_1)|^{2-1/a_2}}{2 - 1/a_2} \tag{4.73}$$

Multiplying the by k_2 on both sides, the following equation is obtained

$$k_2 e_2 + k_1 k_2 sign^{a_1}(e_1) - \frac{k_2(a_2 + 1)}{2a_2 - 1} \leq \frac{k_2 a_2}{2a_2 - 1} |e_2 + k_1 sign^{a_1}(e_1)|^{2-1/a_2} \tag{4.74}$$

substituting the above equation into (4.72), it follows:

$$sign^{a_1}(e_1) + k_2 e_2 + k_1 k_2 sign^{a_1}(e_1) = \acute{\epsilon} + \frac{k_2(a_2+1)}{2a_2-1} \tag{4.75}$$

where $|\acute{\epsilon}| \leq |\epsilon| \leq \Delta_1$ the above equation can be written as follows:

$$e_2 + \left(\frac{1+k_1k_2}{k_2} - \frac{\frac{1}{k_2}\acute{\epsilon} + \frac{(a_2+1)}{2a_2+1}}{sign^{a_1}(e_1)} \right) sign^{a_1}(e_1) = 0 \tag{4.76}$$

Recalling that $\dot{e_1} = e_2$, the upper bound of e_1 can be analysed using the steady state analysis as follows:

$$\left(\frac{1+k_1k_2}{k_2} - \frac{\frac{1}{k_2}\acute{\epsilon} + \frac{(a_2+1)}{2a_2+1}}{sign^{a_1}(e_1)} \right) sign^{a_1}(e_1) = 0 \tag{4.77}$$

$$\left(\frac{1+k_1k_2}{k_2} \right) sign^{a_1}(e_1) = \frac{\acute{\epsilon}}{k_2} + \frac{a_2+1}{2a_2+1} \tag{4.78}$$

solving for $sign^{a_1}(e_1)$, one has:

$$sign^{a_1}(e_1) = \frac{\frac{\acute{\epsilon}}{k_2} + \frac{a_2+1}{2a_2+1}}{\frac{1+k_1k_2}{k_2}} \tag{4.79}$$

It follows:

$$|e_1|^{a_1} = \frac{|\acute{\epsilon}| + \frac{k_2(a_2+1)}{2a_2+1}}{1+k_1k_2} \tag{4.80}$$

taking the $\frac{1}{a_1}$ root on both sides one obtains the upper bound of the tracking error as follows:

$$|e_1| \leq \left(\frac{|\acute{\epsilon}| + \frac{k_2(a_2+1)}{2a_2+1}}{1+k_1k_2} \right)^{\frac{1}{a_1}} \tag{4.81}$$

The upper bound of the velocity error, e_2, can be obtained by substituting (4.81) in (4.76) and solving for e_2:

$$|e_2| \leq \left(2\frac{|\acute{\epsilon}| + \frac{k_2(a_2+1)}{2a_2+1}}{k_2} \right) \tag{4.82}$$

Consequently the overall settling time is given by:

$$T \leq T_r + T_s \quad \leq \frac{2}{\bar{\alpha}\phi(\gamma_1 - 1)} + \frac{2}{\bar{\beta}\phi(1-\gamma_2)} + \frac{1}{\bar{k}_1(\bar{a}_1 - 1)} + \frac{1}{\bar{k}_2(1-\bar{a}_2)} + \lambda(t) \tag{4.83}$$

This concludes the proof. □

4.5 Simulations

Remark 4.5.1. *In this thesis, the heading angle ψ is presented within the range $[-180^\circ\ 180^\circ]$. In the plots displaying the heading angle, abrupt changes may appear when the angle crosses the $\pm 180^\circ$ boundary, due to quadrant shifts. These changes are inherent to the angular representation and should be interpreted as wraparound effects rather than actual discontinuities in the system's heading.*

4.5.1 4 DOF Simulations

This section presents the results of trajectory tracking control, demonstrating the effectiveness of the overall control scheme through various simulations. In these tests, the 4-DOF model of Blucy is tasked with tracking a spatial circular trajectory over 200 seconds of simulation. This trajectory is defined in the inertial reference frame and consists of three distinct phases: descent, waiting, and 2D circular motion. The trajectory can be described as follows:

- **Phase 1: Descent** (0 s $\leq$ t $\leq$ 10 s) — The vehicle performs a vertical descent from the surface to a predefined depth of 5 meters.

- **Phase 2: Stationary Waiting** (10 s $<$ t $\leq$ 15 s) — Blucy maintains its position at the depth of 5 meters. During this phase, all control inputs are held steady.

- **Phase 3: 2D Circular Motion** (15 s $<$ t $\leq$ 200 s) — The vehicle follows a circular path at a constant depth of 5 meters. Given that Blucy is underactuated, based on the principle of the guidance system (Section 4.3), only the forward motion and yaw angle are actively controlled, with the vehicle's orientation aligned with the tangent of the circular path.

The desired trajectory in each phase is mathematically expressed as follows:

$$\begin{cases} \text{Phase 1: Descent, } 0s \leq t \leq 10s \\ x_d(t) = 20 \\ y_d(t) = 0 \\ z_d(t) = -\frac{5t}{10} \\ \psi_d(t) = \frac{\pi}{2} \end{cases} \tag{4.84}$$

$$\begin{cases} \text{Phase 2: Waiting, } 10s < t \leq 15s \\ x_d(t) = 20 \\ y_d(t) = 0 \\ z_d(t) = -5 \\ \psi_d(t) = \frac{\pi}{2} \end{cases} \tag{4.85}$$

$$\begin{cases} \text{Phase 3: 2D Circular Motion, } 15s < t \leq 200s \\ x_d(t) = R \cdot \cos\left(\frac{2\pi}{T}(t - t_2)\right) \\ y_d(t) = R \cdot \sin\left(\frac{2\pi}{T}(t - t_2)\right) \\ z_d(t) = -5 \\ \psi_d(t) = \tan^{-1}\left(\frac{\sin\left(\frac{2\pi}{T}(t-t_2)\right)}{\cos\left(\frac{2\pi}{T}(t-t_2)\right)}\right) \end{cases} \tag{4.86}$$

where $R = 20\ m$ is the radius of the circular path, $T = 160$ s is the time required to complete a circumference and $t_2 = 15\ s$ represent the time of the descent and waiting phase. During the simulations, the initial conditions for the 4-DOF model of Blucy are set as follows: $x(0) = 20$, $y(0) = z(0) = u(0) = v(0) = w(0) = r(0) = 0$, and $\psi(0) = \frac{\pi}{2}$. It should be noted that although the system is considered in 4 degrees of freedom (DOF), the figures that follow include plots for p, q, ϕ, and θ for the sake of completeness. Since these states are not considered in the 4-DOF system, their values remain zero throughout the entire simulations The guidance and controller parameters used, are shown in the Table 4.1.

Guidance	**Guidance Parameter**	
LOS - Look Ahead Distance	$\Lambda_{min} = 0.1$	$\Lambda_{max} = 1$
	$k_\Lambda = 0.2$	
Control Method	**Control Parameter**	
FTSMC	$k_1 = 1$	$k_2 = 0.0008$
	$a_1 = 1.005$	$a_2 = 1.08$
	$\alpha = \text{diag}\{0.001, 2, 1.5\}$	$\gamma_1 = 1.5$
	$\beta = \text{diag}\{1, 0.5, 0.7\}$	$\gamma_2 = 0.5$
	$k_0 = \text{diag}\{2, 4, 4\}$	
	$\alpha_3 = \text{diag}\{0.4, 0.4, 0.4\}$	$\beta_3 = \text{diag}\{1.2, 1.2, 1.2\}$
FTSMNNDO	$k_e = \text{diag}\{15, 15, 15\}$	
	$\alpha_2 = \text{diag}\{0.4, 0.4, 0.4\} \times 10^{-3}$	$\beta_2 = \text{diag}\{0.2, 0.2, 0.2\} \times 10^{-3}$
	$n = 20$	$C \in [0, 1]$
	$\sigma \in [1, 2]$	$\Gamma = \text{diag}\{15, 20, 25\}$
	$\alpha_1 = \text{diag}\{0.5, 0.5, 0.5\}$	$\beta_1 = \text{diag}\{1.5, 1.5, 1.5\}$

Table 4.1: Control Parameters used in the simulations for FTSMC and FTSMNNDO

In addition, to enhance the realism of the simulation and accurately reflect the limitations of Blucy's propulsive system (as detailed in Section 3.3), the control inputs for surge (τ_u), heave (τ_w), and yaw (τ_r) are subjected to saturation limits based on the vehicle's

physical capabilities:

$$\tau_i = sat(\tau_i) = \begin{cases} \tau_{i\,max}, \tau_i \geq \tau_{i\,max} \\ \tau_i, \tau_{i\,min} < \tau_i < \tau_{i\,max} \\ \tau_{i\,min}, \tau_i \leq \tau_{i\,min} \end{cases} \qquad (i = u, w, r) \tag{4.87}$$

Specifically, the control forces are capped at ±80 N in surge, ±70 N in heave, and the yaw moment is limited to ±40 Nm. Without loss of generality, the control input plots are presented in dimensionless percentages, scaled to ±100%, to facilitate comparison with the system's maximum capabilities.

Simulations considers different working conditions to proof the effectiveness of the designed control scheme: (a) Test 1 will demonstrate the effectiveness of the trajectory tracking control and discuss the fixed time stability as well as the chattering mitigation; (b) Test 2 introduces external disturbances as defined in Assumption 4.2.3 and evaluates the performance of the control scheme. A comparison is made between the Fixed Time Sliding Mode Controller (FTSMC) and the proposed Fixed Time Sliding Mode Neural Network Disturbance Observer (FTSMNNDO) in terms of Integrated Absolute Error (IAE), Integrated Square Error (ISE), and Integrated Time Absolute Error (ITAE). (c) Test 3 compares FTSMNNDO and FTSMC in presence of external disturbances, model uncertainties and simultaneous actuator faults, demonstrating the super performances in handling difficult operational scenario due to the estimation of Neural Networks and Disturbance observer.

4.5.1.1 Test 1: Undisturbed System

This test demonstrates the effectiveness of the proposed control scheme in the absence of uncertainties and external disturbances. The figures associated with this scenario are presented in Figures 4.2 -4.7.

The Figure 4.2 represents the state variable, demonstrating the effectiveness of the proposed control system in the stabilization of all variables. In particular, the figures show that after an initial transient response in certain controlled variables (such as u, w, and r), the system quickly damps oscillations and brings the system to a stable state. The flat lines in several angular plots (p, q, ϕ, θ) are justified because 4 DOF system is considered.

Moving on the Figure 4.3, a comparison is made between the simulated trajectory (blue line) and the desired trajectory (red dashed line). The trajectory tracking appears highly accurate, suggesting that the control system is performing well, especially after the initial settling period in altitude as can be seen in Figure 4.4. The largest error appears in z_e due to the different initial condition $z(0)$ compared to the desired z_d. However, once

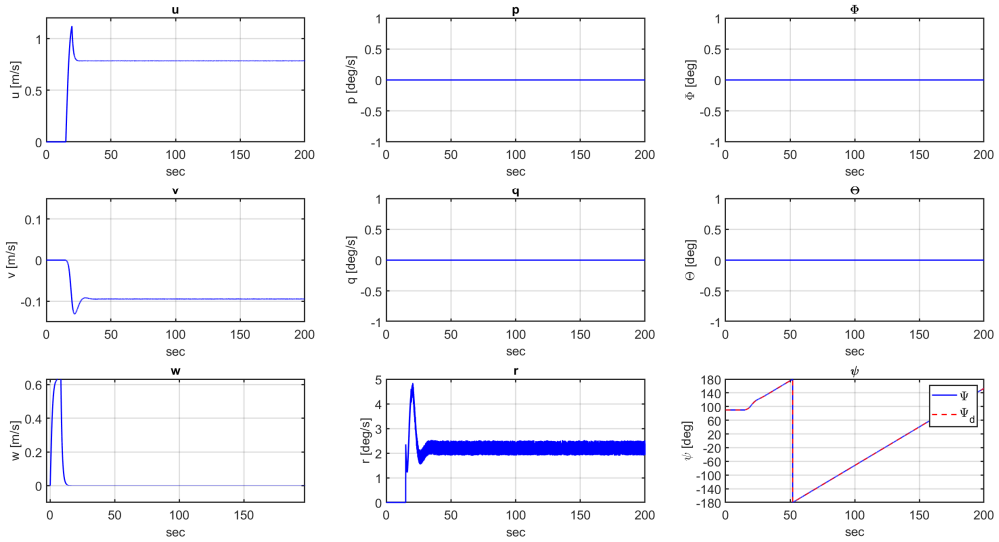

Figure 4.2: State Variables Test 1

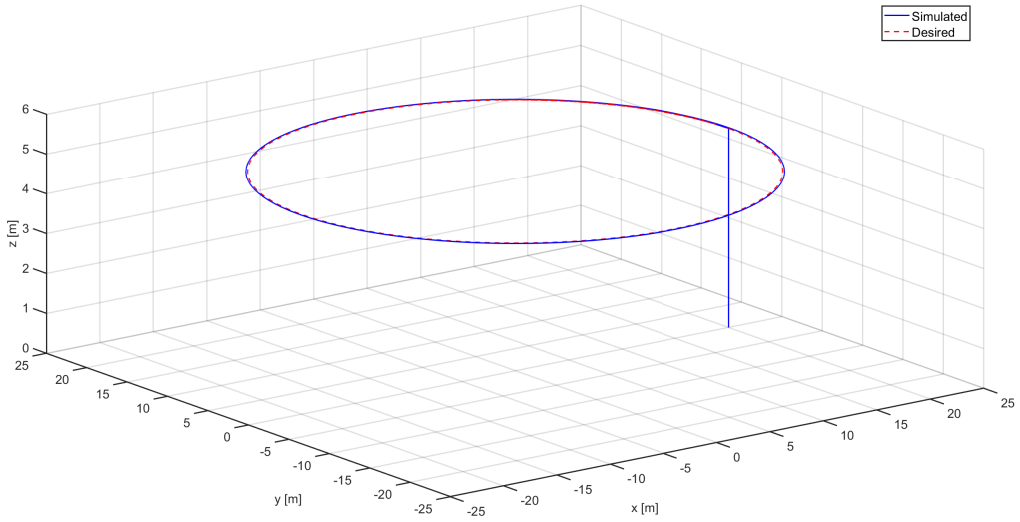

Figure 4.3: Trajectory Test 1

the desired z_e is reached, the error reduces to 0. The maximum error in the x and y direction is approximately bounded at $10^{-1}m$, while the maximum error magnitude ψ_e remains within $10^{-2}deg$.

Figure 4.5 represents the sliding variables, the control system successfully drives the sliding variable in the neighbourhood of zero within a fixed-time window regardless of the initial conditions or system states. This fixed-time convergence can particularly be studied in the S_w plot. Given that the desired z trajectory is treated as a step input, the sharp transition in the sliding surface at the start of the response is clearly visible. By

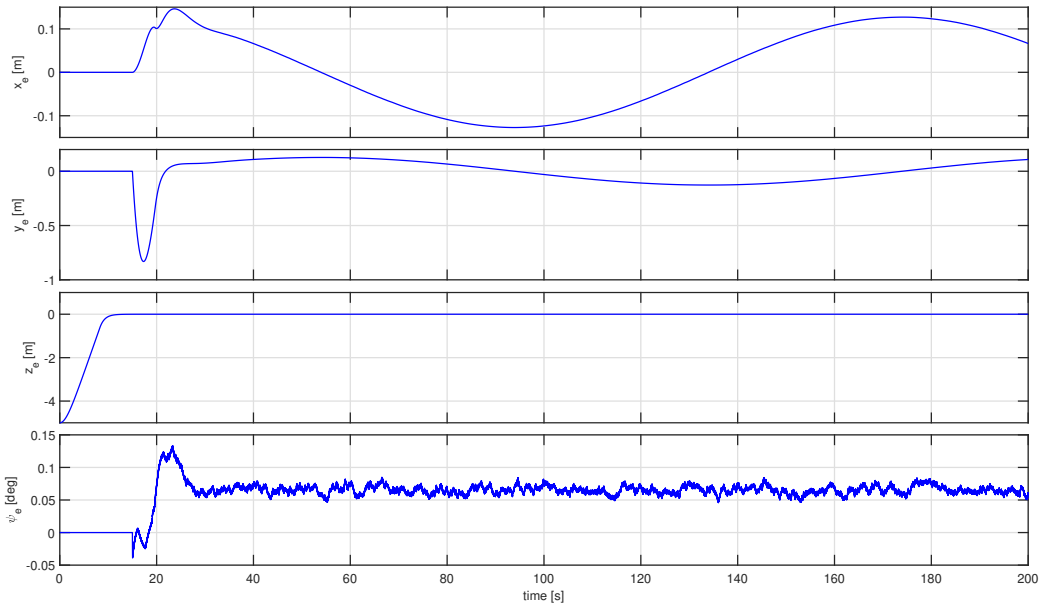

Figure 4.4: Position and Attitude Tracking Error: Test 1

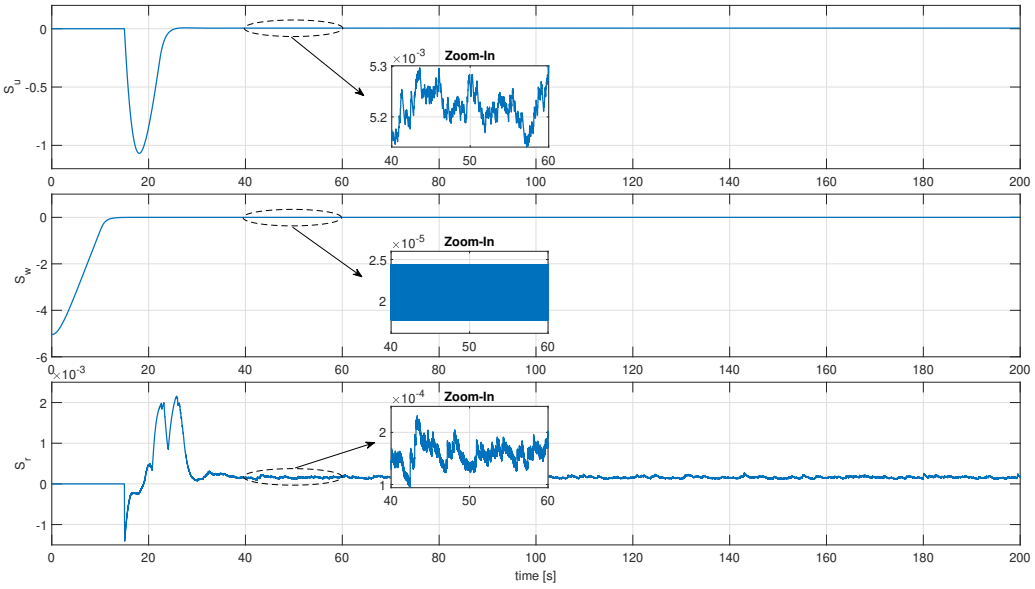

Figure 4.5: Sliding Surfaces Test 1

using the (4.64) and control parameters (Table 4.1), $T_{max} = 20.38$ s and from the figure it is the clear the reach time is less than the T_{max}, as predicted.

Figure 4.6 illustrates the performance of a state estimator and its corresponding error dynamics. The left side shows the estimated states $(\hat{u}, \hat{w}, \hat{r})$ compared to the true states, while the right side shows the estimation errors (e_{ou}, e_{ow}, e_{or}). During the transient phase an overshoot can be observed, this due to the fact that the state observer takes estimations of the neural network and disturbance observer into account (4.44). These elements

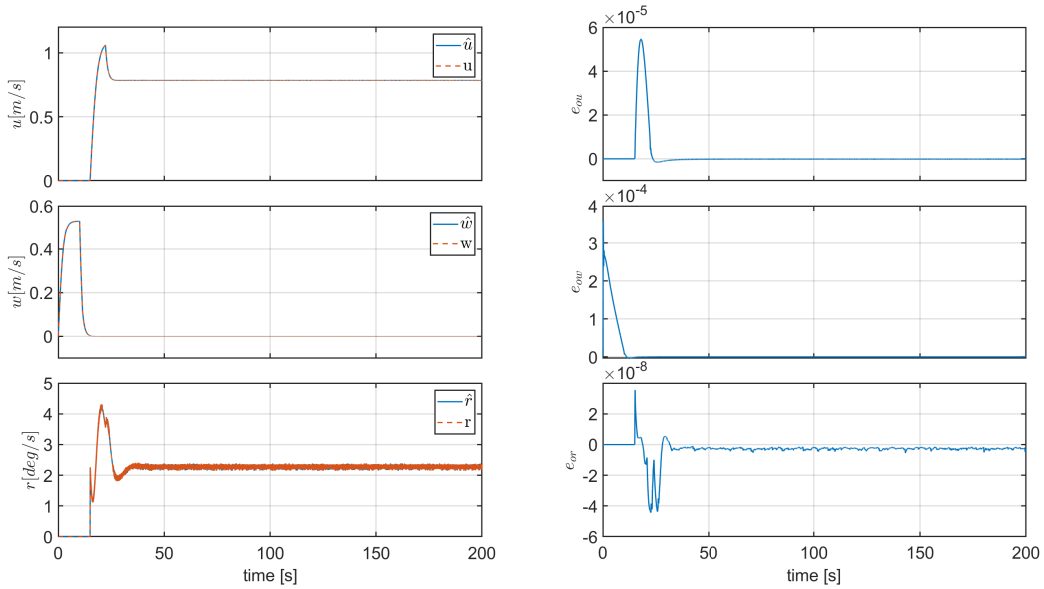

Figure 4.6: State Observer Estimations and Corresponding Estimation Errors: Test 1

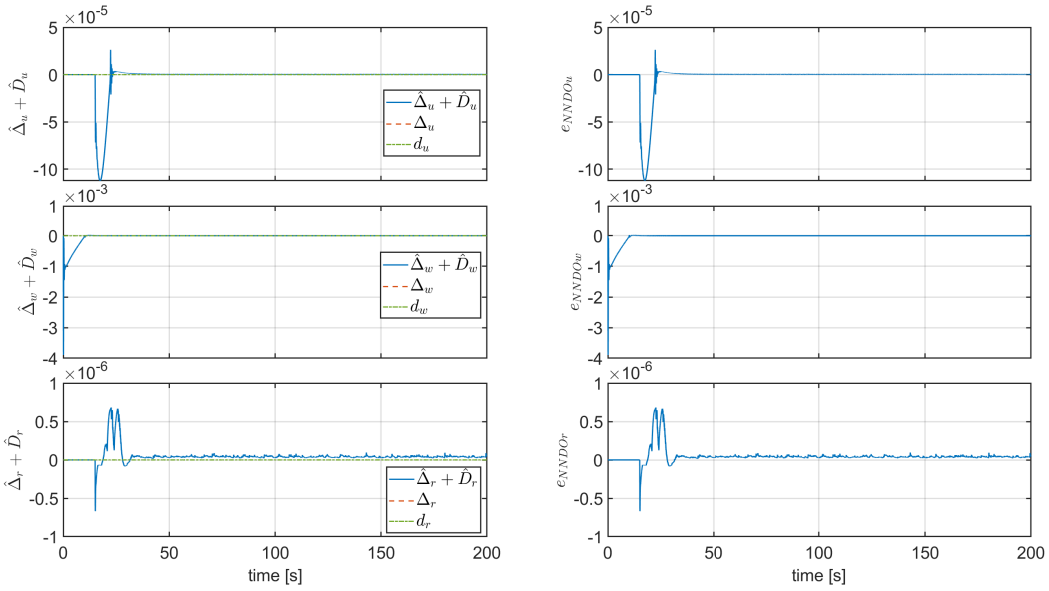

Figure 4.7: Neural Network and Disturbance Observer Estimations ($\hat{\Delta} + \hat{D}$) of Uncertainties and Disturbances

require a brief training period to accurately estimate the uncertainties and disturbances within the system. As a result, the initial discrepancy between the estimated values and the actual values leads to a temporary overshoot, as shown in Figure 4.7, which presents the sum estimations of the NN and DO, expressed as $\hat{\Delta} + \hat{D}$. It has to be noticed that DO incorporate estimation derived from NN (4.49), while the prediction errors capture discrepancies in disturbance estimation. There is a continuous exchange of information

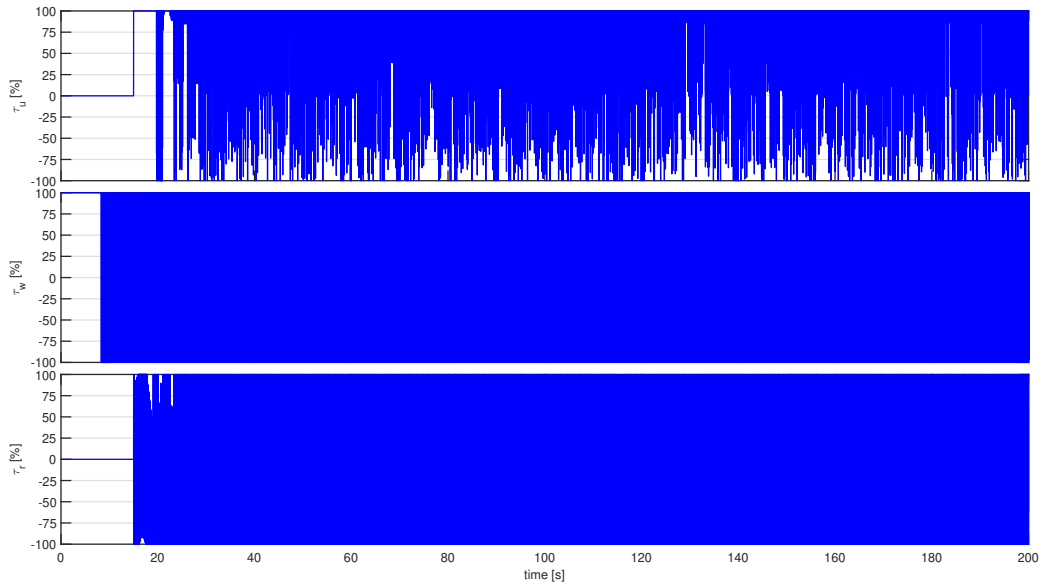

Figure 4.8: Control inputs of Test 1: τ_u, τ_w and τ_r

between the DO and NN, indicating that they collaboratively share the task of estimation, hence the summation of the estimations is presented in the figure. Once the NN and DO sufficiently train and converge to accurate estimates, the overshoot diminishes, and the system stabilizes since the disturbance and uncertainties are not considered in this scenario.

Figure 4.8 represents the control action of the control law. The control signal oscillates between the boundaries of the control authority (represented in percentage: $\pm 100\%$). The high-frequency oscillations observed in the figure are a classic indication of chattering in sliding mode control [82]. This is also reflected in the sliding variables and states in Figures 4.5 and 4.2. Chattering occurs due to the discontinuous nature of the *sign* function in the control law and the sliding variable, which switches the control input at high frequencies to maintain the system on the sliding surface. This leads to problems like excessive wear on actuators, energy inefficiency, heat generation, and induced vibrations.

To mitigate chattering, various methods such as boundary layer approximation (soft switching)[83], higher-order sliding modes [84], or adaptive control [85] can be employed . These techniques are effective in reducing the high-frequency oscillations associated with sliding mode control while preserving its inherent robustness. In this work, a boundary layer approximation is adopted [83], where the discontinuous $sign(x)$ function is replaced with the smooth $\tanh\left(\frac{x}{\epsilon}\right)$ function. As the value of ϵ approaches zero, the hyperbolic tangent function behaves increasingly like the *sign* function, allowing for a balance between chattering reduction and control precision.

The simulation results after replacing the *sign* function with $\tanh\left(\frac{x}{\epsilon}\right)$, using $\epsilon = 0.0001$, are shown in Figures 4.9 and 4.10. Compared to the previous results in Figures

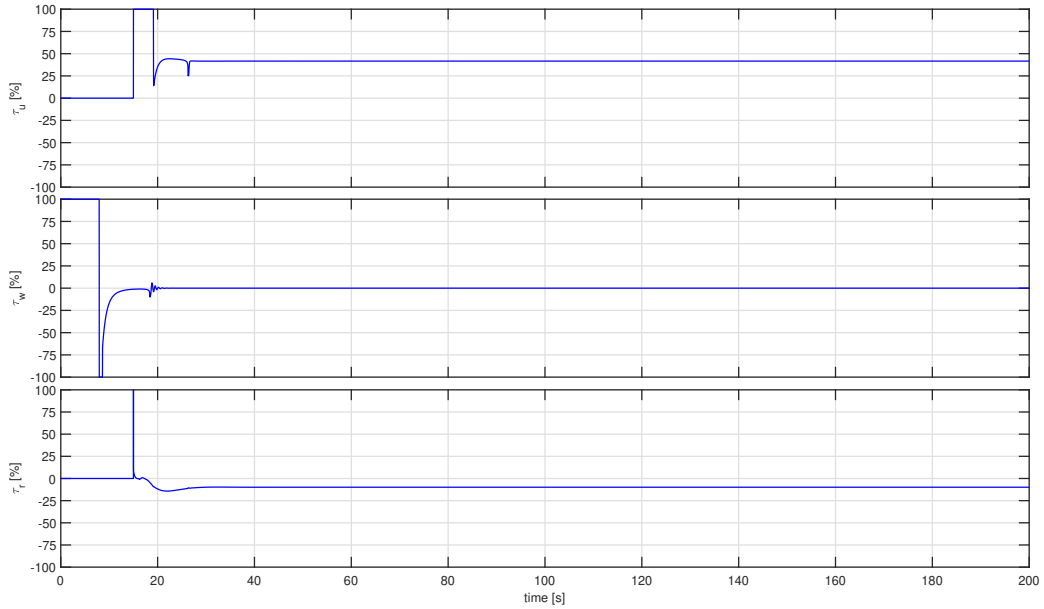

Figure 4.9: Control inputs without chattering: τ_u, τ_w and τ_r

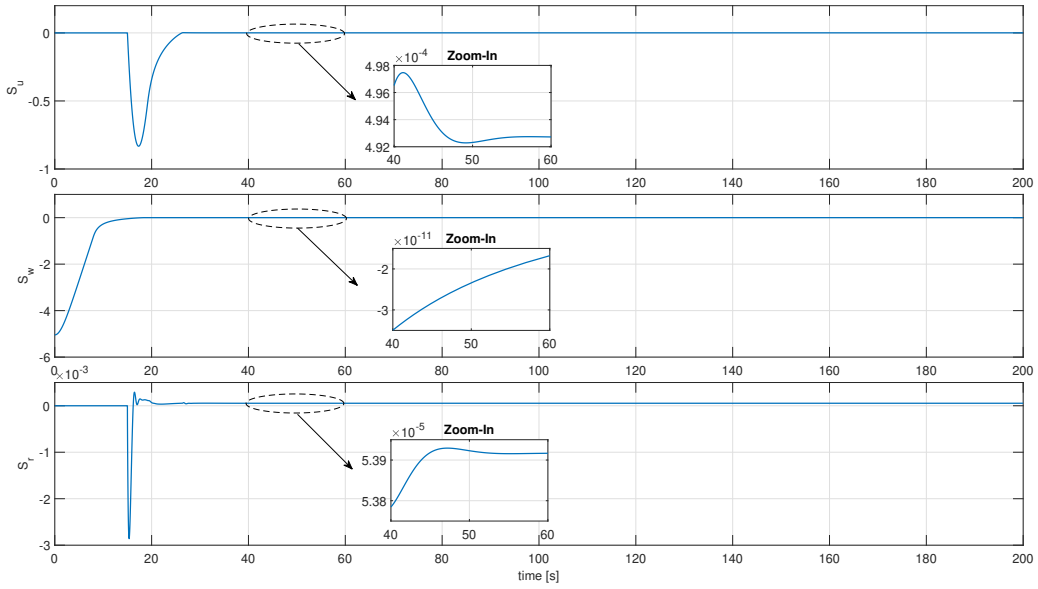

Figure 4.10: Sliding Surfaces without chattering

4.8 and 4.5, where high-frequency oscillations due to chattering were evident, the control inputs are now considerably smoother. While the initial transients remain visible, they stabilize quickly, and the aggressive switching and oscillations dissipate after approximately 20 seconds. The sliding surfaces exhibit a marked improvement, with minimal oscillations compared to the noisy behavior observed earlier. The use of the tanh function effectively suppresses chattering while maintaining the control system's stability and overall performance.

4.5.1.2 Test 2: External Disturbances

In Test 2, the simulation setup is specifically designed to analyse the effects of time-varying external disturbances on Blucy's dynamics. Underwater vehicles are subject to various external influences that can significantly impact their motion and stability. These disturbances primarily include ocean currents, environmental disturbances such as surface waves and turbulence, and the effects of tether cables in ROVs. To model these disturbances, a combination of sinusoidal wave functions and bias is used, representing both periodic and transient influences on the system. The mathematical representation of the external disturbances acting on the vehicle's surge, sway, heave, and yaw directions is given by:

$$\begin{aligned} d_u(t) &= -0.03 \sin\Big(0.06t\Big) \\ d_v(t) &= 0.09 \sin\Big(0.05t + \frac{\pi}{6}\Big) + 0.01 \\ d_w(t) &= 0.1 \sin\Big(0.2t + \frac{\pi}{4}\Big) + 0.08 \\ d_r(t) &= -0.06 \sin\Big(0.5t\Big) \end{aligned} \tag{4.88}$$

The results of this test are depicted in Figures 4.11 - 4.18, illustrating the underwater vehicle's response under the influence of these disturbances. To quantitatively evaluate the performance of the proposed control strategies, a comparison is made between the Fixed-Time Sliding Mode Controller (FTSMC) and the proposed Fixed-Time Sliding Mode Control augmented with Neural Networks (NN) and Disturbance Observer (DO) techniques, indicated in the plots as FTSMNNDO.

For this analysis, the overall tracking error is defined as:

$$\rho_e = \sqrt{x_e^2 + y_e^2 + z_e^2} \tag{4.89}$$

This error metric provides a consolidated measure of the vehicle's deviation from its desired trajectory, allowing the evaluation of control precision.

To further evaluate the controller's performance, standard performance indices are utilised, including the Integrated Absolute Error (IAE), Integrated Square Error (ISE), and Integrated Time Absolute Error (ITAE), calculated as follows:

$$\text{IAE} = \int_0^\infty |\rho_e(t)|\, dt \tag{4.90}$$

$$\text{ISE} = \int_0^\infty \rho_e(t)^2\, dt \tag{4.91}$$

$$\text{ITAE} = \int_0^\infty t \cdot |\rho_e(t)|\, dt \tag{4.92}$$

Figure 4.11 compares the behaviour of FTSMC against FTSMNNDO under the influence of disturbances. The state variables show that while both controllers stabilize the

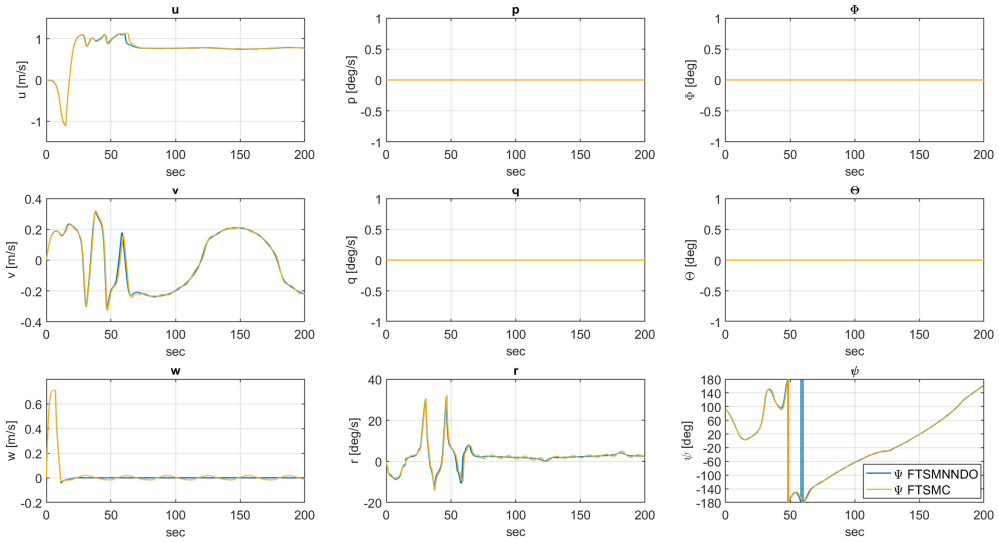

Figure 4.11: State Variables Test 2: FTSMNNDO vs FTCSMC

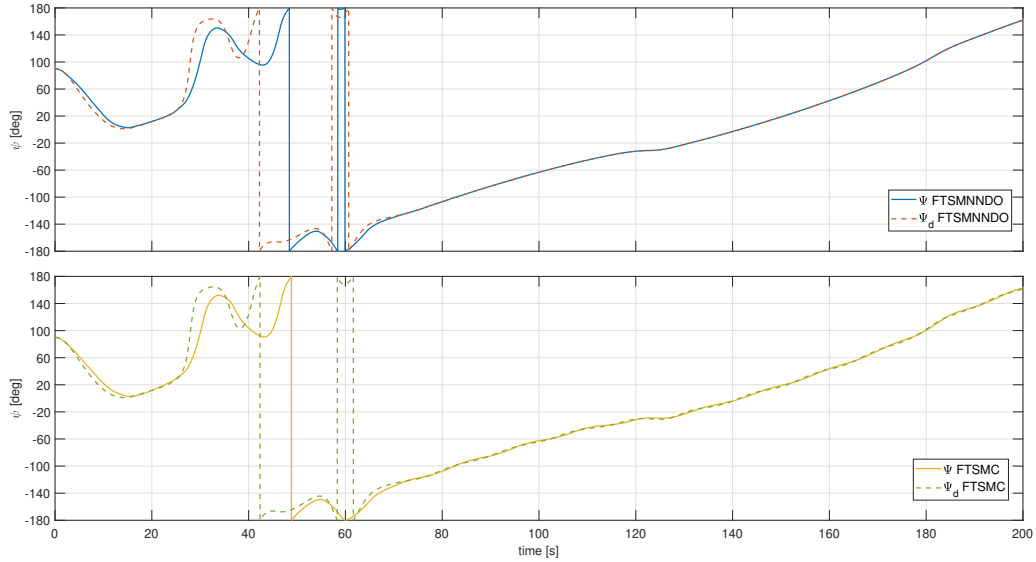

Figure 4.12: Ψ for FTSMNNDO vs FTSMC: Test 2

system, the FTSMNNDO demonstrates improved disturbance rejection, particularly in the heave velocity (w), yaw rate (r) and lateral velocity (v), where oscillations are more effectively minimized. Overall, the controller with DO and NN provides smoother system behaviour as can be seen from Figures 4.13, 4.14, and 4.15. Indeed, from Figure 4.13 it has to be noticed that FTSMC is not able to maintain constant depth throughout the motion. Moreover, from Figure 4.14 and considering x_e and y_e in Figure 4.15, FTSMNNDO is able to converge to the desired trajectory faster than FTSMC. The error ψ_e in Figure 4.15 is primarily caused by the time-varying disturbance $d_v(t)$, to which the yaw dynamics react.

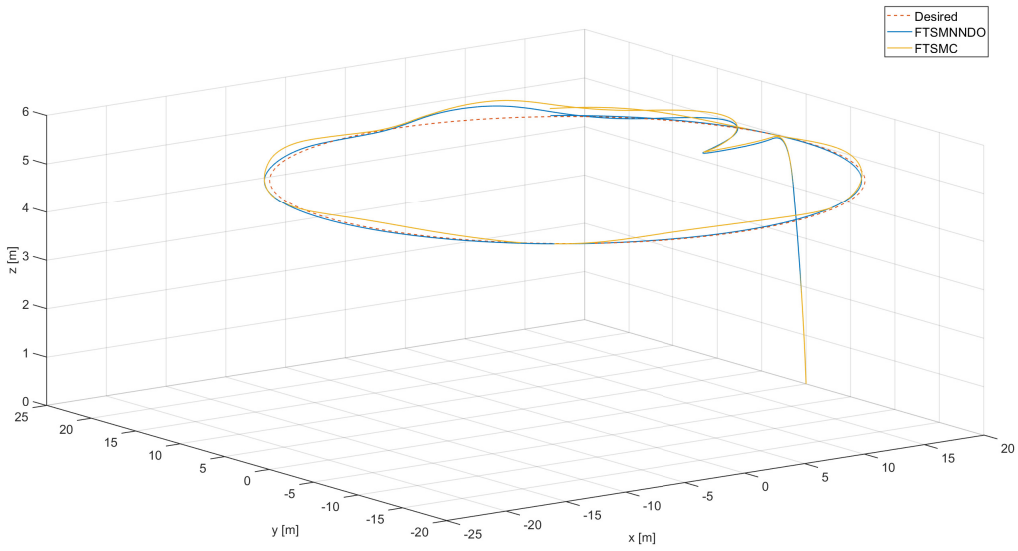

Figure 4.13: Trajectory 3D: Test 2

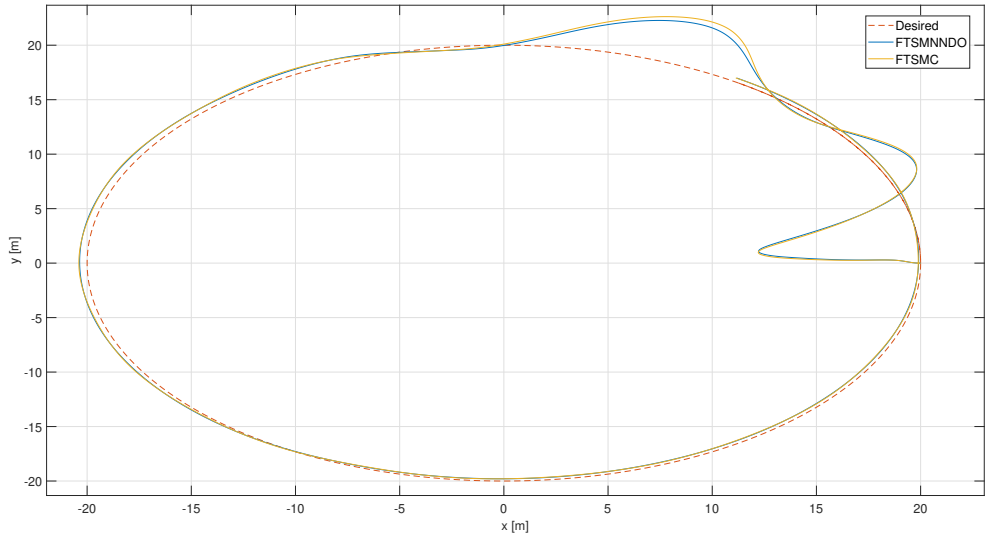

Figure 4.14: Trajectory 2D: Test 2

This disturbance, with both a sinusoidal and constant component, continuously affects the system, making it challenging for the controllers to fully reject its influence on the state variables. While both FTSMC and FTSMNDO attempt to track the desired yaw reference (ψ_d), some error remains due to their limitations in disturbance rejection as can be seen in τ_r in Figure 4.16. The FTSMNDO controller shows better performance with smaller oscillations and faster recovery, while the FTSMC controller exhibits larger tracking errors and slower response, especially when the disturbance becomes more pronounced in the time interval $[30 - 48]$ s of the simulation (See also Figure 4.12).

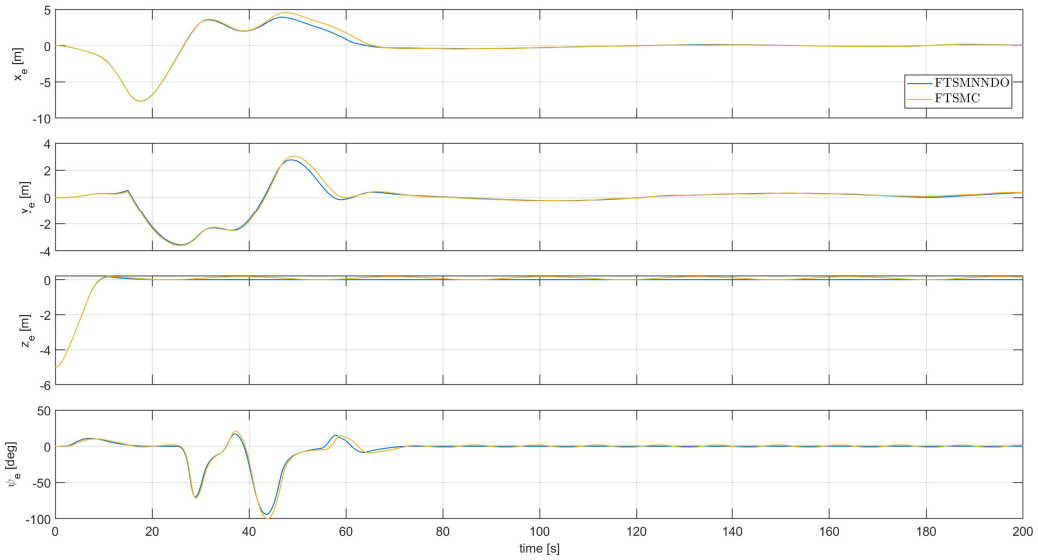

Figure 4.15: Position and Attitude Tracking Error: Test 2

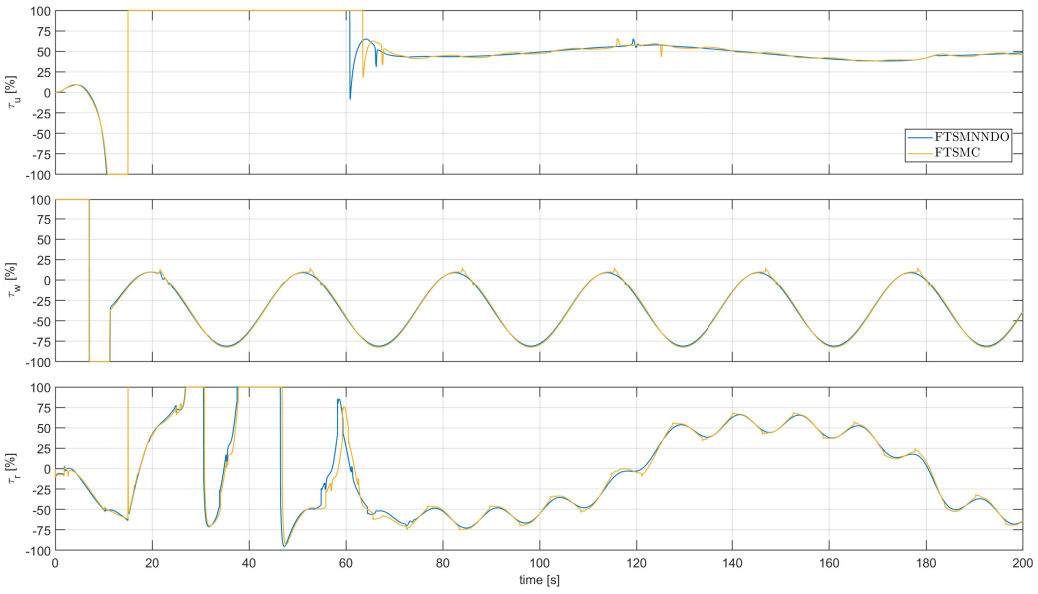

Figure 4.16: Control inputs Test 2: τ_u, τ_w and τ_r

This observation is further substantiated by the quantitative comparison provided in Table 4.2. The results indicate that FTSMNNDO exhibits superior performance across all evaluation metrics. Specifically, FTSMNNDO achieves an ISE that is approximately 9.6% lower than FTSMC, demonstrating a more effective overall error reduction. Similarly, the IAE shows a 7.3% improvement, while the ITAE exhibits the most significant enhancement, being 11.8% lower, reflecting a more efficient time-weighted error reduction.

These quantitative findings reinforce the visual observations from Figure 4.13, demon-

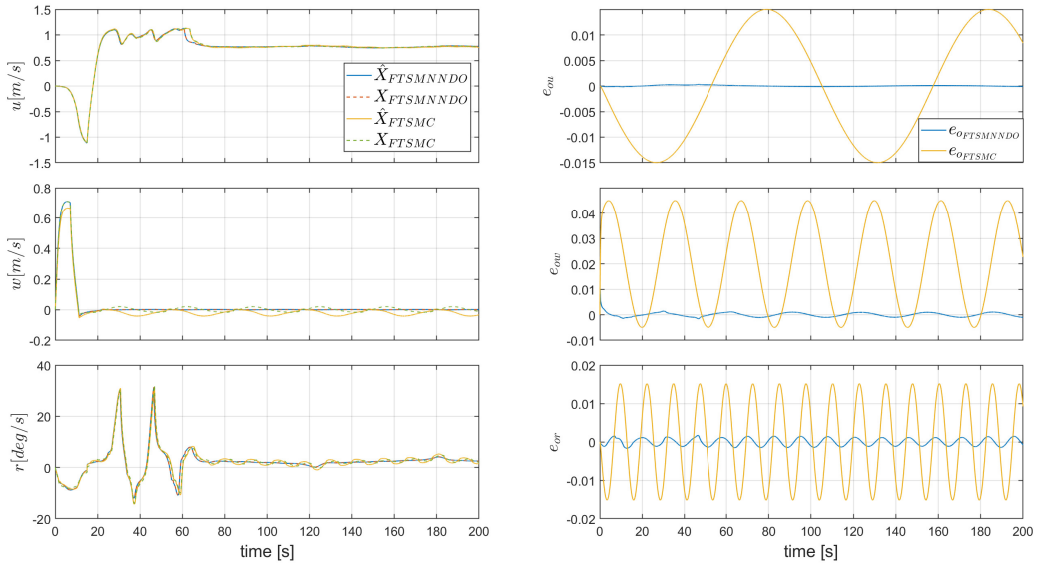

Figure 4.17: State Observer Estimations and Corresponding Estimation Errors: Test 2

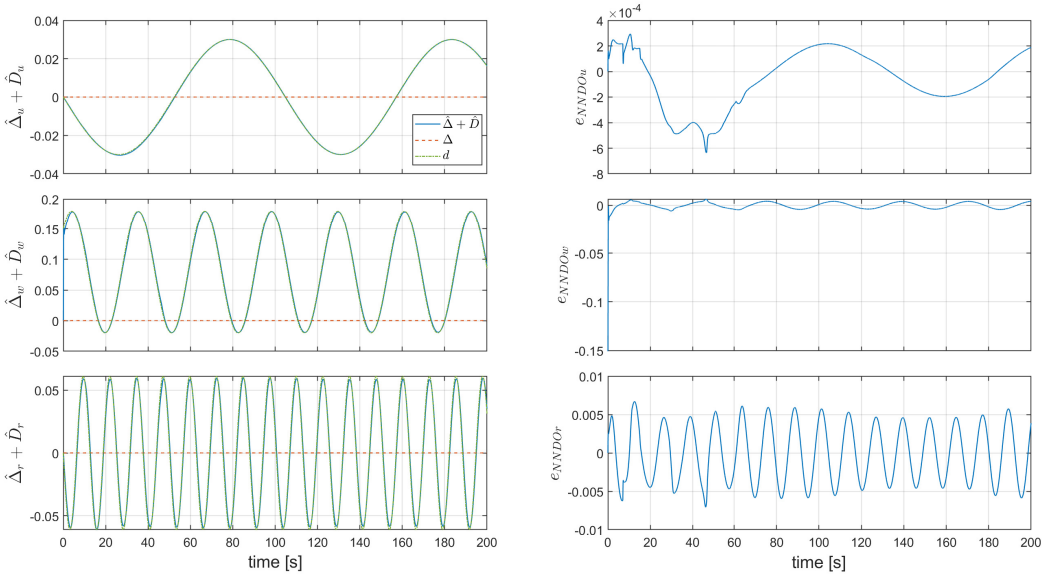

Figure 4.18: $(\hat{\Delta} + \hat{D})$ of Uncertainties and Disturbances: Test 2

strating that FTSMNNDO achieves improved disturbance rejection and smoother control performance. Notably, the enhancement is particularly evident in its ability to reduce the long-term and oscillatory effects of disturbances on the system. While the standard FTSMC alone is inherently robust against disturbances due to the sliding mode control technique, the addition of Neural Networks and Disturbance Observer in FTSMNNDO significantly enhances its overall performance, achieving more precise and stable control. The Figure 4.17 illustrates the superior performance of the FTSMNNDO state estimation

Term	ISE	IAE	ITAE
FTSMC	1158	289	12640
FTSMNNDO	1047	268	11146

Table 4.2: Quantitative comparison in Test 2

in comparison to the FTSMC. The FTSMNNDO leverages DO and NN whose estimates are depicted in Figure 4.18, achieves much more accurate estimations and significantly reduces errors across all state variables. In particular, it exhibits minimal oscillations and maintains low error levels over time, as seen in e_{ou}, e_{ow} and e_{or} that remain small and steady, indicating effective estimation of state and robust disturbance rejection. Conversely, FTSMC, lacking the DO and NN, shows larger and persistent oscillations in the errors, highlighting its reduced capability in handling external disturbances.

4.5.1.3 Test 3: External Disturbances, Model Uncertainties and Actuator faults

The simulations in this scenario are designed to compare the performance of the proposed FTSMNNDO controller against the FTSMC under the influence of external disturbances (4.88), model uncertainties and concurrent actuator faults. These uncertainties are introduced to asses their impact on the 4 DOF system's dynamics (4.14) and to evaluate the controller's ability to compensate for them effectively.

Model uncertainties, in particular, arise due to discrepancies between the nominal model and the actual vehicle, which may result from factors such as inaccurate parameter estimation, unmodeled dynamics, or payload variations during real-world missions. Additionally, actuator faults are modeled as concurrent thrust losses relative to the nominal thrust available from the vehicle's propulsion system. This reflects a realistic scenario where the actuators may not deliver the full expected thrust, introducing further challenges for maintaining system performance.

Considering the system in (4.31) to analytically express the effects of these uncertainties and actuator faults, perturbations are introduced, $\delta f(X)$ and $\delta g(X)$, into the mass, inertia, hydrodynamic coefficients. Specifically, these uncertainties are modeled as deviations in the parameters, reflecting differences between the nominal and actual behavior of the vehicle. The following expressions represent the perturbed dynamics of the system:

$$
\begin{aligned}
m_{11Actual} &= (m + \delta m) - (X_{\dot{u}} + \delta X_{\dot{u}}) \\
m_{22Actual} &= (m + \delta m) - (Y_{\dot{v}} + \delta Y_{\dot{v}}) \\
m_{33Actual} &= (m + \delta m) - (Z_{\dot{w}} + \delta Z_{\dot{w}}) \\
m_{66Actual} &= (I_z + \delta I_z) - (N_{\dot{r}} + \delta N_{\dot{r}}) \\
d_{11Actual} &= (X_u + \delta X_u) + (X_{u|u|} + \delta X_{u|u|})|u| \\
d_{22Actual} &= (Y_v + \delta Y_v) + (Y_{v|v|} + \delta Y_{v|v|})|v| \\
d_{33Actual} &= (Z_w + \delta Z_w) + (Z_{w|w|} + \delta Z_{w|w|})|w| \\
d_{66Actual} &= (N_r + \delta N_r) + (N_{r|r|} + \delta N_{r|r|})|r| \\
\tau_{uActual} &= \tau_u + f_u \\
\tau_{wActual} &= \tau_w + f_w \\
\tau_{rActual} &= \tau_r + f_r
\end{aligned}
\tag{4.93}
$$

with

- δm: uncertainty in vehicle mass.
- $\delta X_{\dot{u}}, \delta Y_{\dot{v}}, \delta Z_{\dot{w}}, \delta N_{\dot{r}}$: uncertainties in added mass coefficients.

- δI_z: uncertainty in yaw inertia.
- $\delta X_u, \delta Y_v, \delta Z_w, \delta N_r$: uncertainties in linear hydrodynamic damping coefficients.
- $\delta X_{u|u|}, \delta Y_{v|v|}, \delta Z_{w|w|}, \delta N_{r|r|}$: uncertainties in quadratic hydrodynamic damping coefficients.
- f_u, f_w, f_r: represents faults on actuator system.

In this case, all uncertainties, represented by the δ terms, are modeled as a percentage of their nominal values. Specifically, each uncertainty is proportional to the original parameter, meaning that $\delta m = \%m$, $\delta X_{\dot{u}} = \%X_{\dot{u}}$, and similarly for the other dynamic terms. Furthermore, actuator faults are incorporated into the simulation using a multiplicative fault model, as outlined in [86]. These faults directly impact the system's inputs by reducing the available thrust or torque, and are defined as:

$$\begin{aligned} f_u &= -l_u \tau_u \\ f_w &= -l_w \tau_w \\ f_r &= -l_r \tau_r \end{aligned} \tag{4.94}$$

where $0 \leq l_u, l_w, l_r \leq 1$. In this context, l_u, l_w, and l_r represent the fault levels in the surge, heave, and yaw control inputs, respectively. A value of $l = 0$ signifies no fault, where the control input is fully available, while $l = 1$ indicates a total failure, meaning the actuator provides no control effort.

By substituting both the modeled uncertainties and actuator faults from (4.93) and (4.94) into the 4-DOF dynamic model (4.14), the complete system dynamics under the influence of these uncertainties and faults becomes:

$$\begin{aligned} \dot{u} &= \frac{1}{m_{11}} \left(m_{22} v r - d_{11} u + \tau_u + d_u \right) + \delta u + \frac{f_u}{m_{11}} \\ \dot{v} &= \frac{1}{m_{22}} \left(-m_{11} u r - d_{22} v + d_v \right) + \delta v \\ \dot{w} &= \frac{1}{m_{33}} \left(-d_{33} w + \tau_w + d_w \right) + \delta w + \frac{f_w}{m_{33}} \\ \dot{r} &= \frac{1}{m_{66}} \left(\left(m_{11} - m_{22} \right) u v - d_{66} r + \tau_r + d_r \right) + \delta r + \frac{f_r}{m_{33}} \end{aligned} \tag{4.95}$$

where:

$$\begin{aligned} \delta u &= \frac{1}{m_{11}} \Big((-\delta m + \delta X_{\dot{u}}) \dot{u} + (\delta m - \delta Y_{\dot{v}}) v r - (\delta X_u + \delta X_{u|u|} |u|) u \Big) \\ \delta v &= \frac{1}{m_{22}} \Big((-\delta m + \delta Y_{\dot{v}}) \dot{v} - (\delta m - \delta X_{\dot{u}}) u r - (\delta Y_v + \delta Y_{v|v|} |v|) v \Big) \\ \delta w &= \frac{1}{m_{33}} \Big((-\delta m + \delta Z_{\dot{w}}) \dot{w} - (\delta Z_w + \delta Z_{w|w|} |w|) w + f_w \Big) \\ \delta r &= \frac{1}{m_{66}} \Big((-\delta I_z + \delta N_{\dot{r}}) \dot{r} + (-\delta X_{\dot{u}} + \delta Y_{\dot{v}}) u v - (\delta N_r + \delta N_{r|r|} |r|) r \Big) \end{aligned} \tag{4.96}$$

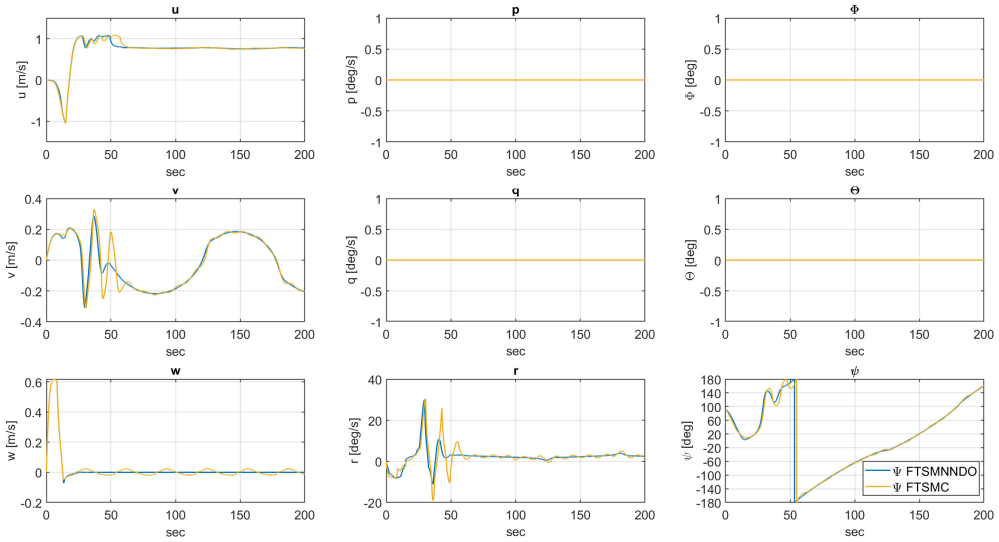

(a) State Variables

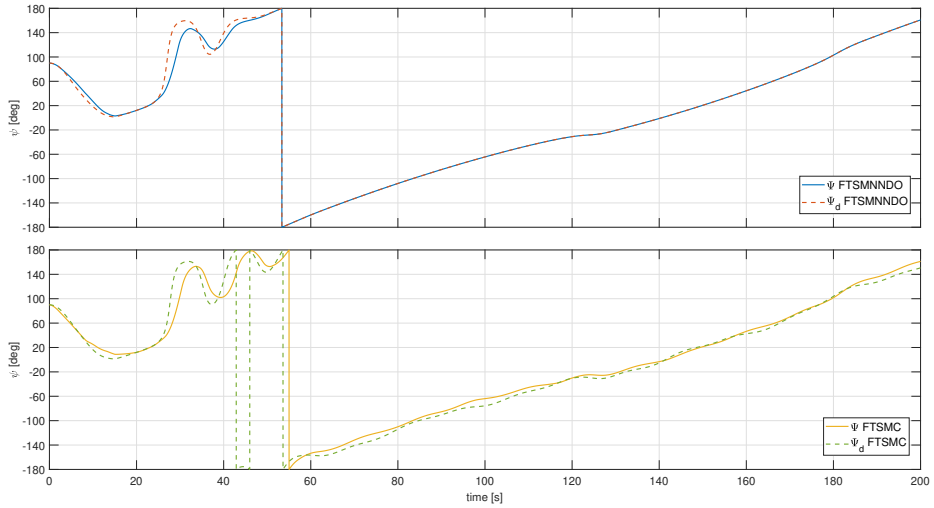

(b) Ψ for FTSMNNDO vs FTSMC

Figure 4.19: Comparison of FTSMNNDO and FTCSMC State Variables with 20% of uncertainties and 15% of thrust losses.

Remark 4.5.2. *Recalling that* $\Delta(X) = \dot{R}(\psi)X + R(\psi)(\delta f(X) + \delta g(X)\tau)$ *and* $R(\psi) = diag(\cos(\psi + \beta - \gamma_p), 1, 1)$*, using the guidance law defined in section 4.3, it can be shown that:*

$$\cos(\psi + \beta - \gamma_p) \approx 1$$

It follows that $R(\psi) \approx I$*, where* I *is the identity matrix and* $\dot{R}(\psi) \approx 0$*. Consequently, one has:*

$$\Delta(X) \approx \delta f(X) + \delta g(X)\tau$$

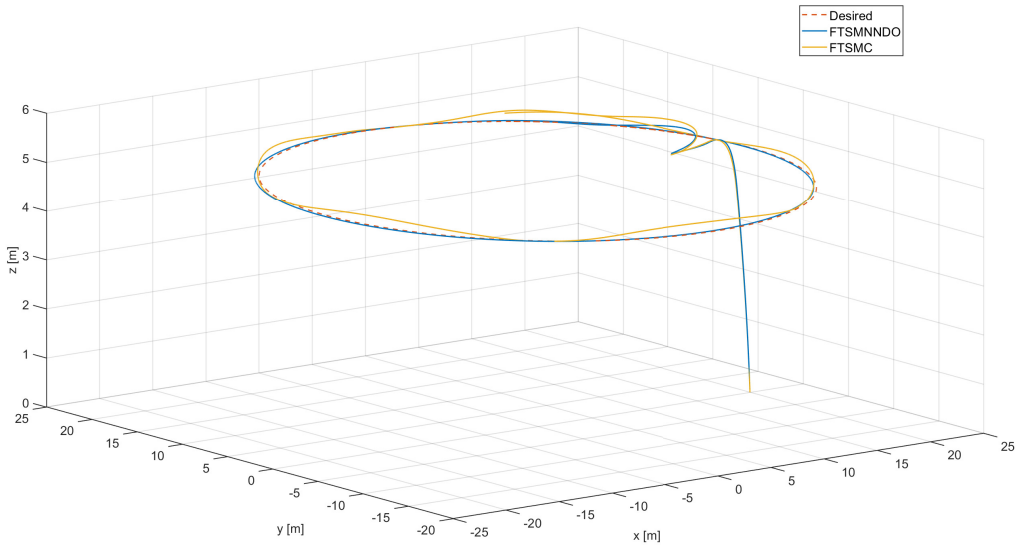

(a) 3D Trajectory

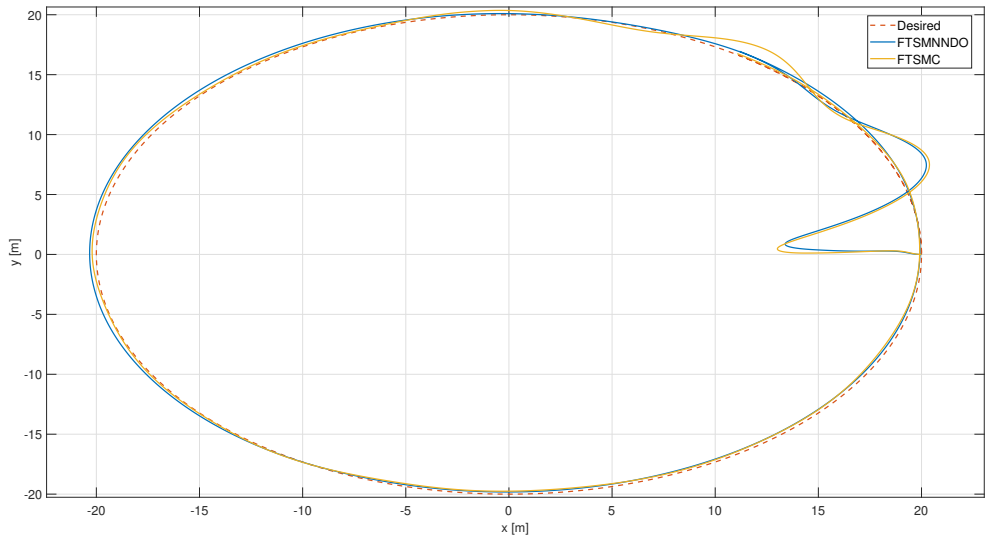

(b) 2D trajectory

Figure 4.20: Comparison of FTSMNNDO and FTCSMC Trajectories with 20% of uncertainties and 15% of thrust losses.

The simulation result presented in Figure 4.19 - 4.23 along with Table 4.3, demonstrate the clear superiority of the FTSMNDO controller over the FTSMC in the presence of external disturbances (4.88), 20% model uncertainties, and 15% of efficiency losses in all actuators. In Figure 4.19, the states variables illustrate how the FTSMNNDO controller is able to quickly dampen oscillations in the variable w, v and r, leading to a faster stabilization compared to the FTSMC. This faster response is also visible in the trajectory (Figure 4.20), where the FTSMNNDO drives the vehicle to converge to the desired trajec-

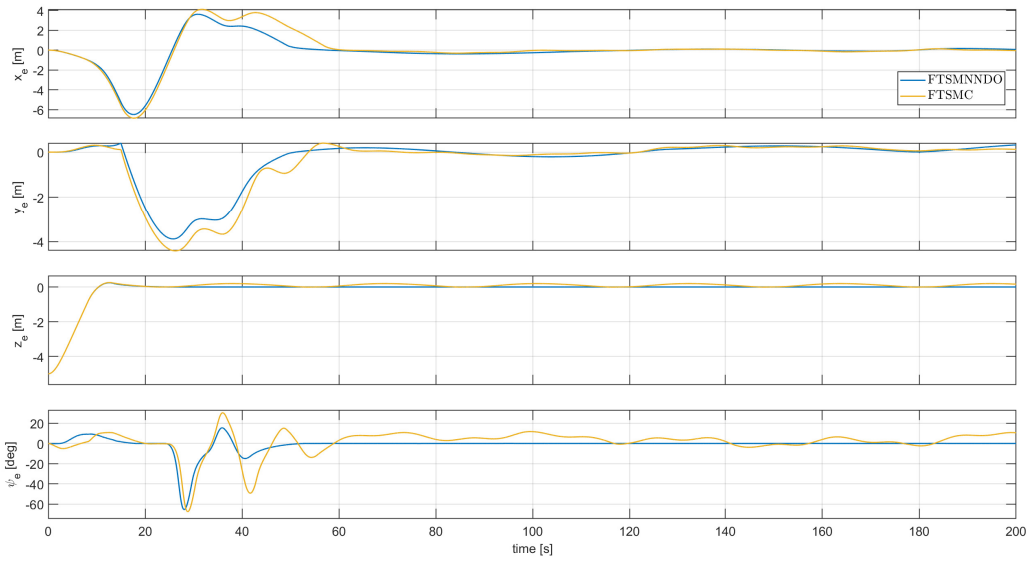

Figure 4.21: FTSMNNDO and FTSMC Position and Attitude Tracking Error with 20% of uncertainties and 15% of thrust losses

tory with minimal tracking error. The FTSMC, on the other hand, experiences significant oscillations, particularly in the z axis. This behaviour is confirmed also in the tracking error Figure 4.21. Importantly, the reduced control effort required by FTSMNNDO, as shown in Figure 4.22, highlights its efficiency in handling uncertainties and faults, while using less energy compared to FTSMC.

This simulation scenario proves the crucial importance of incorporating NN and DO within the control architecture, indeed in Figures 4.23a it can be seen that the state estimation error remain close to zero for the FTSMNNDO, thanks to the real time adaptation provided by the NN and DO. Figure 4.23b further emphasizes the importance of these estimation mechanism, where the NN+DO, $(\hat{\Delta} + \hat{D})$, accurately tracks the disturbances as well as uncertainty and faults affecting the system.

In test 3, FTSMNNDO clearly demonstrates its potential, with performance differences between FTSMNNDO and FTSMC becoming more pronounced in the challenging environment (Table 4.3). FTSMNNDO achieves an ISE that is 26.3% lower, an IAE 17.1% lower, and an ITAE 17.9% lower than FTSMC, highlighting its superior ability to handle uncertainties and multiple actuator faults. In Test 2, with only disturbances present, FTSMNNDO still outperformed FTSMC but by smaller margins, emphasizing its advantages in complex scenarios.

To further validate the robustness of the proposed FTSMNNDO controller, additional simulations are conducted with an increasing magnitude of actuator faults. From the Table 4.4 it is evident that FTSMNNDO controller can handle up to 20% fault magni-

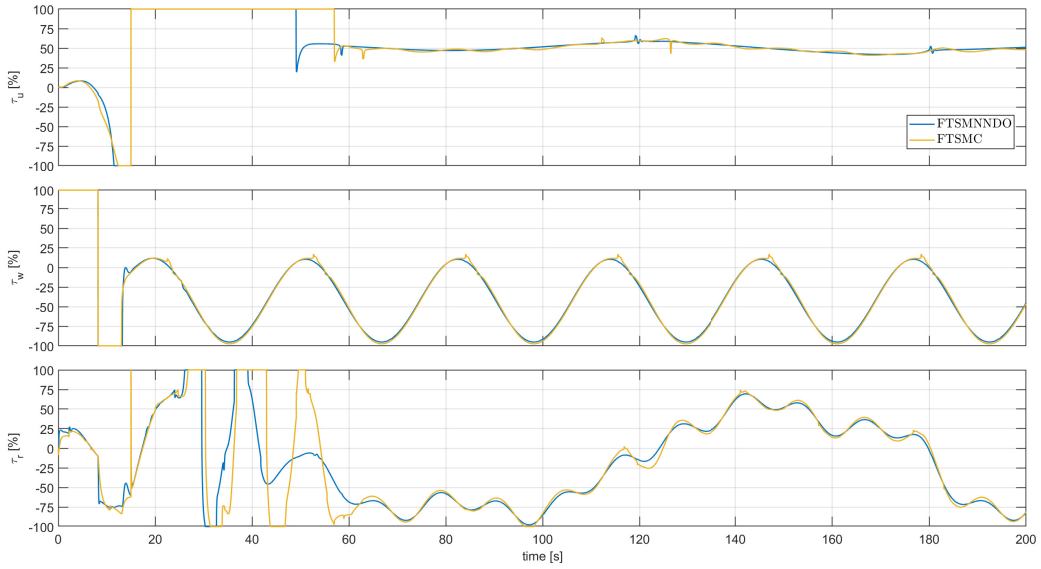

Figure 4.22: FTSMNNDO and FTCSMC Control inputs with 20% of uncertainties and 15% of thrust losses: τ_u, τ_w and τ_r

Term	ISE	IAE	ITAE
FTSMC	1057	257	10026
FTSMNNDO	779	213	8230

Table 4.3: Quantitative comparison in Test 3 in presence of 20% Uncertainties and 15% multiple fault on thrusters.

tude without failure, maintaining performance and stability, as resflected by the relatively consistent values of ISE, IAE and ITAE. Even as the fault magnitude increases, FTSMNNDO demonstrates its resilience, with error values gradually increasing but without drastic degradation. In contrast, the FTSMC controller fails at 17.2% fault magnitude, as seen by the dramatic surge in ISE, IAE, and ITAE, indicating its inability to maintain stability beyond this point.

This ability of FTSMNNDO to handle up to 20% simultaneous actuator faults without failure, underscoring its superior active fault-tolerant capability, is largely thanks to the estimations provided by the NN and DO. These estimators, effectively adapt to the uncertainties and disturbances introduces by the faults, allowing the control system to compensat for the lost actuator efficiency. This allows FTSMNNDO to maintain stability and minimize error, even in the face of severe actuator faults. In contrast, FTSMC lacks this adaptive estimation mechanism, making it far more vulnerable to higher levels of faults.

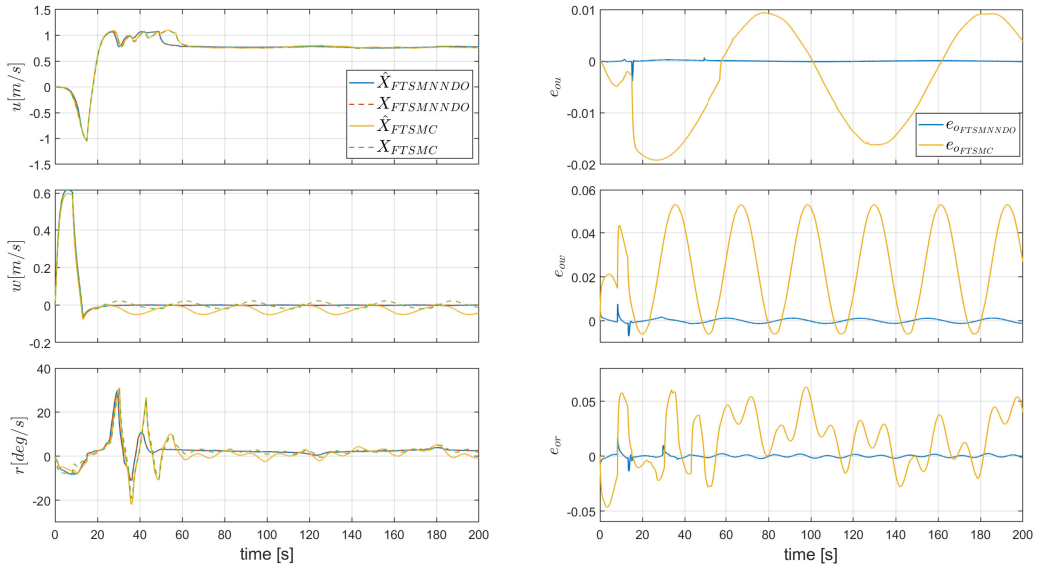

(a) FTSMNNDO and FTSMC State Observer Estimations and Estimation Errors

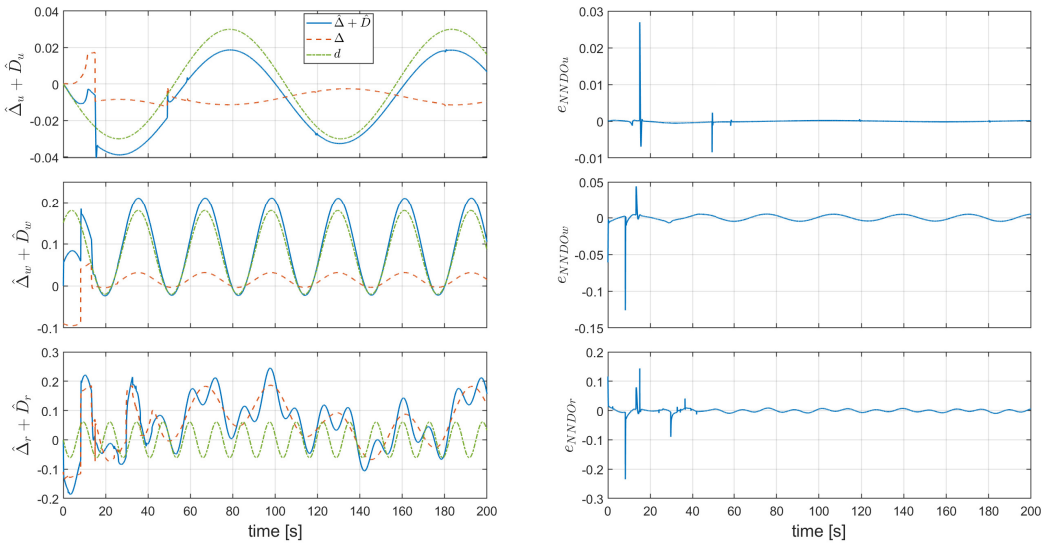

(b) $\hat{\Delta} + \hat{D}$ of FTSMNNDO

Figure 4.23: State observer and $\hat{\Delta} + \hat{D}$ in presence of 20% of uncertainties and 15% of thrust losses

4.5.2 6 DOF Simulations

This section presents the result of trajectory tracking control, comparing the performances of the proposed FTSMNNDO control scheme with the FTSMC, using the complete 6-DOF benchamrk of Blucy. The comparison evaluates each controller's ability to handle the nonlinearities and coupling effect in a more comprehensive and realistic dynamic setting. However, unlike the simplified model, the 6-DOF model includes additional dy-

Fault	FTSMC				FTSMNNDO			
Magnitude %	IAE	ISE	ITAE	Failure	IAE	ISE	ITAE	Failure
16	1049.37	254.51	9898	No	772.31	211.99	8166.52	No
16.5	1052.73	255.12	9943.05	No	769.2	211.34	8138.55	No
17	1066.64	258.99	10170.3	No	766.38	210.72	8109	No
17.2	79298.94	3263.13	433863.99	Yes	765.32	210.45	8093.43	No
17.5	233849.98	5475.44	742291.7	Yes	763.72	209.96	8060	No
18	268514.04	5940.27	8070065	Yes	761	208.81	7969.77	No
18.5	294519	6211	846164	Yes	758.51	207.55	7862.77	No
19	305173	6327	862990	Yes	756.71	208.09	7949	No
19.5	314647	6425	877649	Yes	758.64	212.98	8513	No
20	322476	6504	889609	Yes	772.61	221.48	9468.39	No
21	323108	6512	891829	Yes	42429	1824	281030	Yes

Table 4.4: Comparison of IAE, ISE, and ITAE for FTSMC and FTSMNNDO under different fault conditions

namics associated with roll (ϕ), pitch (θ), and lateral sway (v), leading to significant nonlinear coupling between the different degrees of freedom.

In this 6-DOF benchmark model, Blucy's motion is represented across six degrees of freedom, where the inclusion of roll (ϕ) and pitch (θ) significantly impacts system dynamics. This configuration introduces nonlinear coupling, particularly between lateral and vertical dynamics, as well as buoyancy-related forces, resulting in more complex interactions during the trajectory tracking task.that further influence stability and maneuverability. For example, the vehicle's forward motion (u), sway (v), and yaw (r) are now coupled with the pitch (θ) and roll (ϕ) motions, leading to oscillatory behaviors that were not present in the 4-DOF model.

In the following tests, two different trajectories will be considered: circular trajectory for test 1 and test 2; multibeam (MBES) survey trajectory in test 3. The circular spatial trajectory from the 4-DOF simulations is adapted for the 6-DOF model. Unlike the 4-DOF trajectory, which included a waiting phase, the trajectory here is structured as a continuous descent followed by simultaneous circular motion and depth maintenance, totaling 400 seconds of simulation time. The trajectory is divided into two phases:

- **Phase 1: Descent and Circular Initiation** ($0 \text{ s} \leq \text{t} \leq 10 \text{ s}$) — During this phase, the depth $z_d(t)$ changes linearly from 0 to 5 meters, while $x_d(t)$ and $y_d(t)$ follow a circular path based on the radius R and period T.

- **Phase 2: Continuous 2D Circular Motion** ($10 \text{ s} < \text{t} \leq 400 \text{ s}$) — After reaching the target depth, Blucy continues to follow a circular trajectory at a constant depth

of 5 meters, completing one full circumference over 380 seconds.

$$\begin{cases} x_d(t) = R\cos\left(\frac{2\pi}{T}t\right) \\ y_d(t) = R\sin\left(\frac{2\pi}{T}t\right) \\ z_d(t) = \begin{cases} \frac{-5}{10}t & \text{if } 0 \le t \le t_2 = 10 \text{ s} \\ -5 & \text{if } t > t_2 = 10 \text{ s} \end{cases} \\ \psi_d(t) = \tan^{-1}\left(\frac{\sin\left(\frac{2\pi}{T}(t-t_2)\right)}{\cos\left(\frac{2\pi}{T}(t-t_2)\right)}\right) \end{cases} \tag{4.97}$$

The desired trajectory follows these mathematical expressions, where the radius $R = 20\,\text{m}$, the completion time for a full circumference $T = 380\,\text{s}$, and $t_2 = 10\,\text{s}$ to account for the descent duration.

The MBES survey trajectory used in Test 3 replicates the survey pattern typically followed during multibeam echosounder (MBES) operations. The trajectory consists of parallel transects connected by smooth semicircular turns at each end, as shown in Figure 4.24. This pattern ensures uniform data coverage and controlled overlaps between adjacent transects, mimicking real-world operation, and optimizing data reliability. The trajectory generation process begins with the definition of a set of waypoints that represent the desired positions of the vehicle in the horizontal plane. These waypoints are arranged to create a series of parallel transects, each 50 meters in length, positioned at a distance of 20 meters from each other. This configuration is designed to account for the MBES swath width, ensuring controlled overlaps between adjacent transects to improve data resolution and avoid coverage gaps. Smooth transitions between transects are achieved by introducing semicircular arcs at the turning points, ensuring continuous and smooth motion along the survey path. The trajectory is generated by interpolating between these waypoints to create a piecewise continuous path. Along the linear transect segments, the vehicle position changes linearly between the waypoints, maintaining a constant forward speed of $u = 5\ m/s$. At the ends of each transect, the vehicle performs smooth semicircular turns, mathematically defined, to transition to the next transect. During these turns, the vehicle's heading angle $\psi_d(t)$ is dynamically adjusted to follow the curvature of the arc. Throughout the trajectory, Blucy maintains a constant depth of $z_d = 5\ m$, providing stable conditions for the MBES data acquisition. The total simulation time for this trajectory is 800 seconds, allowing sufficient duration to evaluate the vehicle control performance during an extended survey mission.

The initial conditions and control parameters for the 6-DOF simulations are set as in the 4-DOF model, with $p(0) = q(0) = \phi(0) = \theta(0) = 0$, to account for the lateral dynamics neglected in the 4 DOF model.

To further increase the realism of the simulation, a current model has been integrated

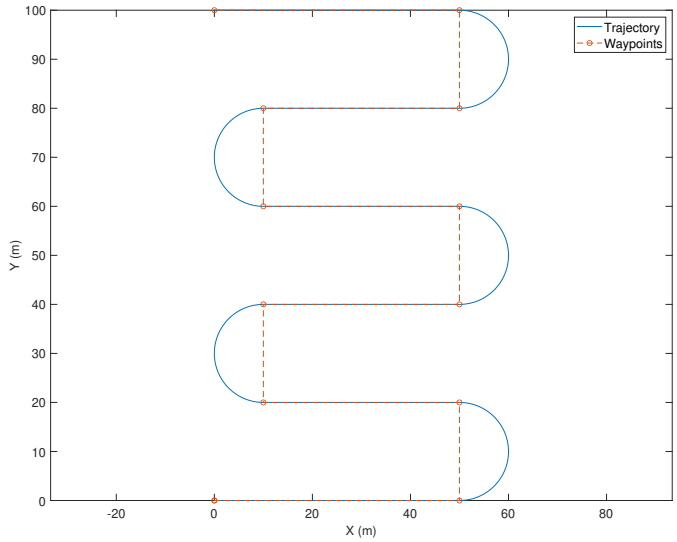

Figure 4.24: MBES Survey Trajectory

into the 6-DOF simulations instead of using a generic disturbance model. The Ocean current is modeled as a 2D constant irrotational flow with constant velocity components in the North-East-Down (NED) reference frame [10]. The current introduces additional forces and moments acting on Blucy, affecting its dynamics. The current model is defined by a velocity vector in the Flow reference frame then it is transformed to obtain in the NED frame as follows:

$$V_c^n = R_f^n \begin{bmatrix} V_c \\ 0 \\ 0 \end{bmatrix} \tag{4.98}$$

where R_f^n is the rotation matrix from flow reference frame to inertial reference frame defined as follows:

$$R_f^n = \begin{bmatrix} cos(\beta) & sin(\beta) & 0 \\ -sin(\beta) & cos(\beta) & 0 \\ 0 & 0 & 1 \end{bmatrix} \tag{4.99}$$

which then can be transformed to body reference using Euler angle rotation matrix as follows:

$$V_c^b = R_b^{nT} \begin{bmatrix} u_c cos(\beta) \\ v_c sin(\beta) \\ 0 \end{bmatrix} \tag{4.100}$$

Now the current induces hydrodynamic forces and moments on Blucy, which can be expressed as functions of the relative velocity between the current and the vehicle's velocity in the body-fixed frame can be calculated using (2.35). Based on real measurements of the Adriatic Sea, a current speed of 0.2 , m/s is implemented in the simulations, with the

current direction defined by the angle β. For Test 1 and Test 3, a current angle of $\beta = 90°$ is used, while $\beta = 0°$ is implemented in Test 3. The chosen current speed of 0.2 , m/s lies within the observed range of 0.08 to 0.20 m/s, reflecting typical current speeds reported in the high and central Adriatic regions. This range, supported by high-frequency radar and drifter studies, captures the variability induced by local winds, seasonal influences, and thermohaline structures specific to the Adriatic Sea [87, 88, 89].

4.5.2.1 Test 1: Unmodeled Dynamics and Ocean Current

This test evaluates the performance of both control systems, the FTSMNNDO and FTSMC, under conditions of nonlinear coupling and ocean current uncertainty. Unlike the 4-DOF simulations, where explicit uncertainty and disturbance signals are introduced to facilitate comparisons with estimation methods, the 6-DOF model does not incorporate predefined uncertainty or disturbance signals for direct comparison. Instead, the system's inherent non linearity, particularly the coupling between different degrees of freedom and the influence of ocean currents, naturally introduce uncertainties into the dynamics. Consequently, it is challenging to directly compare the estimations made by the Neural Network (NN) and Disturbance Observer (DO) with specific disturbance signals, as was possible in the 4 DOF case.

However, the aim here is to evaluate how the estimation of these complex, unmodeled dynamics by the NN and the compensation for external forces by the DO can improve the control system's overall performance. The result are presented in Figures 4.25 - 4.29. In Figure 4.25, in terms of linear velocities (u, v, w), both controllers demonstrate similar responses, but the FTSMNNDO controller achieves slightly smoother transitions with fewer oscillations, particularly in the u and v. The FTSMNNDO's impact is most noticeable in the angular rates (p, q, r), where it significantly dampens oscillations faster than FTSMC. This quicker damping effect allows the FTSMNNDO to stabilize the vehicle's orientation more efficiently, as evident in the reduced oscillations in the attitude angles (ϕ, θ, ψ). This suggests that the disturbance observer and neural network (NN) improve stability by compensating for nonlinear effects and currents. In contrast, FTSMC struggles to handle the nonlinear coupling, leading to persistent oscillations in the angular velocities and yaw rate.

Both controllers closely follow the desired trajectory, as shown in the 3D and 2D trajectory plots (Figure 4.26). However, a comparison of the position and attitude tracking errors (Figure 4.27 reveals that FTSMNNDO consistently achieves smaller errors across all axes, especially in yaw tracking. This deviation indicates that the FTSMC has difficulty maintaining accurate tracking under the same conditions, committing an error around 20°. Additionally, the thruster input plots (Figure 4.28) show that FTSMNNDO main-

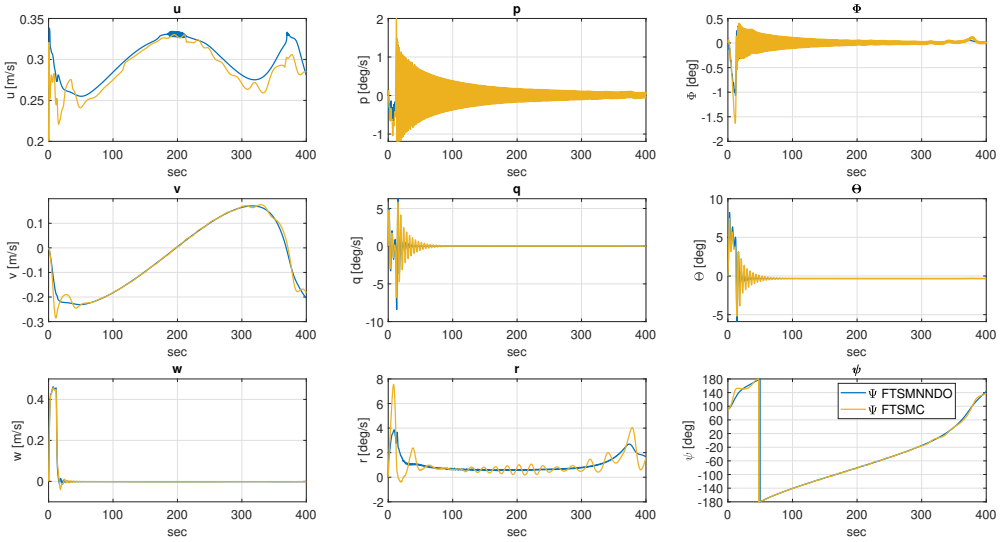

(a) State Variables

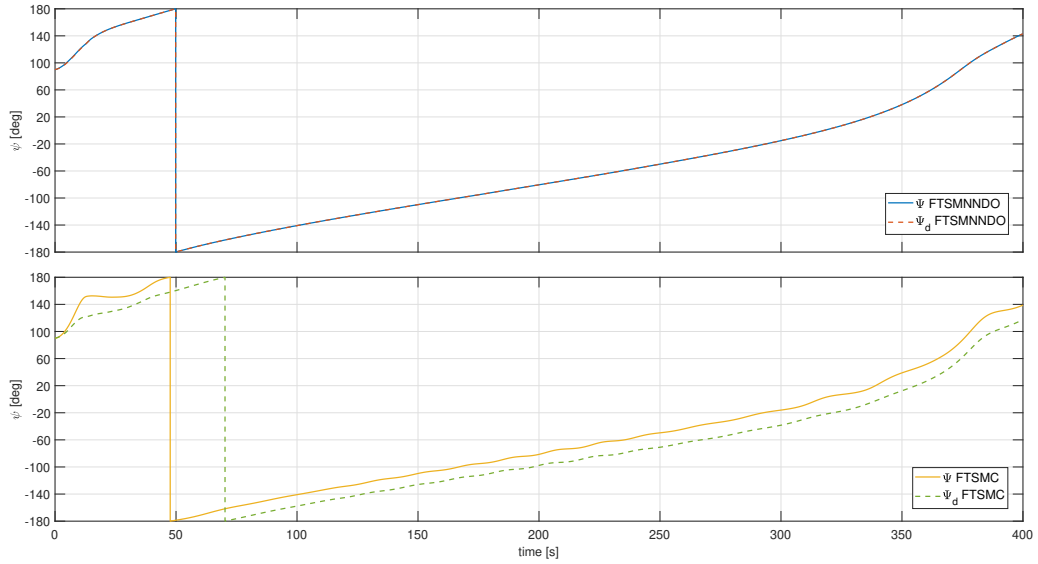

(b) Ψ for FTSMNNDO vs FTSMC

Figure 4.25: 6 DOF State Variables of FTSMNNDO and FTCSMC with Unmodeled Uncertainty and Ocean Current.

tains smoother control actions. As expected, the results in Figure 4.29 align with findings from the 4-DOF test, where FTSMNNDO achieved lower estimation errors, benefiting from neural network and disturbance observer estimations. Table 4.5 further highlights FTSMNNDO's advantages in the 6-DOF model, showing an 18.03% reduction in ISE, a 7.14% reduction in IAE, and a 38.38% reduction in ITAE compared to FTSMC. These improvements are more pronounced than in the 4 DOF case, given the influence of un-

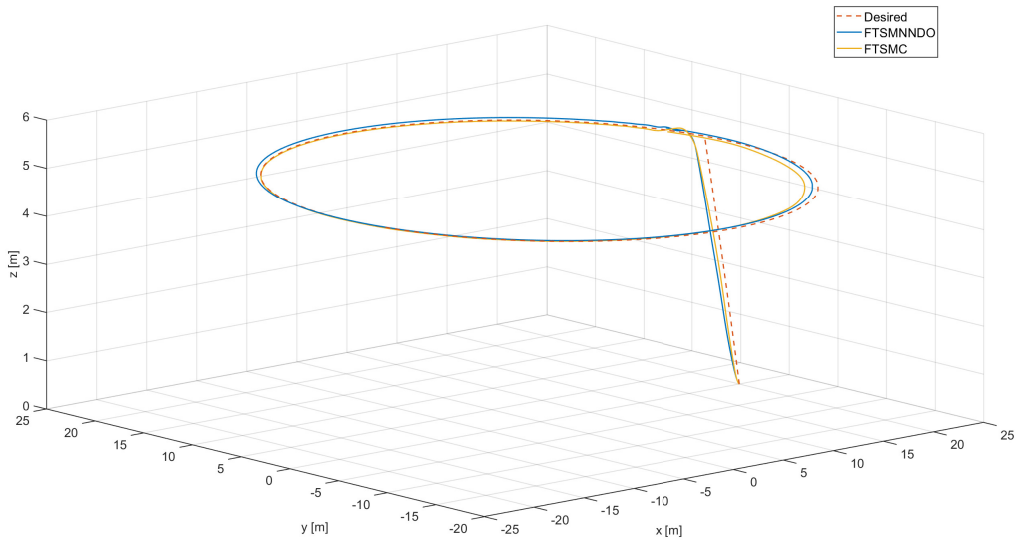

(a) 3D Trajectory

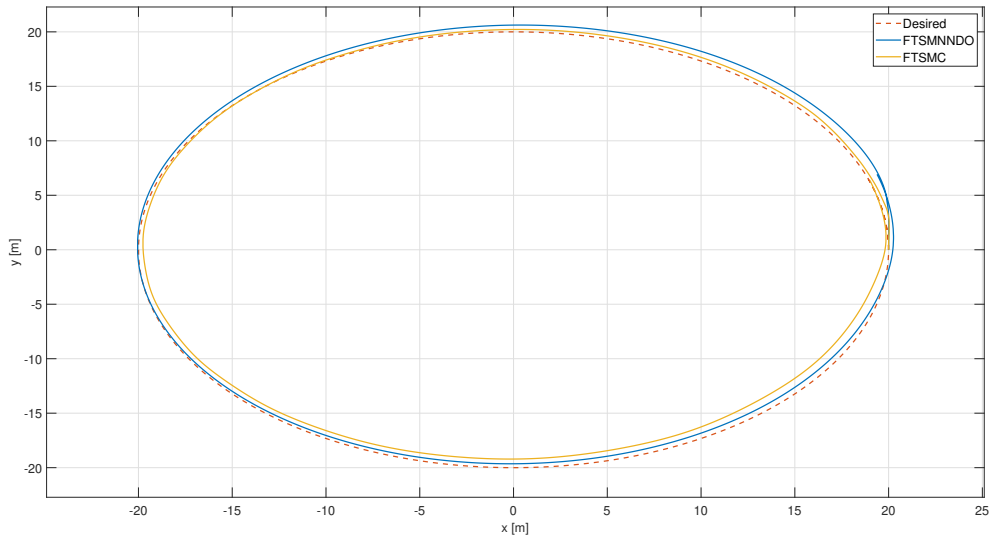

(b) 2D trajectory

Figure 4.26: 6 DOF Trajectories of FTSMNNDO and FTCSMC with unmodeled Uncertainty and Ocean Current.

modeled dynamics and ocean currents in the 6 DOF environment. This comprehensive comparison confirms FTSMNNDO's robustness and accuracy, particularly in challenging conditions with complex dynamics.

4.5.2.2 Test 2: Unmodeled Dynamics, Ocean Current and Actuator faults

As in Section 4.5.1.3, both controllers are tested under unmodeled uncertainty, ocean currents, and actuator faults. In this scenario, a multiplicative incipient fault is intro-

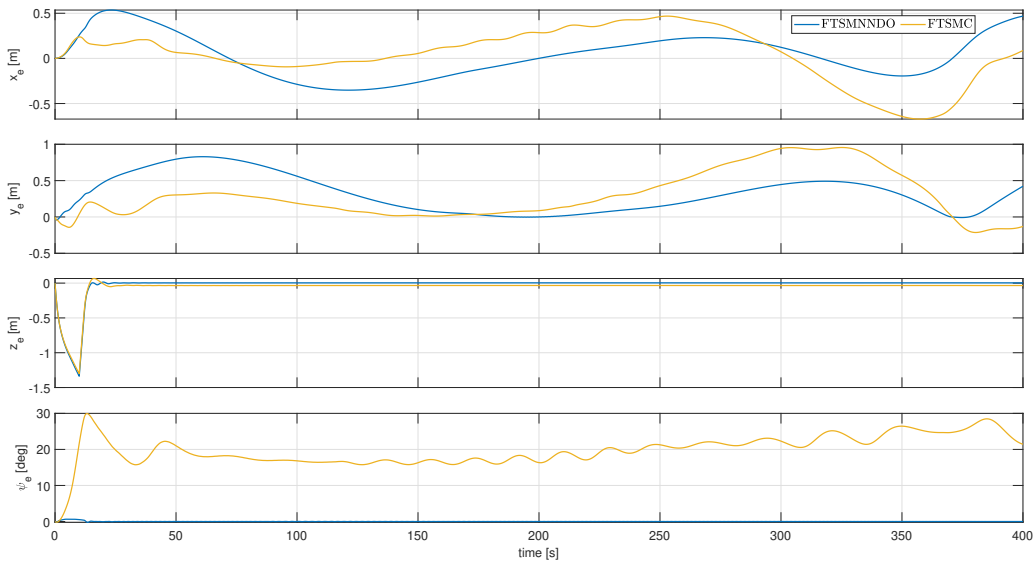

Figure 4.27: 6 DOF Position and Attitude Tracking Error of FTSMNNDO and FTSMC with unmodeled Uncertainty and Ocean Current.

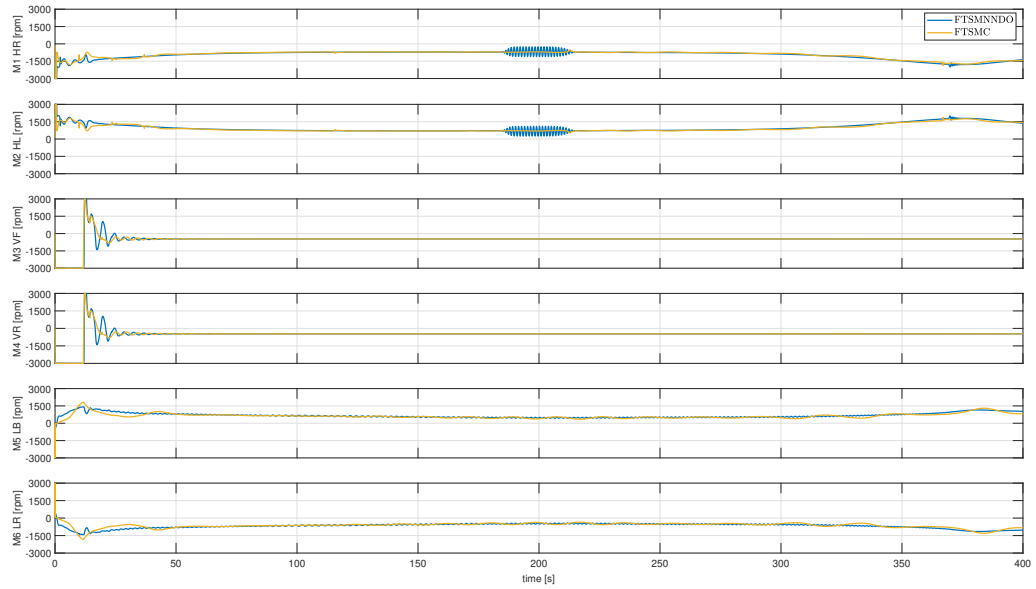

Figure 4.28: 6 DOF Thrusters inputs of FTSMNNDO and FTCSMC with Unmodeled Uncertainty and Ocean Current.

duced in M5 thruster (lateral bow) at $t = 150$ s, modeled as $f_{M5} = -l_{M5}\tau_{M5}$. This fault progressively reduces the effective thrust of M5, and the fault level l_{M5} will be incrementally increased to determine each controller's ability to track the desired trajectory. The goal is to determine the maximum fault level at which each control scheme can maintain stability and tracking accuracy, under the combined influence of ocean currents,

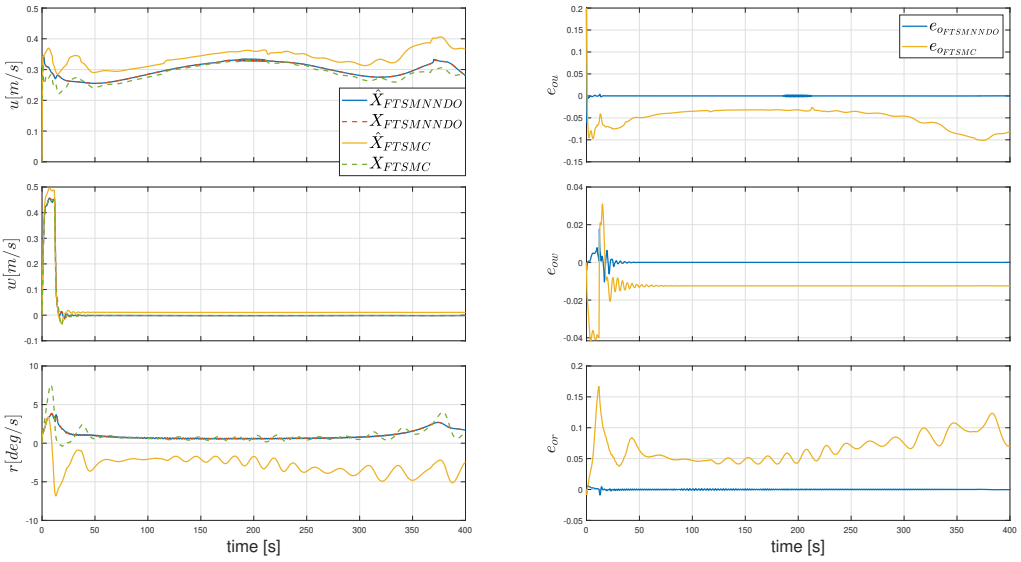

(a) 6 DOF State Observer Estimations and Estimation Errors of FTSMNNDO and FTSMC.

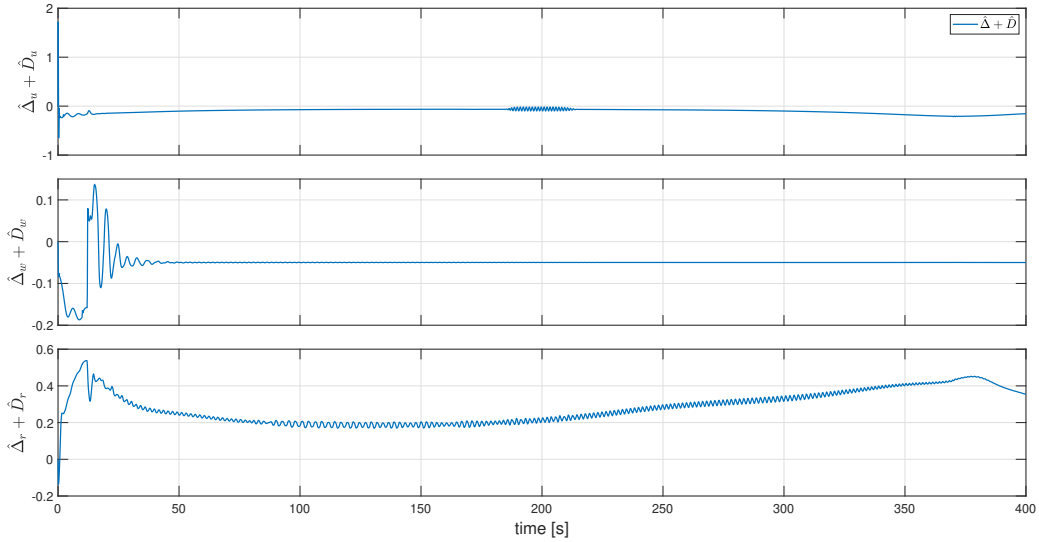

(b) $\hat{\Delta} + \hat{D}$ of FTSMNNDO.

Figure 4.29: 6 DOF State observer and $\hat{\Delta} + \hat{D}$ in presence of Unmodeled Uncertainty and Ocean Current.

unmodeled dynamics, actuator faults, and the specified trajectory. Simulation results are presented for an initial fault magnitude of $l_{M5} = 0.2$, shown in Figures 4.30 - 4.34. As observed in the state variables and tracking error plots(Figures 4.30 and 4.32), the FTSMC controller fails to maintain accurate trajectory tracking after the fault, with oscillations emerging in response to the disturbance. This degradation leads to notable deviations in ϕ and ψ angles, disrupting the overall stability and precision of trajectory tracking.

Term	ISE	IAE	ITAE
FTSMC	122	182	43900
FTSMNNDO	100	169	27061

Table 4.5: Quantitative comparison in 6 DOF in the presence of Unmodeled Uncertainty and Ocean Current.

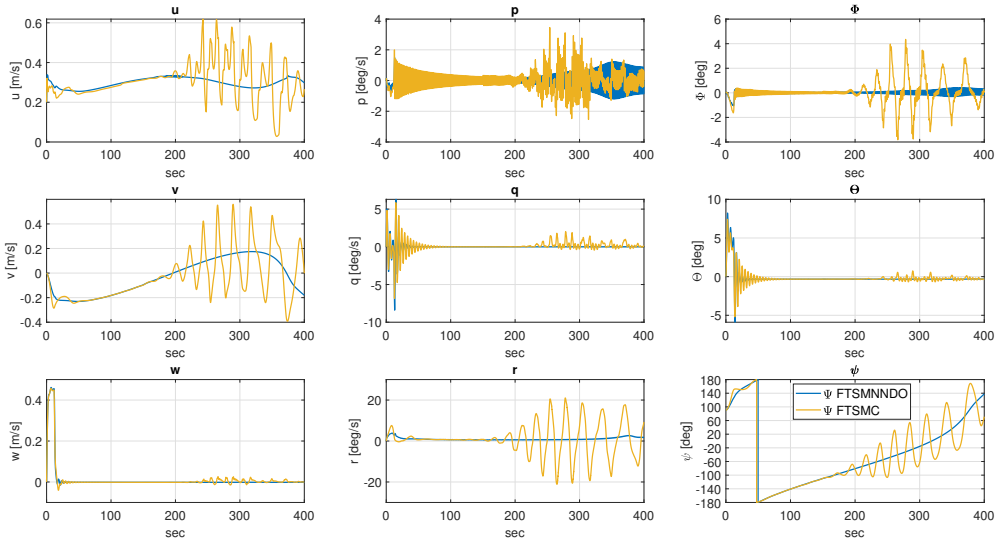

(a) State Variables

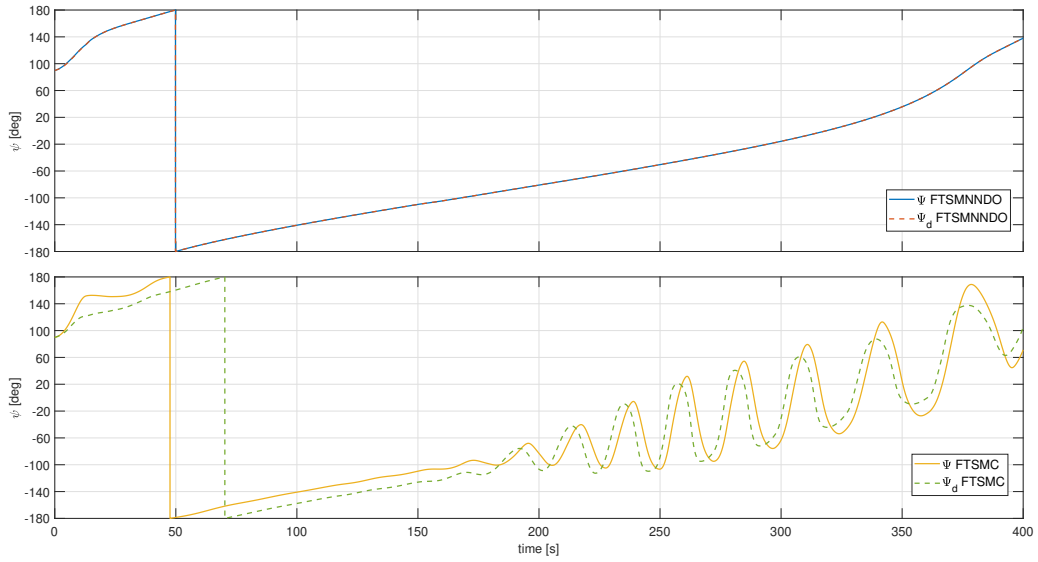

(b) Ψ for FTSMNNDO vs FTSMC

Figure 4.30: 6 DOF State Variables of FTSMNNDO and FTCSMC with $l_{M5} = 0.2$.

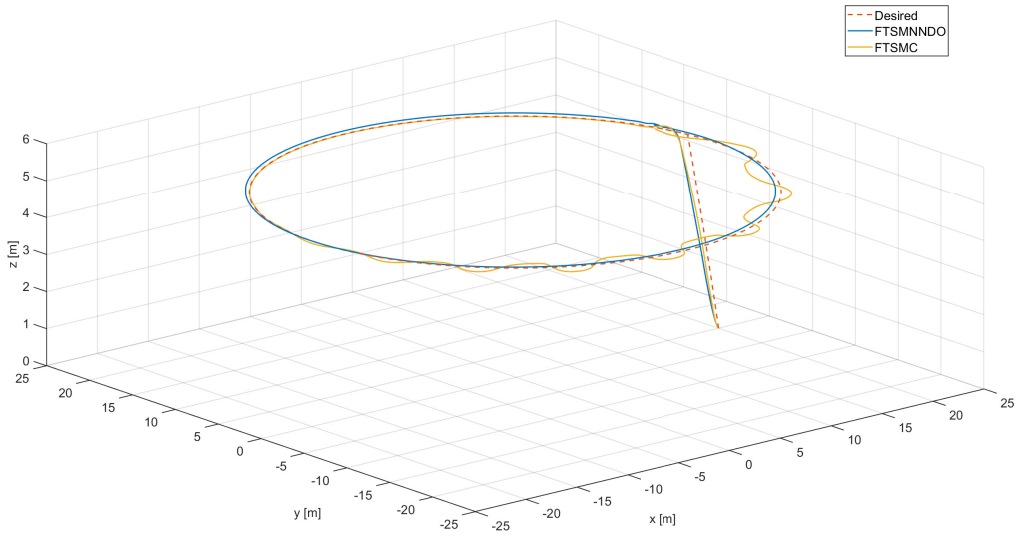

(a) 3D Trajectory

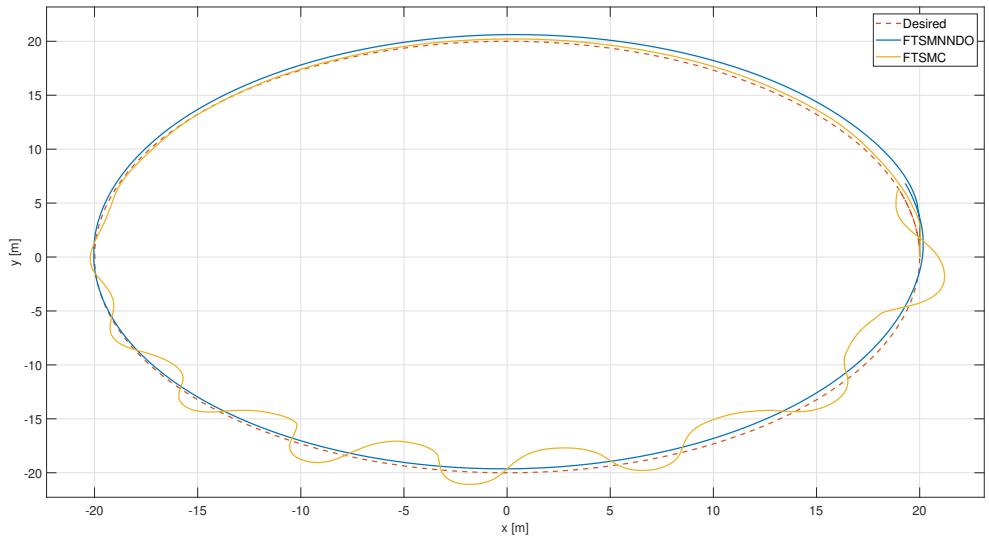

(b) 2D trajectory

Figure 4.31: 6 DOF Trajectories of FTSMNNDO and FTCSMC with $l_{M5} = 0.2$.

In contrast, FTSMNNDO remains unaffected by the fault, showing stable and bounded behavior across all state variables, particularly in ϕ where it closely resembles nominal performance. As shown in Figure 4.34, the estimation errors remain minimal, and the NN and DO estimates accurately track the disturbances and uncertainties introduced by the fault. Furthermore, FTSMNNDO maintains precise trajectory tracking, as seen in Figure 4.31, exhibiting smooth control inputs (Figure4.33) and minimal tracking errors. Overall, FTSMNNDO's performance highlights its passive fault-tolerant capability and robustness, as it achieves reliable trajectory tracking and stability throughout the simulation

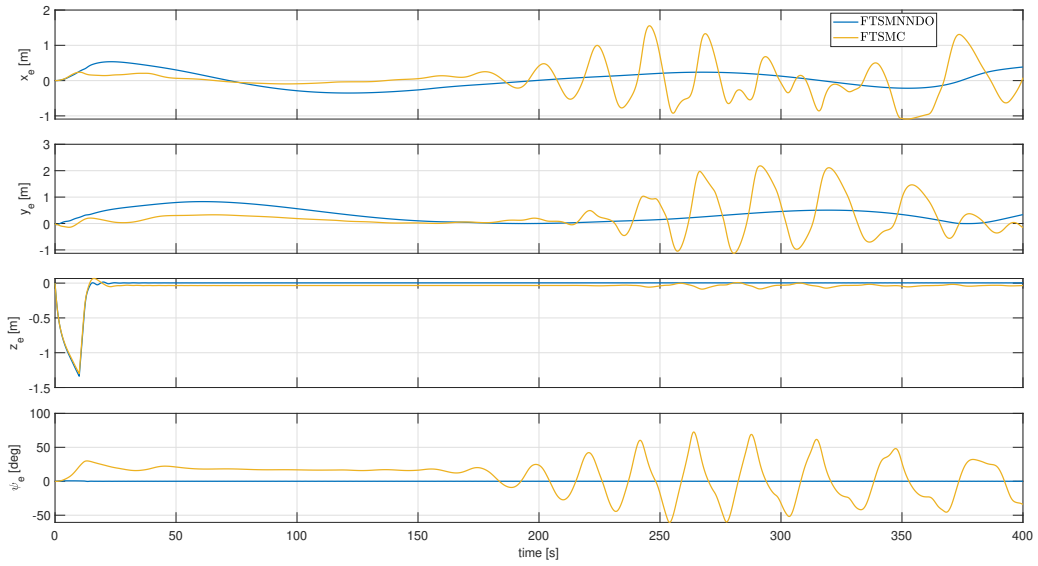

Figure 4.32: 6 DOF Position and Attitude Tracking Error of FTSMNNDO and FTSMC with $l_{M5} = 0.2$.

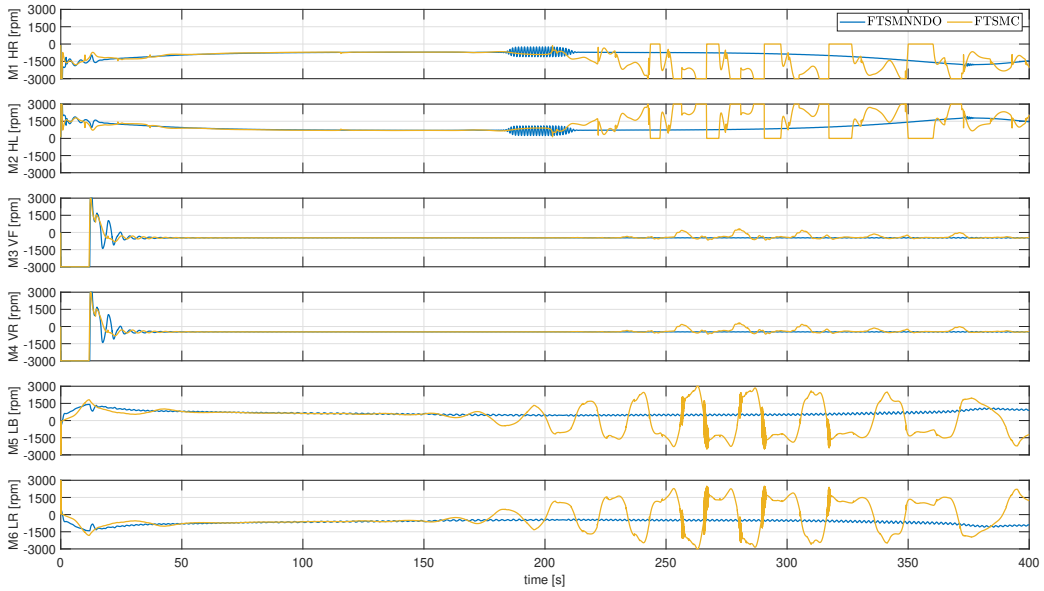

Figure 4.33: 6 DOF Thrusters inputs of FTSMNNDO and FTCSMC with $l_{M5} = 0.2$.

despite the occurrence of a fault.

The performance robustness of FTSMNNDO is further demonstrated by comparing the IAE, ISE, and ITAE across simulations with increasing fault magnitudes in the M5 thruster. Table 4.6 presents a comprehensive view of these indices across different fault levels, demonstrating that the FTSMNNDO succesfully maintains its trajecktory traking capability, even when $l_{M5} = 1$, corresponding to a complete failure of the M5 thruster.

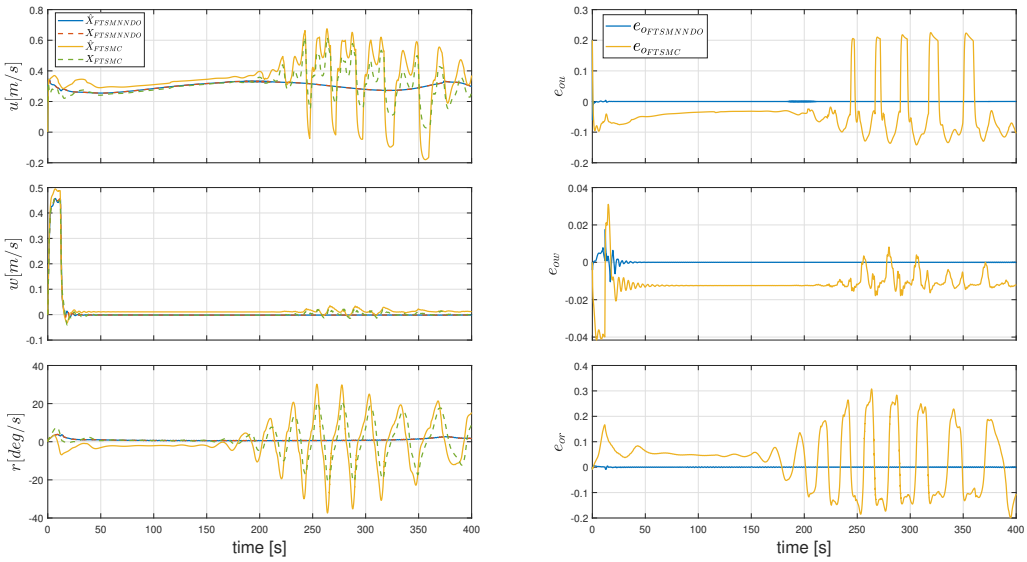

(a) 6 DOF State Observer Estimations and Estimation Errors of FTSMNNDO and FTSMC.

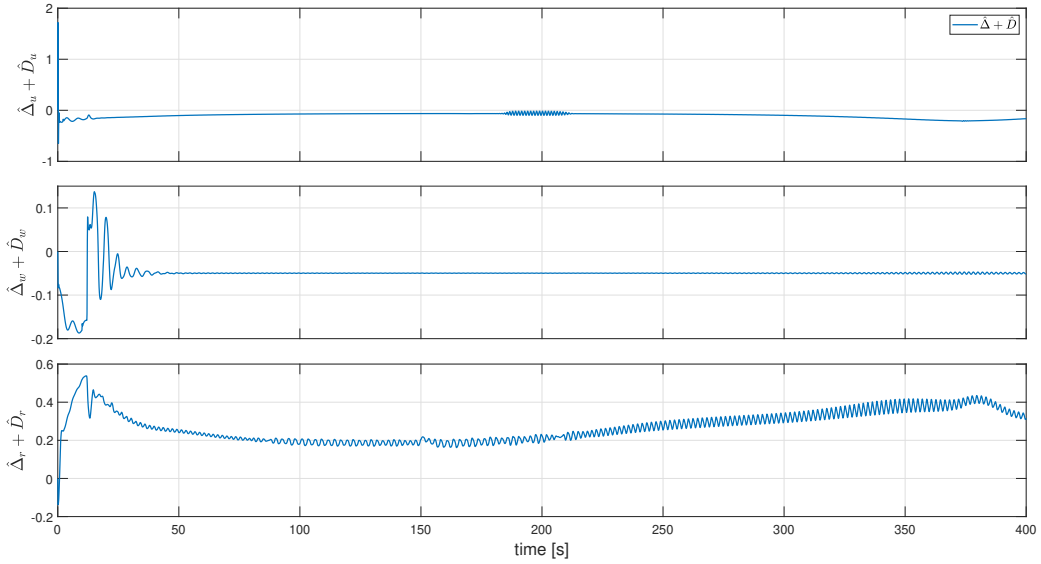

(b) $\hat{\Delta} + \hat{D}$ of FTSMNNDO.

Figure 4.34: 6 DOF State observer and $\hat{\Delta} + \hat{D}$ with $l_{M5} = 0.2$.

The results show that, under each fault condition, the FTSMNNDO controller's performance indices remain stable, underscoring its ability to adapt effectively to different fault magnitudes through NN and DO estimates. This adaptability is confirmed by the negligible changes observed in the IAE, ISE, and ITAE values, which highlight the FTSMNNDO's passive fault-tolerant functionality.Moreover, the results contrast with the performance of the FTSMC controller, which fails to track the trajectory when the fault magnitude reaches 0.39, illustrating the limitations of FTSMC in handling larger actuator

faults.

This table emphasizes that the FTSMNNDO controller not only compensates for actuator faults passively but also retains stability and accuracy in tracking, even under complex fault conditions and environmental disturbances, validating its effectiveness as a robust fault-tolerant control approach in 6-DOF underwater vehicle applications.

Fault l_{M5}	**FTSMC**				**FTSMNNDO**			
Magnitude	**IAE**	**ISE**	**ITAE**	**Failure**	**IAE**	**ISE**	**ITAE**	**Failure**
0.05	174	141	43071	No	169	100	27030	No
0.06	179	157	44801	No	169	100	27025	No
0.07	185	174	46890	No	169	100	27020	No
0.08	193	194	49282	No	169	100	27015	No
0.09	201	217	51979	No	169	100	27010	No
0.10	209	236	54262	No	169	100	27005	No
0.11	215	251	56063	No	169	100	27008	No
0.12	221	264	57687	No	169	100	27008	No
0.13	227	277	59328	No	169	100	27008	No
0.14	233	291	60959	No	169	100	27008	No
0.15	239	306	62649	No	169	100	27008	No
0.16	245	318	64168	No	169	100	26977	No
0.17	249	327	65399	No	169	100	26977	No
0.18	253	335	66508	No	169	100	26977	No
0.19	257	342	67511	No	169	100	26977	No
0.20	261	349	68497	No	169	100	26977	No
0.25	279	385	73625	No	169	100	26967	No
0.30	309	457	82162	No	169	100	26960	No
0.35	318	474	83865	No	169	100	26955	No
0.36	321	481	84846	No	169	100	26955	No
0.37	335	522	89112	No	169	100	26955	No
0.38	340	541	90570	No	169	100	26955	No
0.39	490	2174	148912	Yes	169	100	26955	No
0.40	549	3192	171281	Yes	169	100	26955	No
0.45	698	6314	227137	Yes	169	100	26963	No
0.50	409	803	108279	Yes	170	100	26980	No
0.60	623	1893	175817	Yes	170	100	27035	No
0.70	931	4227	271580	Yes	170	101	27093	No
0.80	1080	5788	319604	Yes	170	101	27149	No
0.90	1177	6902	351018	Yes	170	101	27233	No
1.00	1208	7287	361102	Yes	171	101	27337	No

Table 4.6: 6 DOF comparison of IAE, ISE, and ITAE for FTSMC and FTSMNNDO under different fault conditions on thruster M5

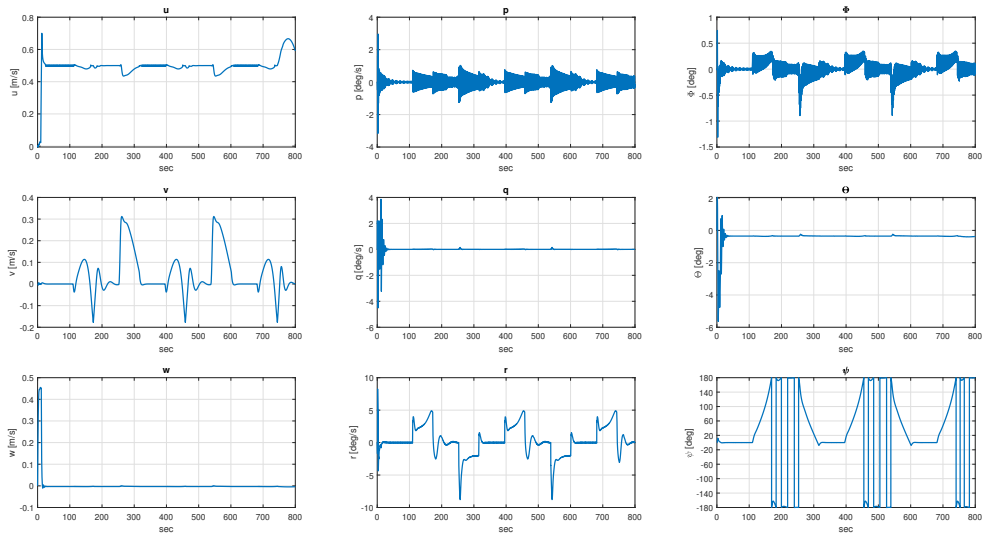

Figure 4.35: 6 DOF MBES Trajectory: State Variables

4.5.2.3 Test 3: MBES Survey

Test 3 is designed to evaluate the overall performance of the proposed FTSMNNDO control scheme under realistic operational conditions, including the presence of ocean currents and unmodeled dynamics, by simulating an MBES survey trajectory as depicted in Figure 4.24. The vehicle navigates a systematic pattern of parallel transects, each 50 meters long and separated by 20 meters, with smooth semicircular turns at each end to ensure continuous motion. By employing a trajectory that mimics actual MBES operations, Test 3 serves as a benchmark for demonstrating the control scheme's capabilities in handling the complexities of real-world missions.

The simulation results are presented in Figure 4.35-4.39. As can be seen in Figure 4.35, the pitch θ and roll ϕ angles remain close to zero, demonstrating the system's robustness in preventing oscillations that could compromise the multibeam's pointing accuracy. Furthermore, Figures 4.36 and 4.37 illustrate that the actual trajectory closely follows the desired one. It has to be noted that even if the semicircular turns are particularly challenging due to the lateral effect of the ocean current, the vehicle maintains smooth transitions and adheres to the desired trajectory showcasing the controller robustness. The contribution of the NN and DO estimations to achieving precise trajectory tracking is highlighted in Figure 4.39b. The NN and DO estimation is particularly significant in the r dynamics, where the combined effect of the ocean current and unmodeled vehicle dynamics during the semicircular turns are most pronounced. This coordinated estimation plays a crucial role in maintaining precise traking throughout the MBES survey.

The results of Test 3 highlight the effectiveness of the proposed FTSMNNDO control

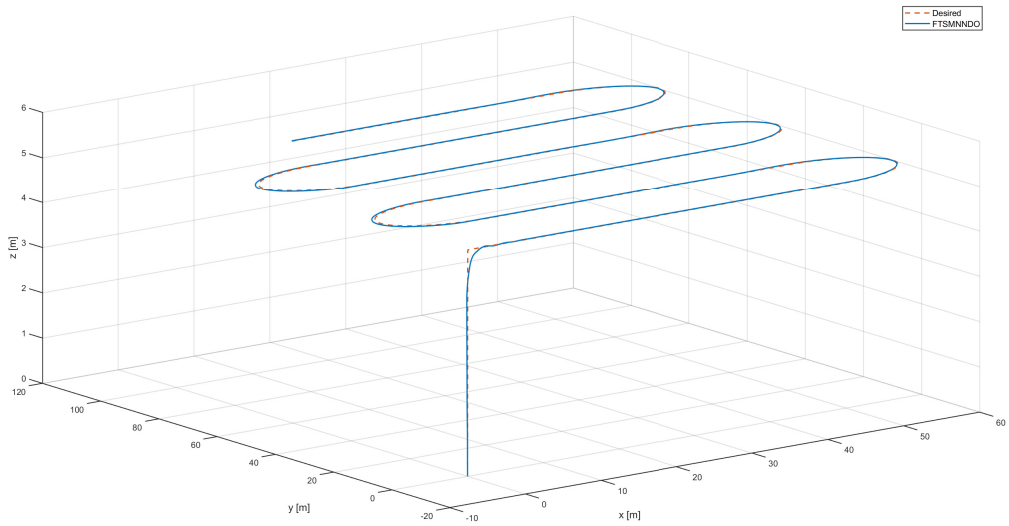

(a) 3D Trajectory

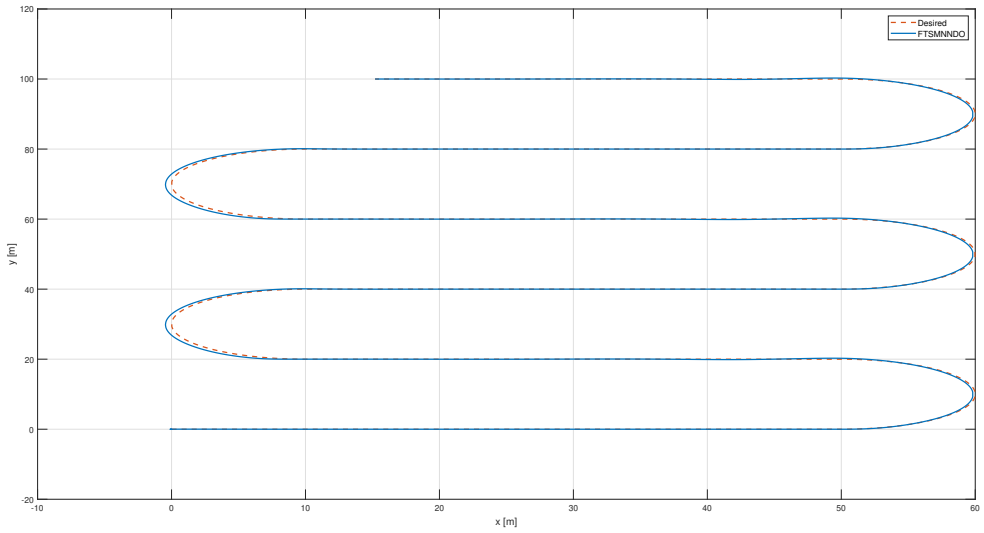

(b) 2D trajectory

Figure 4.36: 6 DOF MBES Trajectory with unmodeled dynamics and Ocean Current.

scheme in accurately tracking a realistic MBES survey trajectory, even under challenging conditions with ocean currents and unmodeled dynamics, demonstrating its robustness and applicability to real-world operational scenarios.

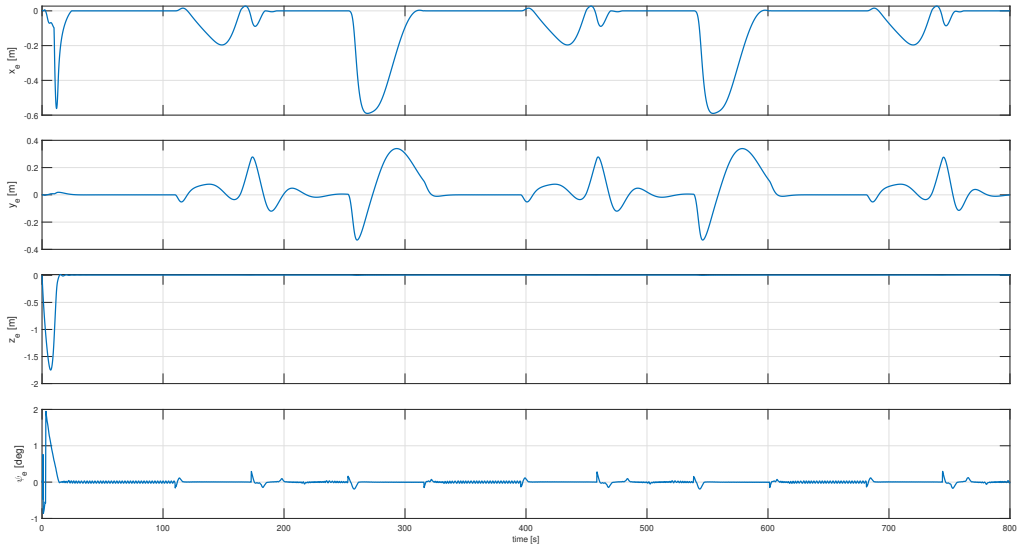

Figure 4.37: 6 DOF MBES Trajectory: Position and Attitude Tracking Error.

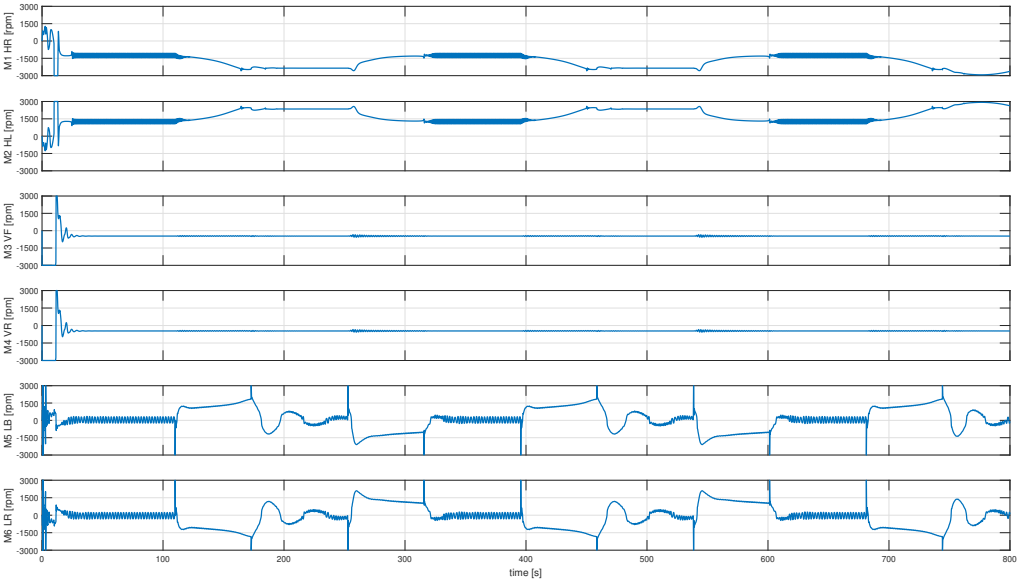

Figure 4.38: 6 DOF MBES Trajectory: Thrusters inputs.

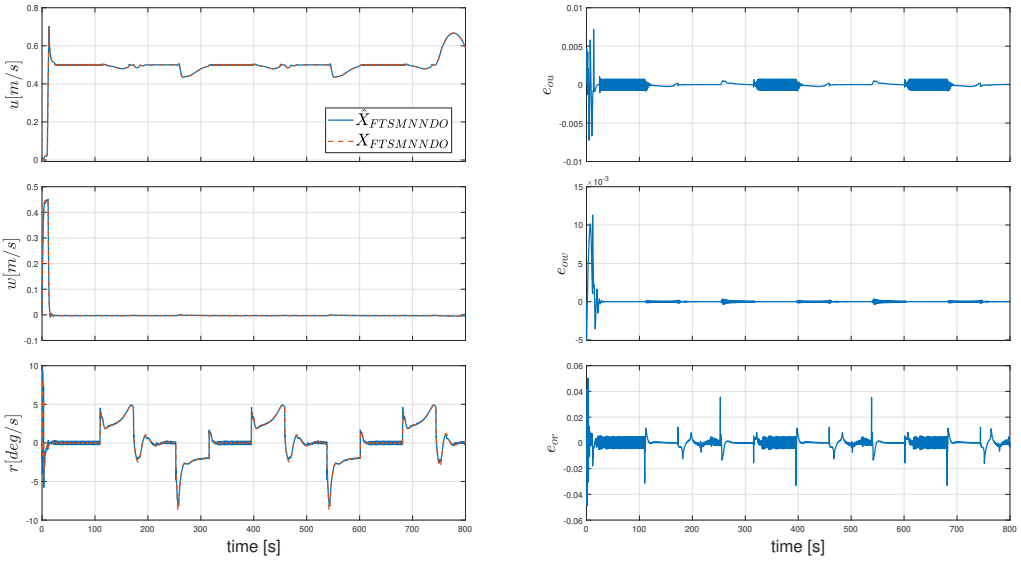

(a) State Observer Estimations and Estimation Errors.

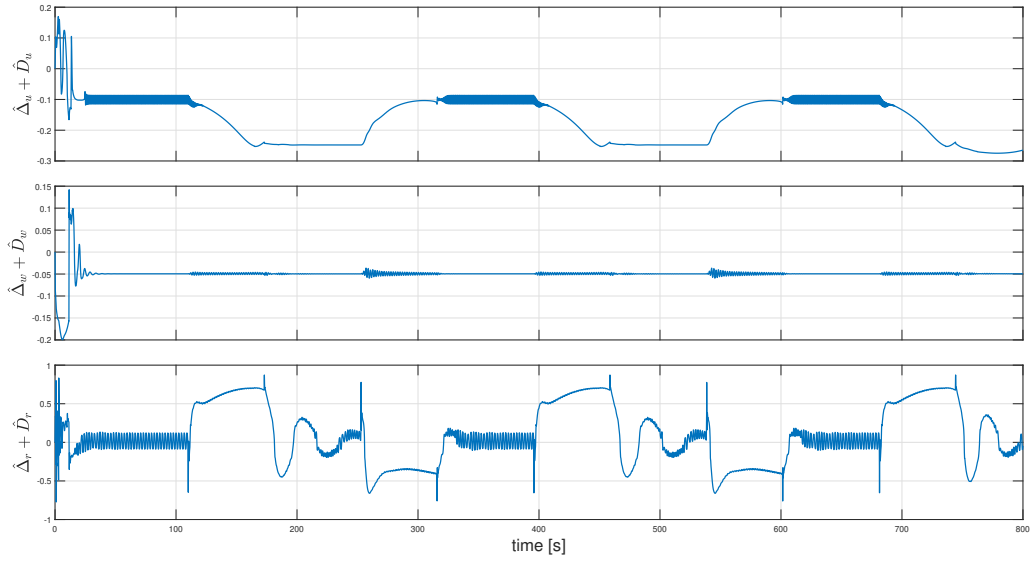

(b) $\hat{\Delta} + \hat{D}$

Figure 4.39: 6 DOF MBES Trajectory: State observer and $\hat{\Delta} + \hat{D}$

Chapter 5

Conclusions

This thesis presents, for the first time, an augmented fixed-time sliding mode controller for Blucy Unmanned Underwater Vehicle, integrating neural networks (NN) and a disturbance observer (DO) trained using composite error learning to estimate uncertainties and time-varying disturbances. The hybrid model-based approach is selected over an indirect data driven approach to avoid limitations due to data dependency. Data driven controls rely heavily on the data used for training; thus, if the vehicle is actually operating outside of known data, the results may be unreliable. To address this, a benchmark mathematical model, based on physical laws, for the underwater vehicle Blucy is developed. Model parameters are obtained by integrating high-fidelity CAD modeling, computational fluid dynamics (CFD) simulations, and specialized software such as AMCOMP. Physical parameters, including mass and inertial properties, are derived from the CAD model, while hydrodynamic and added mass coefficients are determined using CFD and AMCOMP, respectively. A four-quadrant thrust model is developed and refined using both experimental and simulation data. This comprehensive workflow can be generalized to other Blucy configurations and similar unmanned underwater vehicles (UUVs).

However, several limitations affect the accuracy of the parameter estimation. For instance, CFD simulations assumed stationary rotors, whereas in reality, they are moving, leading to potential discrepancies. Additionally, the CFD analysis simplified the vehicle model, potentially introducing further inaccuracies. Added mass parameters are estimated using AMCOMP, which relies on discretized STL files, making the accuracy of these estimates dependent on the quality of discretization and the balance between computational cost and model precision. Furthermore, cross-coupling terms for the added mass are neglected, reducing the overall accuracy of the model. The four-quadrant thrust model simplifies thruster nonlinearities and does not account for significant interactions between the hull and the thrusters, which can notably affect thrust generation.

Despite these limitations, the simulation results for the proposed benchmark model,

validated against real-world mission data, demonstrated its accuracy and reliability. The developed model is thus suitable for control prototyping across underactuated UUVs, enabling efficient testing and refinement of control strategies.

Building on a simplification of the benchmark model, i.e. synthesis model (4 DOF), a novel neuro-adaptive fixed-time sliding mode control strategy with composite learning is introduced to meet Blucy's control objectives. This control approach integrates a Neural Network (NN), Disturbance Observer (DO), and state estimator, working together to adapt to and compensate for model uncertainties and external disturbances. Composite learning enhances the feedback error learning adaptability by incorporating state estimation errors into the learning rule, reducing the need for high learning rates typically required in neuro-adaptive schemes. This adaptive control is further supported by a line-of-sight guidance law tailored to Blucy's underactuated dynamics, ensuring precise trajectory tracking. The stability of the developed control stystem is rigorously proven using the Lyapunov approach.

Simulations demonstrate that the Fixed-Time Sliding Mode Control with the neuro-adaptive NN and DO (FTSMNNDO) outperforms the standard Fixed Time Sliding Mode Controller (FTSMC) in both the 4-DOF and complete 6-DOF models, even in the presence of uncertainties, time-varying disturbances, and faults. This enhanced performance is attributed to the disturbance and uncertainty estimations provided by the NN and DO. Additionally, the thesis explores the accuracy of these estimations. However, producing an exact reference signal for evaluating the NN and DO estimations against true uncertainties and disturbances is challenging, particularly in the complete 6-DOF model. For the simplified 4-DOF model, controlled uncertainty and disturbance signals are generated to allow a more detailed assessment of estimation performance.

The NN and DO estimations are presented as combined outputs since these components are not structurally decoupled. This coupling of time-dependent disturbances with state-based uncertainties means that the NN and DO share information and jointly estimate disturbances and uncertainties, rather than isolating them individually. While the exact accuracy of these estimations remains unclear, simulation results indicate that they significantly enhance robustness against external disturbances and uncertainties.

The future works that can be derived from this thesis can be categorized into two main areas:

1. Enhancing the Mathematical Model: Future efforts will focus on addressing the identified limitations to improve model accuracy. This includes incorporating a tether model to study the interactions between the tether, body frame, and propellers, which will provide insights into how these dynamics affect the vehicle's maneuverability and stability during remote operations. Additionally, investigating

hull-propeller interactions will help identify and mitigate performance issues related to thruster dynamics, further enhancing the reliability and precision of the model.

2. Advancing the Control Framework: From a control perspective, future work will aim to investigate the possibility of structural decoupling of the NN and DO to better define their individual estimation roles. A promising approach is to apply differential geometry to create a subspace where uncertainties can be separated from disturbances, allowing the NN and DO to estimate each element independently. This separation would clarify the NN and DO's specific roles in estimation, reducing ambiguity in the control framework and enabling more targeted parameter tuning. Additionally, another valuable direction is to generalize the NN's capabilities to estimate uncertainties that are functions of both system states and time-varying disturbances, thereby broadening its adaptability and robustness.

Bibliography

[1] Yongpeng Weng, Ning Wang, Hongde Qin, Hamid Reza Karimi, and Wenhai Qi. "Data-driven adaptive tracking control of unknown autonomous marine vehicles". In: *IEEE Access* 6 (2018), pp. 55723–55730.

[2] Vishaal Krishnan and Fabio Pasqualetti. "On Direct vs Indirect Data-Driven Predictive Control". In: *2021 60th IEEE Conference on Decision and Control (CDC)*. 2021, pp. 736–741. DOI: 10.1109/CDC45484.2021.9683187.

[3] Bilal Wehbe, Alexander Fabisch, and Mario Michael Krell. "Online model identification for underwater vehicles through incremental support vector regression". In: *2017 IEEE/RSJ International Conference on Intelligent Robots and Systems (IROS)*. 2017, pp. 4173–4180. DOI: 10.1109/IROS.2017.8206278.

[4] Lei Lei, Yang Gang, Guo Jing, and Liqun Chen. "Gliding hydrodynamic modeling and identification of underwater glider based on differential evolution algorithm". In: *Ocean Engineering* 244 (2022), p. 110250.

[5] Seyyed Ali Emami, Paolo Castaldi, and Afshin Banazadeh. "Neural network-based flight control systems: Present and future". In: *Annual Reviews in Control* 53 (2022), pp. 97–137. ISSN: 1367-5788. DOI: https://doi.org/10.1016/j.arcontrol.2022.04.006. URL: https://www.sciencedirect.com/science/article/pii/S1367578822000219.

[6] Italy-Croatia Interreg. *SUSHI DROP SUstainable fiSHeries wIth DROnes data Processing*. https://www.italy-croatia.eu/web/sushidrop. 2019.

[7] You Hong Eng, Kwong Meng Teo, Mandar Chitre, and Kien Ming Ng. "Online system identification of an autonomous underwater vehicle via in-field experiments". In: *IEEE Journal of Oceanic Engineering* 41.1 (2015), pp. 5–17.

[8] Bilal Wehbe, Alexander Fabisch, and Mario Michael Krell. "Online model identification for underwater vehicles through incremental support vector regression". In: *2017 IEEE/RSJ International Conference on Intelligent Robots and Systems (IROS)*. IEEE. 2017, pp. 4173–4180.

[9] George C Karras, Panos Marantos, Charalampos P Bechlioulis, and Kostas J Kyriakopoulos. "Unsupervised online system identification for underwater robotic vehicles". In: *IEEE Journal of Oceanic Engineering* 44.3 (2018), pp. 642–663.

[10] Thor I Fossen. *Handbook of marine craft hydrodynamics and motion control*. John Wiley & Sons, 2011.

[11] Gianluca Antonelli, Thor I Fossen, and Dana R Yoerger. "Modeling and control of underwater robots". In: *Springer Handbook of Robotics* (2016), pp. 1285–1306.

[12] Bruno Ferreira, Anibal Matos, Nuno Cruz, and Miguel Pinto. "Modeling and control of the MARES autonomous underwater vehicle". In: *Marine Technology Society Journal* 44.2 (2010), pp. 19–36.

[13] Masao Nomoto and Mutsuo Hattori. "A deep ROV" DOLPHIN 3K": design and performance analysis". In: *IEEE Journal of Oceanic Engineering* 11.3 (1986), pp. 373–391.

[14] Sven Lack, Erik Rentzow, and Torsten Jeinsch. "Experimental Parameter Identification for an open-frame ROV: Comparison of towing tank tests and open water self-propelled tests". In: *IFAC-PapersOnLine* 52.21 (2019), pp. 271–276.

[15] Alex Goodman. "Description and operation of sub planar motion mechanism system". In: *Hydronautics Technical Manual, Hydronautics* (1979).

[16] Massimo Caccia, Giovanni Indiveri, and Gianmarco Veruggio. "Modeling and identification of open-frame variable configuration unmanned underwater vehicles". In: *IEEE journal of Oceanic Engineering* 25.2 (2000), pp. 227–240.

[17] P Ridao, A Tiano, A El-Fakdi, M Carreras, and A Zirilli. "On the identification of non-linear models of unmanned underwater vehicles". In: *Control engineering practice* 12.12 (2004), pp. 1483–1499.

[18] David A Smallwood and Louis L Whitcomb. "Adaptive identification of dynamically positioned underwater robotic vehicles". In: *IEEE Transactions on Control Systems Technology* 11.4 (2003), pp. 505–515.

[19] Saeed Ebrahimi, Mohammad Bozorg, and Mehdi Zare Ernani. "Identification of an autonomous underwater vehicle dynamic using extended Kalman filter with ARMA noise model". In: *International Journal of Robotics, Theory and Applications* 4.1 (2015), pp. 22–28.

[20] Yadollah Sajedi and Mohammad Bozorg. "Robust estimation of hydrodynamic coefficients of an AUV using Kalman and Hinf filters". In: *Ocean Engineering* 182 (2019), pp. 386–394.

[21] Pepijn WJ Van De Ven, Tor A Johansen, Asgeir J Sørensen, Colin Flanagan, and Daniel Toal. "Neural network augmented identification of underwater vehicle models". In: *Control Engineering Practice* 15.6 (2007), pp. 715–725.

[22] Nikola Miskovic, Zoran Vukic, Matko Barisic, and Philip P Soucacos. "AUV identification by use of self-oscillations". In: *IFAC Proceedings Volumes* 40.17 (2007), pp. 181–186.

[23] Juan PJ Avila, Décio C Donha, and Julio C Adamowski. "Experimental model identification of open-frame underwater vehicles". In: *Ocean Engineering* 60 (2013), pp. 81–94.

[24] Benedetto Allotta, Riccardo Costanzi, Luca Pugi, and Alessandro Ridolfi. "Identification of the main hydrodynamic parameters of Typhoon AUV from a reduced experimental dataset". In: *Ocean Engineering* 147 (2018), pp. 77–88.

[25] Farhad Ghanipoor, Aria Alasty, Hassan Salarieh, Mojtaba Hashemi, and Mohammad Shahbazi. "Model identification of a Marine robot in presence of IMU-DVL misalignment using TUKF". In: *Ocean Engineering* 206 (2020), p. 107344.

[26] Mustafa Dinç and Chingiz Hajiyev. "Identification of hydrodynamic coefficients of AUV in the presence of measurement biases". In: *Proceedings of the Institution of Mechanical Engineers, Part M: Journal of Engineering for the Maritime Environment* 236.3 (2022), pp. 756–763.

[27] Amit Tyagi and Debabrata Sen. "Calculation of transverse hydrodynamic coefficients using computational fluid dynamic approach". In: *Ocean Engineering* 33.5-6 (2006), pp. 798–809.

[28] He Zhang, Yu-ru Xu, and Hao-peng Cai. "Using CFD software to calculate hydrodynamic coefficients". In: *Journal of Marine Science and Application* 9 (2010), pp. 149–155.

[29] Gwangsoo Go and Hyung Taek Ahn. "Hydrodynamic derivative determination based on CFD and motion simulation for a tow-fish". In: *Applied Ocean Research* 82 (2019), pp. 191–209.

[30] Feiyan Min, Guoliang Pan, and Xuefeng Xu. "Modeling of autonomous underwater vehicles with multi-propellers based on maximum likelihood method". In: *Journal of Marine Science and Engineering* 8.6 (2020), p. 407.

[31] Faheem Ahmed, Xianbo Xiang, Chaicheng Jiang, Gong Xiang, and Shaolong Yang. "Survey on traditional and AI based estimation techniques for hydrodynamic coefficients of autonomous underwater vehicle". In: *Ocean Engineering* 268 (2023), p. 113300.

[32] Ehsan Javanmard, Shahriar Mansoorzadeh, and Javad A Mehr. "A new CFD method for determination of translational added mass coefficients of an underwater vehicle". In: *Ocean Engineering* 215 (2020), p. 107857.

[33] Frederick Jaouen, Arjen Koop, and Guilherme Vaz. "Predicting roll added mass and damping of a ship hull section using CFD". In: *International Conference on Offshore Mechanics and Arctic Engineering*. Vol. 44397. 2011, pp. 105–115.

[34] Boris V Korvin-Kroukovsky and Winnifred R Jacobs. "Pitching and heaving motions of a ship in regular waves". In: *Trans. Sname* 65 (1957), pp. 590–632.

[35] Horace Lamb. *Hydrodynamics*. University Press, 1924.

[36] Alessandro Ceruti, T Bombardi, and Piergiovanni Marzocca. "A CAD environment for the fast computation of Added Masses". In: *Ocean Engineering* 142 (2017), pp. 329–337.

[37] Andreas J Häusler, Alessandro Saccon, John Hauser, António M Pascoal, and A Pedro Aguiar. "Four-Quadrant Propeller Modeling: a low-order harmonic approximation". In: *IFAC Proceedings Volumes* 46.33 (2013), pp. 161–166.

[38] Gert Kuiper. "The Wageningen propeller series". In: *MARIN Publication 91-001'Published on the occasion of its 60th anniversary, MARIN Wageningen, The Netherlands* (1992).

[39] John Carlton. *Marine propellers and propulsion*. Butterworth-Heinemann, 2018.

[40] MWC Oosterveld. "Ducted propeller characteristics". In: *RINA symposium on ducted propellers*. 1973.

[41] Ralph Bachmayer, Louis L Whitcomb, and Mark A Grosenbaugh. "An accurate four-quadrant nonlinear dynamical model for marine thrusters: Theory and experimental validation". In: *IEEE Journal of Oceanic Engineering* 25.1 (2000), pp. 146–159.

[42] Jinhyun Kim and Wan Kyun Chung. "Accurate and practical thruster modeling for underwater vehicles". In: *Ocean Engineering* 33.5-6 (2006), pp. 566–586.

[43] Gianluca Antonelli, Fabrizio Caccavale, Stefano Chiaverini, and Giuseppe Fusco. "A novel adaptive control law for underwater vehicles". In: *IEEE Transactions on control systems technology* 11.2 (2003), pp. 221–232.

[44] Hangil Joe, Minsung Kim, and Son-cheol Yu. "Second-order sliding-mode controller for autonomous underwater vehicle in the presence of unknown disturbances". In: *Nonlinear Dynamics* 78 (2014), pp. 183–196.

[45] Kairong Duan, Simon Fong, and CL Philip Chen. "Fuzzy observer-based tracking control of an underactuated underwater vehicle with linear velocity estimation". In: *IET Control Theory & Applications* 14.4 (2020), pp. 584–593.

[46] Yintao Wang, Weisheng Yan, Bo Gao, and Rongxin Cui. "Backstepping-based path following control of an underactuated autonomous underwater vehicle". In: *2009 International conference on information and automation*. IEEE. 2009, pp. 466–471.

[47] Shahab Heshmati-Alamdari, Alina Eqtami, George C Karras, Dimos V Dimarogonas, and Kostas J Kyriakopoulos. "A self-triggered visual servoing model predictive control scheme for under-actuated underwater robotic vehicles". In: *2014 IEEE International Conference on Robotics and Automation (ICRA)*. IEEE. 2014, pp. 3826–3831.

[48] Jesus Guerrero, Jorge Torres, Vincent Creuze, and Ahmed Chemori. "Observation-based nonlinear proportional–derivative control for robust trajectory tracking for autonomous underwater vehicles". In: *IEEE journal of oceanic engineering* 45.4 (2019), pp. 1190–1202.

[49] Shahab Heshmati-Alamdari, Alexandros Nikou, and Dimos V Dimarogonas. "Robust trajectory tracking control for underactuated autonomous underwater vehicles in uncertain environments". In: *IEEE Transactions on Automation Science and Engineering* 18.3 (2020), pp. 1288–1301.

[50] Hashem Ashrafiuon, Kenneth R Muske, and Lucas C McNinch. "Review of nonlinear tracking and setpoint control approaches for autonomous underactuated marine vehicles". In: *Proceedings of the 2010 American control conference*. IEEE. 2010, pp. 5203–5211.

[51] Jian Xu, Man Wang, and Lei Qiao. "Dynamical sliding mode control for the trajectory tracking of underactuated unmanned underwater vehicles". In: *Ocean engineering* 105 (2015), pp. 54–63.

[52] Taha Elmokadem, Mohamed Zribi, and Kamal Youcef-Toumi. "Trajectory tracking sliding mode control of underactuated AUVs". In: *Nonlinear Dynamics* 84 (2016), pp. 1079–1091.

[53] Taha Elmokadem, Mohamed Zribi, and Kamal Youcef-Toumi. "Terminal sliding mode control for the trajectory tracking of underactuated Autonomous Underwater Vehicles". In: *Ocean Engineering* 129 (2017), pp. 613–625.

[54] Adrian Manzanilla, Efraín Ibarra, Sergio Salazar, Ángel E Zamora, Rogelio Lozano, and Filiberto Munoz. "Super-twisting integral sliding mode control for trajectory tracking of an Unmanned Underwater Vehicle". In: *Ocean Engineering* 234 (2021), p. 109164.

[55] Haomiao Yu, Chen Guo, and Zheping Yan. "Globally finite-time stable three-dimensional trajectory-tracking control of underactuated UUVs". In: *Ocean Engineering* 189 (2019), p. 106329.

[56] Wei Liu, Hui Ye, and Xiaofei Yang. "Super-twisting sliding mode control for the trajectory tracking of underactuated USVs with disturbances". In: *Journal of Marine Science and Engineering* 11.3 (2023), p. 636.

[57] Andrey Polyakov. "Nonlinear feedback design for fixed-time stabilization of linear control systems". In: *IEEE transactions on Automatic Control* 57.8 (2011), pp. 2106–2110.

[58] Hongde Qin, Jinshuai Si, Ning Wang, and Liyang Gao. "Fast fixed-time nonsingular terminal sliding-mode formation control for autonomous underwater vehicles based on a disturbance observer". In: *Ocean Engineering* 270 (2023), p. 113423.

[59] Bo Su, Hongbin Wang, and Ning Li. "Event-triggered integral sliding mode fixed time control for trajectory tracking of autonomous underwater vehicle". In: *Transactions of the Institute of Measurement and Control* 43.15 (2021), pp. 3483–3496.

[60] Jiaqi Zheng, Lei Song, Lingya Liu, Wenbin Yu, Yiyin Wang, and Cailian Chen. "Fixed-time sliding mode tracking control for autonomous underwater vehicles". In: *Applied Ocean Research* 117 (2021), p. 102928.

[61] Zhongben Zhu, Zhengqi Duan, Hongde Qin, and Yifan Xue. "Adaptive neural network fixed-time sliding mode control for trajectory tracking of underwater vehicle". In: *Ocean Engineering* 287 (2023), p. 115864.

[62] Meng Joo Er, Huibin Gong, Yi Liu, and Tianhe Liu. "Intelligent trajectory tracking and formation control of underactuated autonomous underwater vehicles: A critical review". In: *IEEE Transactions on Systems, Man, and Cybernetics: Systems* (2023).

[63] Junnan Liu and Jialu Du. "Composite learning tracking control for underactuated autonomous underwater vehicle with unknown dynamics and disturbances in three-dimension space". In: *Applied Ocean Research* 112 (2021), p. 102686.

[64] Jiajia Zhou, Xinyi Zhao, Tao Chen, Zheping Yan, and Zewen Yang. "Trajectory tracking control of an underactuated AUV based on backstepping sliding mode with state prediction". In: *IEEE Access* 7 (2019), pp. 181983–181993.

[65] Charita D Makavita, Hung D Nguyen, Dev Ranmuthugala, and Shantha G Jayasinghe. "Composite model reference adaptive control for an unmanned underwater vehicle". In: *Underwater Technology* 33.2 (2015), pp. 81–93.

[66] M. A. Abkowitz. *Lectures on Ship Hydrodynamics – Steering and Maneuverability.* Tech. rep. Report No. Hy-5. Hydro- and Aerodynamics Laboratory, Hydrodynamics Section, Lyngby, Denmark, 1964.

[67] K. K. Fedyaevsky and G. V. Sobolev. *Control and Stability in Ship Design.* Leningrad: State Union Shipbuilding Industry Publishing House, 1963.

[68] Frederick H. Imlay. *The complete expressions for added mass of a rigid body moving in an ideal fluid.* Tech. rep. David Taylor Model Basin Washington DC, 1961.

[69] Julián González Agudelo. "Contribution to the model and navigation control of an autonomous underwater vehicle". PhD thesis. Universitat Politécnica de Catalunya, July 2015.

[70] Consiglio Nazionale delle Ricerche. *Sushi Drop AUV/ROV, Manuale di uso e manutenzione.* Restricted, Interreg IT-HR SUSHI DROP Project, Oct. 2018.

[71] MWC Oosterveld. "Wake adapted ducted propellers". PhD thesis. Delft University of Technology, Doctors Thesis, Publication 345 of The Netherlands Ship Model Basin, 1970.

[72] Italy-Croatia Interreg. *TECHERA: A new technology era in the Adriatic Sea – Big data sharing and analytics for a circular sea economy.* `https://programming14-20.italy-croatia.eu/web/techera`. 2022.

[73] Wei Sun, Shuzhen Diao, Shun-Feng Su, and Zong-Yao Sun. "Fixed-time adaptive neural network control for nonlinear systems with input saturation". In: *IEEE Transactions on Neural Networks and Learning Systems* 34.4 (2021), pp. 1911–1920.

[74] Desheng Ba, Yuan-Xin Li, and Shaocheng Tong. "Fixed-time adaptive neural tracking control for a class of uncertain nonstrict nonlinear systems". In: *Neurocomputing* 363 (2019), pp. 273–280.

[75] Huijie Li and Yuanli Cai. "On SFTSM control with fixed-time convergence". In: *IET Control Theory & Applications* 11.6 (2017), pp. 766–773.

[76] Özhan Bingöl and Hacı Mehmet Güzey. "Fixed-time neuro-sliding mode controller design for quadrotor UAV transporting a suspended payload". In: *European Journal of Control* 73 (2023), p. 100879.

[77] Qiang Chen, Shuzong Xie, and Xiongxiong He. "Neural-network-based adaptive singularity-free fixed-time attitude tracking control for spacecrafts". In: *IEEE Transactions on Cybernetics* 51.10 (2020), pp. 5032–5045.

[78] Haijiao Yang and Dan Ye. "Adaptive fixed-time bipartite tracking consensus control for unknown nonlinear multi-agent systems: An information classification mechanism". In: *Information Sciences* 459 (2018), pp. 238–254.

[79] Tomaso Poggio and Federico Girosi. "Regularization algorithms for learning that are equivalent to multilayer networks". In: *Science* 247.4945 (1990), pp. 978–982.

[80] Morten Breivik and Thor I Fossen. "Principles of guidance-based path following in 2D and 3D". In: *Proceedings of the 44th IEEE Conference on Decision and Control*. IEEE. 2005, pp. 627–634.

[81] Anastasios M Lekkas and Thor I Fossen. "Integral LOS path following for curved paths based on a monotone cubic Hermite spline parametrization". In: *IEEE Transactions on Control Systems Technology* 22.6 (2014), pp. 2287–2301.

[82] V. Utkin and Hoon Lee. "Chattering Problem in Sliding Mode Control Systems". In: *International Workshop on Variable Structure Systems, 2006. VSS'06.* 2006, pp. 346–350. DOI: 10.1109/VSS.2006.1644542.

[83] Yuri Shtessel, Christopher Edwards, Leonid Fridman, Arie Levant, et al. *Sliding mode control and observation*. Vol. 10. Springer, 2014.

[84] G. Bartolini, A. Ferrara, and E. Usai. "Chattering avoidance by second-order sliding mode control". In: *IEEE Transactions on Automatic Control* 43.2 (1998), pp. 241–246. DOI: 10.1109/9.661074.

[85] Leonid Fridman Yuri Shtessel and Franck Plestan. "Adaptive sliding mode control and observation". In: *International Journal of Control* 89.9 (2016), pp. 1743–1746. DOI: 10.1080/00207179.2016.1194531. eprint: https://doi.org/10.1080/00207179.2016.1194531. URL: https://doi.org/10.1080/00207179.2016.1194531.

[86] Jie Chen and Ron J Patton. *Robust model-based fault diagnosis for dynamic systems*. Vol. 3. Springer Science & Business Media, 2012.

[87] Giulio Notarstefano, Pierre-Marie Poulain, and Elena Mauri. "Estimation of surface currents in the Adriatic Sea from sequential infrared satellite images". In: *Journal of Atmospheric and Oceanic Technology* 25.2 (2008), pp. 271–285.

[88] Simone Cosoli, Andrea Mazzoldi, and Miroslav Gačić. "Validation of surface current measurements in the northern Adriatic Sea from high-frequency radars". In: *Journal of Atmospheric and Oceanic Technology* 27.5 (2010), pp. 908–919.

[89] P-M Poulain and S Hariri. “Transit and residence times in the Adriatic Sea surface as derived from drifter data and Lagrangian numerical simulations”. In: *Ocean Science* 9.4 (2013), pp. 713–720.

Author's Publications

[P1] Paolo Castaldi, Saverio Farsoni, Massimiliano Menghini, and Silvio Simani. "Data–Driven Fault Detection and Isolation of the Actuators of an Autonomous Underwater Vehicle". In: *2021 5th International Conference on Control and Fault-Tolerant Systems (SysTol)*. 2021, pp. 139–144. DOI: 10.1109/SysTol52990.2021.9595605.

[P2] Alessandro Lambertini, Massimiliano Menghini, Jacopo Cimini, Angelo Odetti, Gabriele Bruzzone, Marco Bibuli, Emanuele Mandanici, Luca Vittuari, Paolo Castaldi, Massimo Caccia, et al. "Underwater drone architecture for marine digital twin: Lessons learned from sushi drop project". In: *Sensors* 22.3 (2022), p. 744.

[P3] M. Menghini, S.K. Mallipeddi, L. De Marchi, and P. Castaldi. "Modelling and parameter identification of UUV Blucy for control design: A benchmark model". In: *Ocean Engineering* 313 (2024), p. 119617. ISSN: 0029-8018. DOI: https://doi.org/10.1016/j.oceaneng.2024.119617. URL: https://www.sciencedirect.com/science/article/pii/S002980182402955X.

[P4] M. Menghini, S.K. Mallipeddi, Luca De Marchi, and Paolo Castaldi. "Adaptive Fixed Time Sliding Mode Control of Underactuated Underwater Vehicle Using Composite Error Learning". In: (Dec. 2024). DOI: 10.22541/au.173407357.78233025/v1. URL: http://dx.doi.org/10.22541/au.173407357.78233025/v1.

[P5] M Menghini, SK Mallipeddi, P Castaldi, and L De Marchi. "Neuro Adaptive Integral Sliding mode Control based on Composite Learning for Path Following of Underactuated Underwater Vehicle : Blucy". In: *Conference Proceedings of iSCSS* (2024). DOI: https://doi.org/10.24868/11138. URL: http://library.imarest.org/record/11138.

[P6] Silvio Simani, Saverio Farsoni, Paolo Castaldi, and Massimiliano Menghini. "Actuator Fault Reconstruction via Dynamic Neural Networks for an Autonomous Underwater Vehicle Model". In: *IFAC-PapersOnLine* 55.6 (2022), pp. 755–759.

[P7] Paolo Castaldi, Saverio Farsoni, Massimiliano Menghini, and Silvio Simani. "Artificial Intelligence Tools for Actuator Fault Diagnosis of an Unmanned Underwater Vehicle". In: *Science and Information Conference*. Springer. 2022, pp. 392–403.